THESIS FOR THE DEGREE OF DOCTOR OF PHILOSOPHY

Spin transport and dynamics in van der Waals magnets and graphene devices

ROSELLE TORIO NGALOY

Department of Microtechnology and Nanoscience (MC2)
Quantum Device Physics Laboratory
CHALMERS UNIVERSITY OF TECHNOLOGY

Göteborg, Sweden 2025

Spin transport and dynamics in van der Waals magnets and graphene devices

ROSELLE TORIO NGALOY
Göteborg, Sweden 2025
ISBN 978-91-8103-271-0

Doktorsavhandlingar vid Chalmers tekniska högskola
Ny serie Nr 5729
ISSN 0346-718X

Quantum Device Physics Laboratory
Department of Microtechnology and Nanoscience (MC2)
Chalmers University of Technology
SE-412 96 Göteborg, Sweden
Telephone: +46 (0)31-772 1000

Cover
Schematic illustration of spin injection in graphene spin valves, magnetization dynamics, and spin textures

Printed by Chalmers Reproservice
Göteborg, Sweden 2025

Spin transport and dynamics in van der Waals magnets and graphene devices
ROSELLE TORIO NGALOY
Quantum Device Physics Laboratory
Department of Microtechnology and Nanoscience (MC2)
Chalmers University of Technology

ABSTRACT

Two dimensional (2D) magnetic materials have emerged as promising platforms for next-generation 2D spintronic devices due to their intrinsic two-dimensionality, tunable magnetism, rich band structures, and ease of integration with other layered materials while maintaining atomically sharp interfaces. A key advancement in the field has been the demonstration of room temperature ferromagnetism in itinerant ferromagnetic materials such as Fe_5GeTe_2 and its doped species with tunable magnetic anisotropy and ground state, as well as in Fe_3GaTe_2 with perpendicular magnetic anisotropy, overcoming previous temperature limitations. In this work, it is shown that these van der Waals (vdW) magnets exhibit low magnetic damping, anisotropic spin dynamics, and efficient spin injection and detection when combined with graphene. Integrated into lateral spin valve devices, these materials reveal robust spin signals, negative spin polarization, and complex spin orientations at the interfaces. Additionally, engineered heterostructures allow for all-electrical detection of spin textures, enabling multi-level switching behavior and expanding device functionality. New vdW ferromagnet, Fe_3GaTe_2, also display strong nonlinear Hall responses and self-induced spin-orbit torques, opening avenues for electrically driven magnetization control. Together, these developments position 2D magnets as a versatile foundation for spintronic and quantum devices operating at ambient conditions.

Keywords: spintronics, 2D magnets, graphene spin valves, spin orbit torque, van der Waals heterostructures, graphene, magnetization dynamics

ACKNOWLEDGEMENTS

First and foremost, I extend my sincere gratitude to my supervisor, Professor Saroj Dash, for his patience, guidance, and endless innovative ideas. His consistent support and insightful feedback have been crucial in shaping the direction and quality of this work. I also want to express my appreciation to my examiner, Professor Janine Splettstoesser, for her invaluable support and guidance, in making sure that my doctoral studies progress smoothly. I thank my co-supervisor, Assistant Professor Alexei Kalaboukhov, for his continuous help and assistance.

I am deeply grateful to the Area of Advance (AoA) Nano Chalmers for funding my PhD studies. Without their generous support, this academic journey would not have been possible. I would also like to acknowledge funding from EU Graphene Flaghsip project 2DSPIN-TECH (No. 101135853), 2D TECH VINNOVA (No. 2019-00068), FLAG-ERA project 2DSOTECH (VR No. 2021-05925), and Swedish Research Council (VR) grant (No. 2021–04821).

I would like to extend my heartfelt gratitude to Dr. Bing Zhao for his invaluable mentorship and patient guidance through my early years. I deeply appreciate the time and effort he invested in explaining concepts, providing thoughtful advice, and constructively engaging with my ideas, even when they were preliminary or undeveloped. Special thanks go to Dr. Prasanna Rout, Dr. Lalit Pandey, and Dr. Himanshu Bangar for the fruitful discussions, advices, mentorship, and assistance, which significantly enhanced my learning experience. To my wonderful colleagues in the spintronics group (Anamul, Lakhan, Khadiza, Lars, Maha, Divya, Sameer, Ankit, Richa, Enling, Harald, Jonathan, Ivo, Naoto, Dmitrii, and Bogdan) it has been a privilege working alongside each of you. Thank you for the great times and for fostering a collaborative environment within the group.

I am grateful to our collaborators, Professor Johan Åkerman, Professor Biplab Sanyal, Professor Peter Svendlindh, Soheil Ershadrad, Rahul Gupta, and Craig Polley, for the fruitful discussions.

I would also like to extend my gratitude to the MyFab staff who have been very enthusiastic in helping with our cleanroom processes. Thank you to Henrik, Niklas, Marcus, Mats, Mattias, and Petra. I would also like to thank Annika, Susannah, and Deborah for the administrative support during my studies.

To my colleagues at QDP, thank you for the generosity, openness, laughter, and memorable fikas. I wish you all continued success in your future endeavors. I am extremely grateful for newfound friends - Adithi, Aditya, Alessia, Johanna, Joyal, Kiryl, Klinti, Lars, Maha, Munis, Na, Naveen, Núria, and Richa.

To Amay, Dianne, Merle, Jessy, Kenneth, Tom, Anjelou, Deb, Juno, Carlo, for keeping a piece of home thriving here in Gothenburg, maraming salamat. To Mitch, Shern, and Kim, thank you for the low-maintenance friendship.

To my family, thank you for the unwavering support and love. This is as much your achievement as it is mine. Agyaman ak kadakayo amin. Till Nicholas, min största hejaklack, tack så jättemycket för att du finns.

LIST OF PUBLICATIONS

This thesis is based on the work contained in the following appended papers:

[I] B. Zhao, R. Ngaloy, S. Ghosh, S. Ershadrad, R. Gupta, K. Ali, A. M. Hoque, B. Karpiak, D. Khokhriakov, C. Polley, B. Thiagarajan, A. Kalaboukhov, P. Svedlindh, B. Sanyal, and S. P. Dash, "A Room-Temperature Spin-Valve with van der Waals Ferromagnet Fe5GeTe2/Graphene Heterostructure", en, Advanced Materials **35**, 2209113 (2023).

[II] R. Ngaloy, B. Zhao, S. Ershadrad, R. Gupta, M. Davoudiniya, L. Bainsla, L. Sjöström, M. A. Hoque, A. Kalaboukhov, P. Svedlindh, B. Sanyal, and S. P. Dash, "Strong In-Plane Magnetization and Spin Polarization in $(Co_{0.15}$ $Fe_{0.85}$ $)_5$ $GeTe_2$ /Graphene van der Waals Heterostructure Spin-Valve at Room Temperature", en, ACS Nano, acsnano.3c07462 (2024).

[III] B. Zhao, R. Ngaloy, L. Sjöström, and S. P. Dash, "All-Electrical Detection of Spin-textures in van der Waals Magnet", submitted to Advanced Materials (2025).

[IV] R. Ngaloy, L. Bainsla, L. Pandey, H. Bangar, B. Zhao, M. Khademi, J. Åkerman, and S. P. Dash, "Magnetization Dynamics of Beyond Room Temperature van der Waals Ferromagnets", submitted to npj Spintronics (2025).

[V] R. Ngaloy, L. Pandey, P. Rout, H. Bangar, B. Zhao, and S. P. Dash, "Self-induced spin-orbit torque in van der Waals ferromagnet Fe3GaTe2 at room temperature", Manuscript (in preparation).

OTHER PUBLICATIONS NOT INCLUDED IN THIS THESIS

1. Bing Zhao, Lakhan Bainsla, Soheil Ershadrad, Lunjie Zeng, **Roselle Ngaloy**, Peter Svedlindh, Eva Olsson, Biplab Sanyal, and Saroj P. Dash. "Coexisting Non-Trivial Van der Waals Magnetic Orders Enable Field-Free Spin-Orbit Torque Magnetization Dynamics." Advanced Materials (2025): 2502822..
2. Pandey, Lalit, Bing Zhao, Karma Tenzin, **Roselle Ngaloy**, Veronika Lamparská, Himanshu Bangar, Aya Ali et al. "Energy-efficient field-free unconventional spin-orbit torque magnetization switching dynamics in van der Waals heterostructures." arXiv preprint arXiv:2408.13095, Accepted in Nature Communications, August 2025.
3. Viney Ghai, Santosh Pandit, Magnus Svensson, Ragnar Larsson, Aleksandar Matic, **Roselle Ngaloy**, Saroj P. Dash et al. "Achieving Long−Range Arbitrary Uniform Alignment of Nanostructures in Magnetic Fields." Advanced Functional Materials 34, no. 42 (2024): 2406875.
4. Viney Ghai, Ases Akas Mishra, Enling Huang, **Roselle Ngaloy**, Saroj P. Dash, Aleksandar Matic, and Roland Kádár. "Halbach Array Induced Magnetic Field Alignment in Boron Nitride Nanocomposites." Advanced Science 12, no. 6 (2025): 2408532.
5. **Roselle Ngaloy***, Naoto Yamashita*, Bing Zhao, Soojung Kim, Marlis N. Agusutrino, Soobeom Lee ... & Dash, S.P. (2025). Deterministic spin-orbit torque switching of epitaxial ferrimagnetic insulator with perpendicular magnetic anisotropy fabricated by magnetron sputtering. Accepted in npj Spintronics, August 2025.

Abbreviations and Symbols

2D	Two-dimensional
vdW	van der Waals
PMA	Perpendicular magnetic anisotropy
SOT	Spin orbit torque
FGT	$\mathrm{Fe_5GeTe_2}$
CFGT	$(\mathrm{Co}_0.15\mathrm{Fe}_0.85)_5\mathrm{GeTe}_2$
NFGT	$(\mathrm{Ni}_0.40\mathrm{Fe}_0.60)_5\mathrm{GeTe}_2$
SPV	Spin valve
SOC	Spin-orbit coupling
SOT	Spin orbit torque
SSOT	Self-induced spin orbit torque
FMR	Ferromagnetic resonance
AHE	Anomalous Hall effect
PHE	Planar Hall effect
ST	Spin texture
SD	Single domain

Symbols

M_s	Magnetization saturation
T_C	Curie temperature
T_N	Néel temperature
H_C	Coercive field
H_k	Anisotropy field
M_{eff}	Effective magnetization
H_R	Resonance field
γ	Gyromagnetic ratio
g	Landé g-factor
ΔH_0	Linewidth broadening
α	Gilbert damping constant
τ_s	Spin lifetime
$\mathrm{P}_i n$	Injector's spin polarization
$\mathrm{P}_d e$	Detector's spin polarization
σ_{xx}	longitudinal conductivity
D_s	Spin diffusion coefficient
$\lambda_g r$	Spin diffusion length in graphene
L_{ch}	Channel length
ω	Larmor spin precession frequency
θ_{SH}	Spin Hall angle
σ_{xy}	Anomalous Hall conductivity
σ_{SHC}	Spin Hall conductivity
H_{DL}	Damping-like SOT field
H_{DL}	Field-like SOT field

Constants

e	Electron charge: $\mathrm{e} = 1.602 \times 10^{-19}$ C
$\hbar$	Reduced Planck's constant
μ_B	Bohr magneton: $\mu_B = 9.274 \times 10^{-24}\mathrm{JT}^{-1}$

CONTENTS

1 Introduction

Spintronics, or spin electronics, utilizes the electron's spin degree of freedom to write, store, and read information in solid-state devices [1]. Giant magnetoresistance (GMR)[2, 3], tunnel magnetoresistance (TMR) [4, 5], and spin transfer torque (STT) [6, 7] have become the core concepts in efficient generation, manipulation, and detection of spin-polarized current within metallic materials. GMR and TMR describes the change in the electrical resistance of a multilayer stack as a result of the relative magnetic or spin orientation of the ferromagnetic layers while STT is used to change this relative orientation by using a spin polarized current to directly transfer angular momentum and switch the ferromagnet's orientation. Additionally, spin orbit torque (SOT), an emerging technology, drives a transverse spin current from a high spin orbit material to manipulate an adjacent ferromagnet. Unlike conventional purely charge-based electronics, spintronics offers nonvolatile operation leading to minimal standby power, and the possibility of integrating logic and memory to overcome the von Nuemann architecture achieving faster processing speeds.

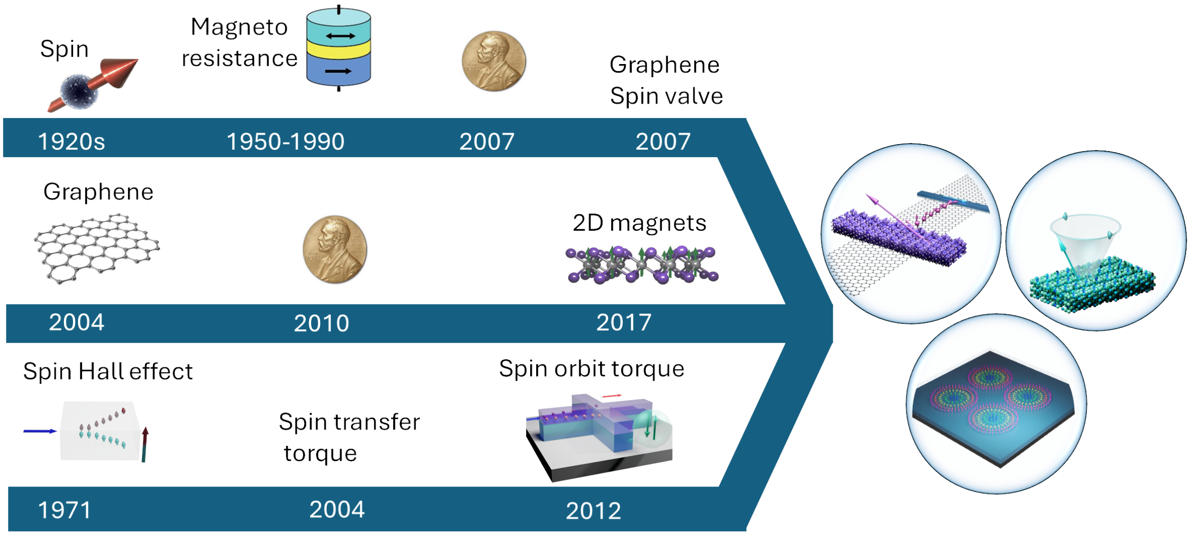

Figure 1.1: Timeline of key discoveries in the field of spintronics towards the realization of the work done in this dissertation.

In more than two decades, spintronic devices, particularly memory devices, have matured from a fundamental proof of concept to commercially available components. Spintronics offers a range of promising options such as magnetic random access memories(STT and SOT) [8–11], racetrack memory [12], spin logic [13], magnonic devices [14], and neuromorphic computing. Despite these advances, several critical challenges remain. One of the fundamental problems in spintronics is overcoming the spin conductance mismatch between ferromagnets and nonmagnetic materials to maintain efficient spin injection and detection. Interface engineering has also become a key factor as interdiffusion, interface degradation, and uncontrolled hybridization at the interfaces limit device performance and reproducibility. Moreover, conventional spintronic devices use ultrathin ferromagnets such as CoFeB to obtain interfacial perpendicular magnetic anisotropy. Although perpendicular magnetic anisotropy (PMA) ferromagnets are desired for high density devices, they are achieved through complicated multilayers of alternating magnetic and nonmagnetic layers, making them more sensitive to surface and interface effects. Atomically thin quantum materials like two dimensional (2D) magnets are a promising solution to address these challenges.

Van der Waals magnets

The isolation of graphene in 2004 [15] initiated the exploration of atomically thin materials with properties that are distinct compared to their bulk counterparts. Until 2017, magnetic order in purely two-dimensional (2D) crystals remained elusive due to Mermin-Wagner theorem [16], which forbids long-range magnetic order in an isotropic 2D Heisenberg system at finite temperatures. This barrier was overcome by the discovery of intrinsic ferromagnetism in monolayer and few-layer van der Waals (vdW) crystals, which was first demonstrated in CrI_3 [17] and independently in $Cr_2Ge_2Te_6$ [18]. In these seminal works, they have reported clear hysteresis loops and layer-dependent remanent magnetization down to the monolayer limit, firmly establishing a magnetic class of 2D layered materials stabilized by magnetocrystalline anisotropy. Throughout this dissertation, the terms vdW magnet and 2D magnet will be used interchangeably.

Since those initial reports, the library of 2D magnets has grown rapidly to include ferromagnets, antiferromagnets, ferrimagnets, and materials exhibiting more exotic spin textures [19–21]. These inlcudes metallic Fe_3GeTe_2 [22], semiconducting VI_3 [23], insulating $MnPS_3$ [24], and topological insulator $MnBi_2Te_4$ [25], among others, which highlights the diversity in magnetic anisotropy, magnetic ground state, electronic structure, and spin-orbit coupling strength.

Moreover, 2D magnets exhibit thickness-dependent magnetism, where their magnetic ordering can drastically change in few-layer or bilayer forms, leading to fascinating interlayer effects [26]. Pressure, strain, or electrostatic gating can also tune the magnetic order of these materials, effectively controlling phase transitions between paramagnetic, ferromagnetic, and antiferromagnetic states [27–31]. Beyond these intrinsic 2D magnets, heterostructures that combine them with graphene, transition metal dichalcogenides (TMDs), or topological insulators (TIs) have revealed proximity-induced magnetic effects, spin filtering, and even novel quantum states that could be harnessed for future quantum technologies [26, 32–35].

Van der Waals magnets in spintronics

Despite these exciting discoveries, several challenges remain before 2D magnets can be fully integrated into practical applications. One major limitation is the low Curie temperatures (Tc) of most known 2D magnets, which typically require cryogenic conditions to maintain magnetic order. Achieving robust room-temperature magnetism is a key goal for the field, with promising candidates such as Fe_5GeTe_2 and Fe_3GaTe_2, and their doped counterparts, exhibiting relatively high Curie temperatures and tunable magnetic properties. Beyond technological considerations, the exploration of fundamental phenomena in 2D magnets is an exciting avenue for research [36–38].

This dissertation investigates the physical properties of 2D magnets, including spin polarization, doping-dependent magnetization and anisotropy, magnetization dynamics, and intrinsic spin orbit torque. First, the static and dynamic properties of beyond room temperature 2D magnets were studied independently. After which, they were integrated into spintronic devices such as graphene spin valves and SOT devices, where their magnetic properties can be controlled, probed, and manipulated. This thesis is structured as follows:

Chapter 2 presents a comprehensive overview of related research studies on 2D magnets to contextualize the impact and contributions of the thesis at a broader perspective.

Chapter 3 introduces the vdW itinerant ferromagnets Fe_5GeTe_2 (FGT),$(Co_{0.15}Fe_{0.85})_5GeTe_2$ (CFGT), and $(Ni_{0.40}Fe_{0.60})_5GeTe_2$ (NFGT). The static and dynamic magnetic properties of these vdW ferromagnets in bulk form is presented. From temperature-dependent superconducting quantum interference device (SQUID) measurements at different magnetic field orientations, we were able to identify the Curie temperature, T_C, magnetic saturation, coercivity, remanence, and anisotropies. Broadband ferromagnetic resonance (FMR) spectroscopy was conducted in the $5-30$ GHz frequency range at room temperature to further examine their magnetization dynamics (*Paper IV*). Relevant magnetic dynamic parameters such as effective magnetization, anisotropy field, Gilbert damping constant, and gyromagnetic ratio (or equivalently the Landé g-factor) were extracted. For spintronics applications, the aim is to maintain thermal stability while lowering power consumption which can be achieved by materials with high spin polarization, moderate magnetic saturation, and anisotropy field but with low damping constant. The results show that NFGT exhibits enhanced effective magnetization and a higher damping constant while FGT, and CFGT demonstrate lower effective magnetization, anisotropy, and damping constant. Further analysis of their gyromagnetic ratios suggests a potential orbital contribution to their magnetization.

In Chapter 4 we continue to probe FGT and CFGT by incorporating them into spin valve devices. Spin injection and detection of FGT (*Paper I*) and CFGT (*Paper II*) in graphene spin valves is presented. Room temperature spin transport measurements in non-local spin valve configuration enable the observation of characteristic spin valve switching for both FGT/graphene and CFGT/graphene devices. The room temperature spintronic properties of FGT and CFGT are characterized by negative spin polarization while dynamic measurements reveal canted magnetic moments in FGT and in-plane magnetic anisotropy in CFGT, highlighting the modulation of spin polarization and magnetic anisotropy with magnetic doping.

Chapter 5 discusses engineered spin textures in graphene from FGT. We investigated the injection, transport, and detection of spin current with distinct spin textures originating from FGT with constrictions and notches (*Paper III*) in graphene spin valves. This results in spins with special textures in graphene which are then detected by conventional cobalt ferromagnets. This approach enables the electrostatic control and detection of spin polarizations associated with different spin textures, leading to anomalous multi-level spin valve switching and Hanle spin precession signals. The analysis suggests that the presence of notches or constrictions in FGT disrupts magnetic domains, resulting in the coexistence of spin textures and conventional single domain structures in FGT.

In Chapter 6, we investigate the high T_C PMA ferromagnet Fe_3GaTe_2 *(Paper V)*. Results show a strong nonlinear Hall effect and self-induced spin-orbit torque in Fe_3GaTe_2, which remains magnetic up to 370 K. Temperature-dependent anomalous Hall effect measurements and scaling analysis reveal large anomalous Hall angle while second harmonic Hall measurements were performed to quantify the self-induced spin-orbit torque (SSOT) which is dominated by the damping-like torque. Switching experiments demonstrated that SSOT can partially switch the magnetization when assisted by an in-plane field, consistent with the expected spin orbit torque geometry.

Lastly, in Chapter 7, a summary of the thesis will be presented together with future perspectives or outlook towards further studies on vdW magnets in spintronics.

2 State of the art: van der Waals magnets in spintronics

The successful demonstration of intrinsic magnetism in two-dimensional (2D) layered materials in 2017 marked a major breakthrough in understanding magnetic order at the 2D limit. Building on decades of progress in spintronics, the integration of 2D magnets with emerging material platforms such as graphene and other 2D quantum materials has opened new directions, not only for uncovering novel physical phenomena and enabling next-generation device concepts, but also for probing magnetism at the atomic scale and advancing fabrication techniques. Together, these developments are tranforming spintronics research.

This chapter provides an overview of the recent developments and the current state of magnetic van der Waals (vdW) materials. Specifically, we focus on recent advancements in spin valve (SPV) devices, and the fundamental interactions that govern their functionality. In addition, we also discuss the state of the art in spin orbit torque (SOT) with 2D magnets and the emerging self-induced spin orbit torques (SSOT) in 2D ferromagnets. These lay the groundwork for future all-vdW spintronic architectures.

2.1 Magnetism in the two-dimensional limit

Magnetic order originates from the antisymmetric nature of the electron wavefunction and is determined by exchange interactions between neighboring spins. Direct exchange occurs when the electron wavefunctions on neighboring atoms overlap significantly, where the degree of overlap determines the kind of magnetic order [39]. In contrast, superexchange describes the magnetic interactions in insulating and semiconducting materials, where the coupling is mediated by non-magnetic anions. In such systems, the magnetic ground state is largely dictated by bond geometry, while the strength of the interaction is predicted by orbital occupancy [40]. In itinerant magnets, magnetic coupling is described by the Ruderman-Kittel-Kasuya-Yosida (RKKY) interaction, where conduction electrons mediate long-range exchange. This mechanism can stabilize ferromagnetism, antiferromagnetism, and even complex spin structures such as spin spirals [41–43].

Motivated by the robust magnetism found in bulk systems such as Fe, Co, Ni, and their alloys, extensive efforts have been made to realize magnetic order in

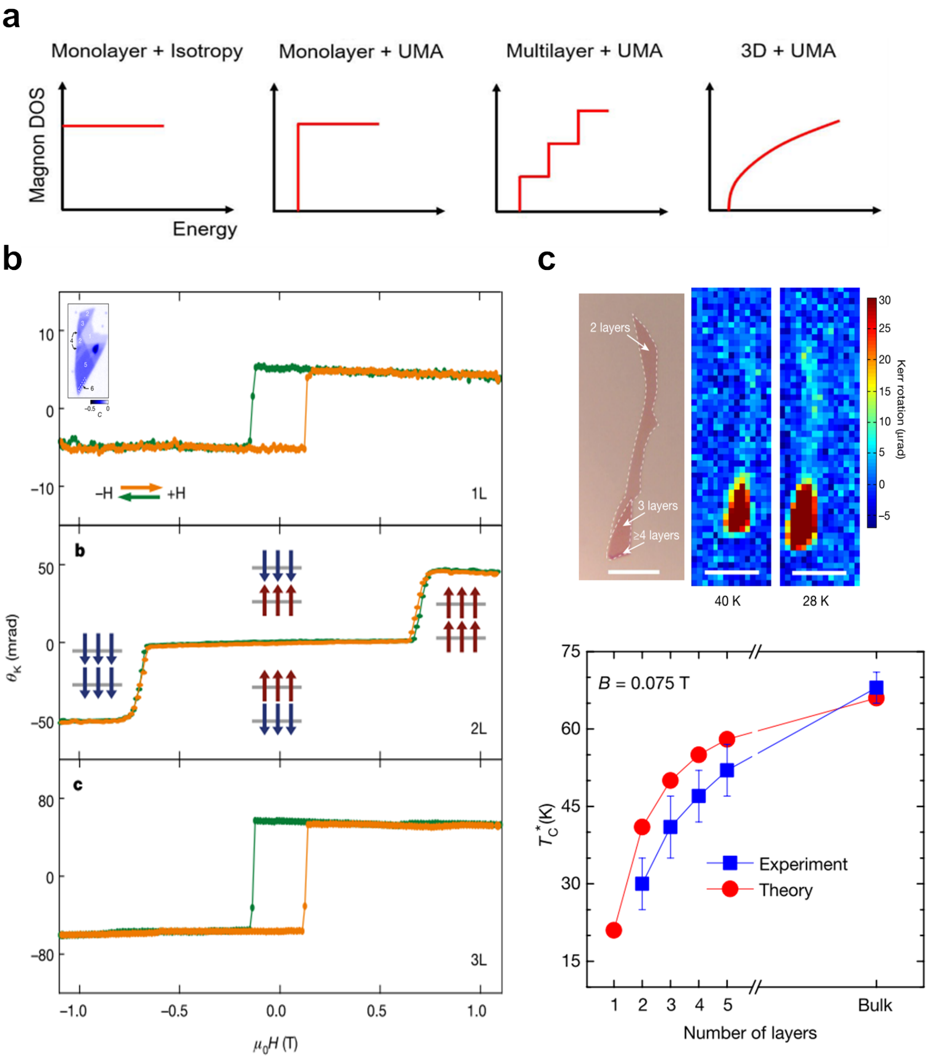

Figure 2.1: Magnetism in the two-dimensional limit and the library of van der Waals mangets. a. Evolution of magnon density of states (DOS) for a 2D isotropic Heisenberg ferromagnet for different number of layers. Uniaxial magnetic anisotropy (UMA) opens a spin-excitation gap, stabilizing long range magnetic order. Adapted from [20]. **b.** MOKE measurements for monolayer (top), bilayer (middle) and trilayer (bottom) CrI_3, indicating ferromagnetic intralayer and antiferromagnetic interlayer order. Adapted from [17] **c.** Optical image (top left) and Kerr rotation signal (top right) of a few layer $Cr_2Ge_2Te_6$ under 0.075 T magnetic field showing magnetic order in bilayer $Cr_2Ge_2Te_6$ at 28 K. Layer dependent T_C (bottom panel) from experimental (MOKE) and theoretical calculations revealing strong dimensionality effect [18]

.

reduced dimensions through epitaxial thin films of these bulk magnetic materials. However, at low dimensions these films often encounter inherent limitations, including surface inhomogeneity, irregular morphology, interfacial hybridization, and poor reproducibility of their magnetic properties [44–46]. Moreover, in the context of 2D magnetism, the Mermin–Wagner theorem poses a fundamental limitation. It predicts that strictly 2D systems with continuous spin symmetry and short-range interactions cannot exhibit long-range magnetic order at finite temperatures, due to divergent long wavelength spin wave fluctuations[16]. In other words, at finite temperatures, the abrupt onset of the magnon density of states (DOS) prevents the persistence of long-range magnetic order in such a system. However, magnetic anisotropy, typically arising from spin orbit coupling, breaks the continuous spin symmetry and opens a gap in the spin wave spectrum. This gap suppresses thermal excitations at low energies, enabling the stabilization of long-range magnetic order in 2D (Figure 2.1)a.

This explains the breakthrough observation of intrinsic magnetism in atomically thin van der Waals magnets such as CrI_3 and $Cr_2Ge_2Te_6$ [17, 18], where the presence of uniaxial magnetic anisotropy allows magnetic order to persist at finite temperatures. While the Mermin–Wagner theorem highlights the intrinsic instability of 2D magnetic order in isotropic systems, it also underscores the essential role of magnetic anisotropy in stabilizing magnetism in 2D materials.

CrI_3 is a semiconductor Ising antiferromagnet, demonstrating a strong out-of-plane magnetic anisotropy which originates from the large spin orbit coupling in iodine [76]. Magnetic order was reported to persist down to a monolayer up until 45 K, as observed through magneto-optical Kerr effect (MOKE) [17]. Additionally, layer-dependent magnetism was shown where odd-even effects are prominent due to ferromagnetic intralayer and antiferromagnetic interlayer ordering as shown in Figure 2.1b. For even number of layers, a metamagnetic transition is observed, which has been shown to be controllable with gate [77, 78].

In an independent study, ferromagnetic order in $Cr_2Ge_2Te_6$ was also reported through ferromagnetic loops measured by MOKE measurements, which revealed ferromagnetic hysteresis loops with small but finite remanent magnetization (Figure 2.1c). Due to its inherently weak mangetic anisotropy, an external magnetic field is used to stabilize long-range order to achieve a finite Curie temperature (T_C) [18]. Under an applied field of 0.075 T, a bilayer CGT undergoes a ferromagnetic transition at about 30 K (68 K in bulk). More importantly, $Cr_2Ge_2Te_6$ is one of the first experimentally confirmed 2D Heisenberg ferromagnets.

Since these reports, more 2D magnetic compounds have been realized, building a whole library encompassing not only ferromagnets such as Fe_3GeTe_2 [22] but also antiferromagnets including MnP_3 [68] and $FePS_3$ [48]. A summary of 2D magnets are presented in Figure 2.2, showing a wide variety of magnetic orders and electronic behaviors. These systems also host different anisotropies, and tunability, establishing a versatile platform for both fundamental studies and device explorations.

Another critical milestone was the realization of room temperature ferromagnetism in Fe_5GeTe_2 [51] and in Fe_3GaTe_2 [47]. This highlights the potential of

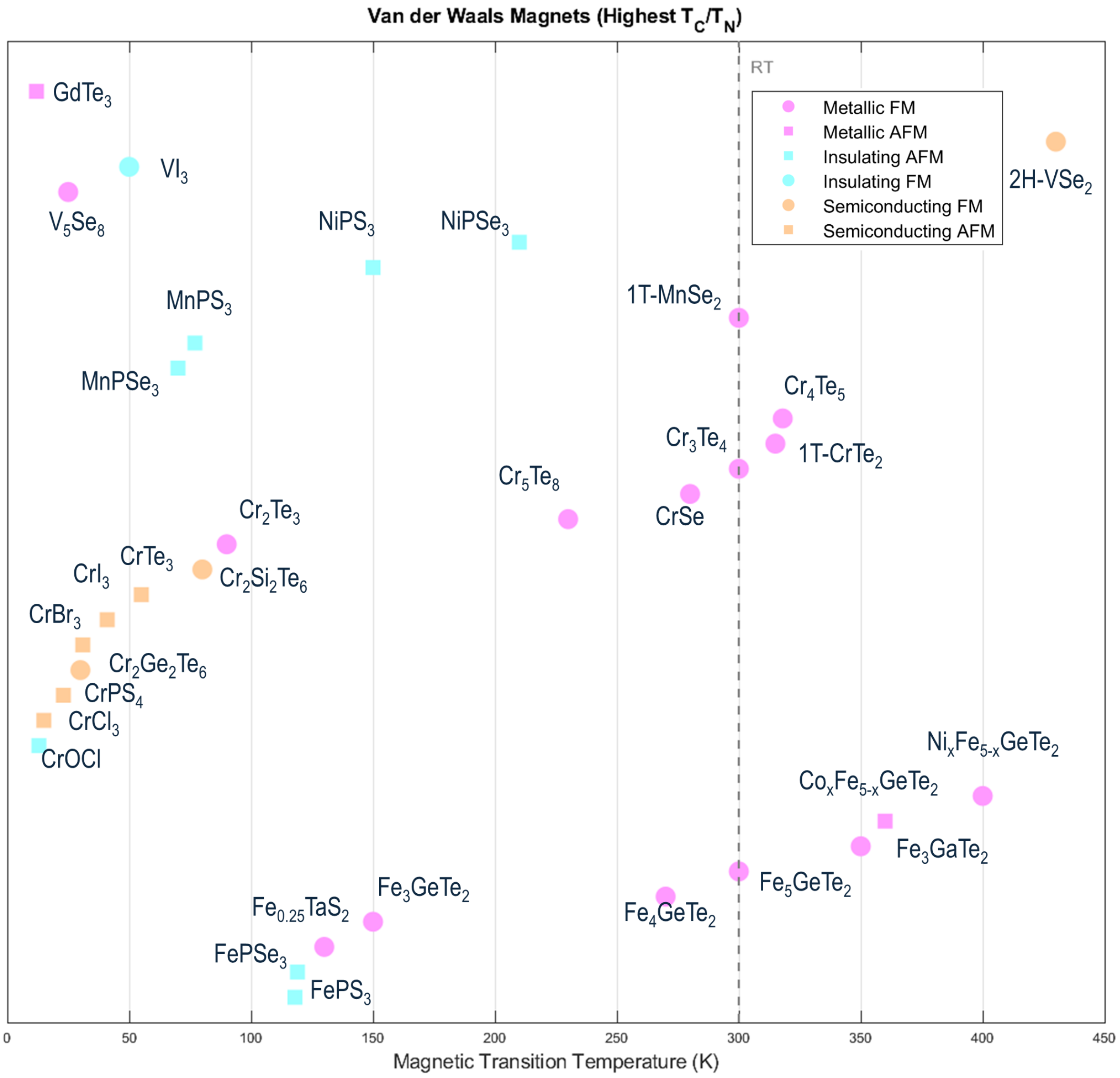

Figure 2.2: The library of van der Waals mangets. Current library of van der Waals magnets and their highest reported T_C or T_N. These includes ferromagnets (circles) and antiferromagnets (squares) with different electrical properties: insulating (cyan), semiconducting (yellow), metallic (magenta) [17, 18, 22, 47–75]

integrating 2D magnets into practical spintronic devices that operate at ambient temperatures. On-going progress is anticipated in stabilizing more high-T_C 2D magnets through doping and strain engineering. However, a central challenge moving forward lies in bridging advances in fundamental physics with scalable and reliable fabrication pathways to enable future commercialization.

2.2 Spintronic phenomena with van der Waals magnets

2.2.1 Spin valve devices with van der Waals magnets

Spin valves represent one of the most important spintronic device architectures, exploiting the giant magnetoresistance (GMR) [2, 3] or tunneling magnetoresistance (TMR) [4, 5] effects to achieve magnetic field-dependent electrical resistance. Spin valves are typically constructed from bulk ferromagnetic electrodes separated by either a metallic or insulating spacer, enabling controlled spin-dependent electron transport. By contrast, spin valves built from two-dimensional magnets open a new avenue for device engineering: the atomically thin nature of layered materials, combined with their atomically sharp van der Waals interfaces, offers cleaner and more tunable junctions. This eliminates issues of lattice mismatch and interfacial disorder that commonly limit traditional heterostructures.

Magnetic tunnel junctions (MTJs) or vertical tunneling spin valves are devices with ferromagnet and insulating spacer stacked vertically, as shown in Figure 2.3. These devices rely on the change in tunneling resistance as the magnetization of the FM electrode changes. The tunneling current is proportional to the electron density of states (DOS) of the electrodes which in ferromagnets is intrinsically spin split, meaning that the majority (spin-up) and minority (spin-down) bands exhibit different DOS profiles depending on the magnetization direction. As a result, the junction resistance varies with the alignment of the FM layers. When the magnetizations are parallel, spin-polarized electrons tunnel efficiently, yielding the lowest resistance state (R_P).Conversely, when the magnetizations are antiparallel, spin filtering suppresses tunneling, leading to the highest resistance state (R_AP). The relative contrast between these two states defines the tunneling magnetoresistance (TMR) ratio, a key performance metric for MTJs:

$$TMR = \frac{R_{AP} - R_P}{R_P} \times 100\% \tag{2.1}$$

Wang et al. [79], demonstrated a tunneling spin valve device (shown in Figure 2.3a using few nanometer thick Fe_3GeTe_2 ferromagnetic electrodes separated by an atomically thin hexagonal boron nitride (hBN) as a tunnel barrier. The device exhibited a tunneling magnetoresistance (TMR) ratio as high as 160%, corresponding to a spin polarization of 0.66 for the FGT electrodes. This enhanced performance, surpassing conventional magnetic tunnel junctions, was attributed to the atomically sharp and clean interfaces formed between the electrodes and the hBN barrier. Replacing hBN with graphite yielded Fe_3GeTe_2/graphite/Fe_3GeTe_2 heterostructures exhibiting antisymmetric MR with an intermediate resistance state, explained by Rashba SOC–induced spin–momentum locking at the interfaces [93]. Depending on the relative alignment between spin polarization and

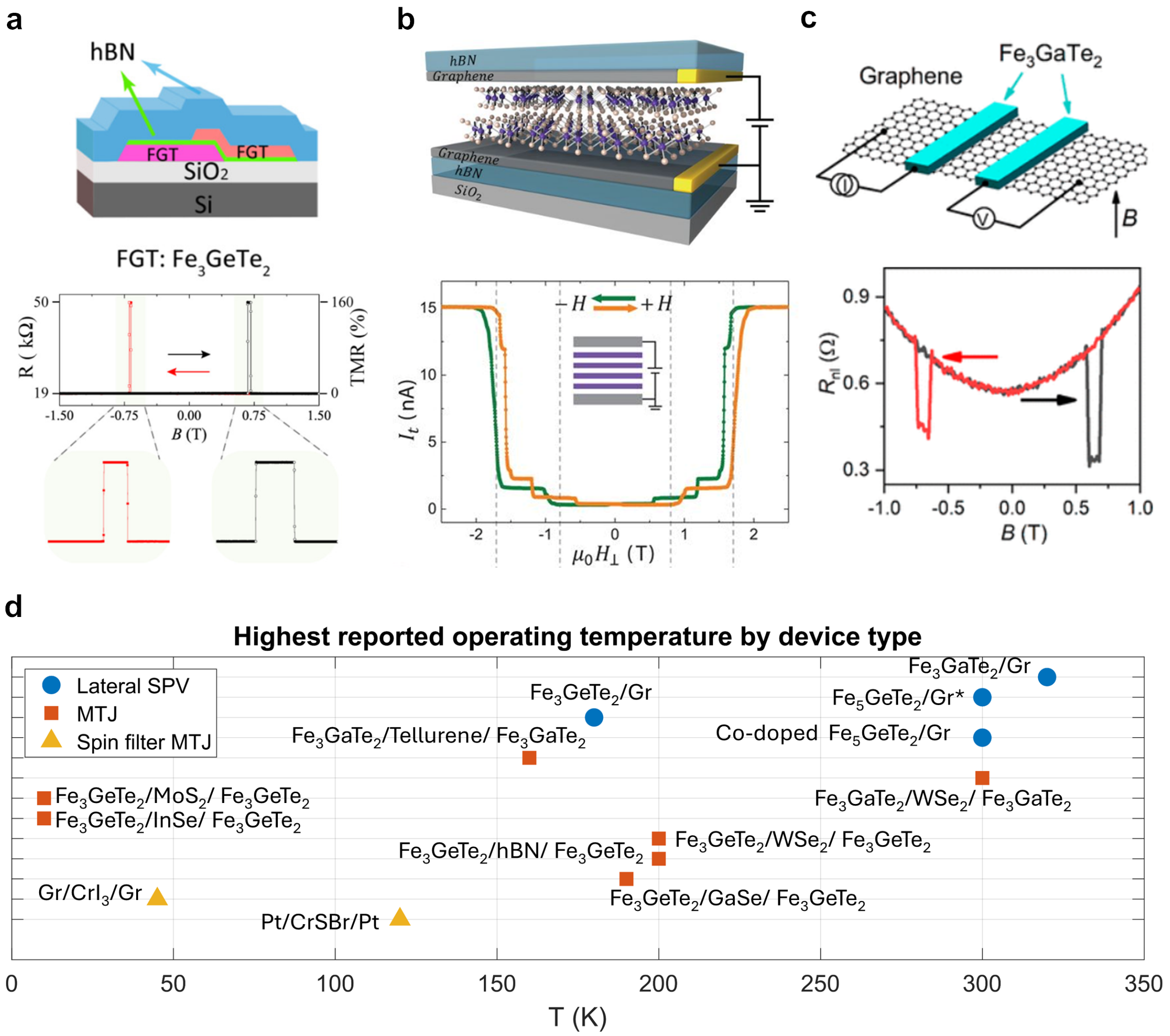

Figure 2.3: Van der Waals magnets in spin valves a. Tunneling spin valve from Fe$_3$GeTe$_2$/hBN/Fe$_3$GeTe$_2$ showing the spin valve effect corresponding to tunneling magnetoresistance of ∼ 160% measured at 4.2 K. Adapted from [79] **b**. Spin-filter effect in graphene/CrI$_3$/graphene tunnel junction with TMR reaching 19,000% at 2 K. Adapted from [26] **c**. All-vdW lateral spin valve with Fe$_3$GaTe$_2$/graphene heterostructure, with the nonlocal spin valve signature measured at 100 K. Adapted from [80]. **d**. Summary of 2D magnet-based spin valve devices which includes magnetic tunnel junctions, spin filter magnetic tunnel junctions, and lateral spin valves. The data were obtained from [26, 79–92].

magnetization at the two interfaces, low, intermediate, or high MR states were obtained. These results highlight the ability of vdW heterostructures to uncover unconventional spin transport phenomena. Importantly, room-temperature operation with TMR ratios of 50% has been achieved inFe$_3$GaTe$_2$/WSe$_2$/Fe$_3$GaTe$_2$ junctions [90] demonstrating the practical viability of 2D MTJs for memory applications.

Song et al. [26] and Klein et al. [94] demonstrated that magnetic tunnel junctions employing a magnetic insulator as the tunnel barrier can yield giant tunneling magnetoresistance, reaching values as high as 19,000% [26]). This behavior arises from the spin-filter effect, where tunneling through a magnetic insulator produces spin-dependent barrier heights, leading to different tunneling rates for spin-up and spin-down electrons. Consequently, the observed magnetoconductance strongly reflects the exponential sensitivity of tunneling current to the barrier's electronic structure. A notable example is the graphite/ CrI_3/graphiteheterostructure (Figure 2.3b), which acts as a multilayer spin-filter device due to the interlayer antiferromagnetic ordering and metamagnetic transitions in CrI_3. Beyond enabling enhanced device performance, such structures also provide a powerful platform to probe the intrinsic magnetic properties of 2D magnets, offering an electrical alternative to conventional microscopy techniques such as MOKE and Lorentz transmission electron microscopy (TEM).

For lateral spin valve devices based on graphene transport channels, the first demonstration of room-temperature spin injection and detection using a vdW magnet was achieved with Fe_5GeTe_2-graphene heterostructures [81]. Efficient spin injection was observed, with a negative spin polarization of 45% in Fe_5GeTe_2. This large interfacial polarization arises not only from the high saturation magnetization of Fe_5GeTe_2 benefitted not only from the high magnetization saturation of Fe_5GeTe_2 but also from the atomically sharp interface and vdW gap, with enhanced tunneling barrier properties compared to conventional thin films. Angle-dependent spin precession measurements further revealed that Fe_5GeTe_2 exhibits canted magnetization at room temperature. More recently, Pan et al. [80], reported the first all-vdW heterostructure lateral spin valve using Fe_3GaTe_2 (Figure 2.3c) with robust nonlocal spin valve signals persisting up to 320 K. Together, these advances highlight the potential of vdW ferromagnet/graphene interfaces for efficient spin injection. Moreover, the sensitivity of spin valves and nonlocal measurements geometries at the ferromagnet/graphene interfaces opens new possibilities for an all-electrical probe of spin textures.

2.2.2 Spin orbit torque and magnetization dynamics in van der Waals magnets

Spin orbit torque is a promising approach for energy-efficient magnetization switching in next-generation spintronic devices. The discovery of 2D magnetic materials has pushed forward research in SOT devices, providing a platform for exploring novel spin orbit phenomena. This section examines the current state of spin orbit torque research in 2D magnetic systems, as well as the emerging self-induced spin orbit torque.

For next-generation nonvolatile, magnetic memory devices, SOT has been established as an improvement over spin transfer torque (STT) based technolo-

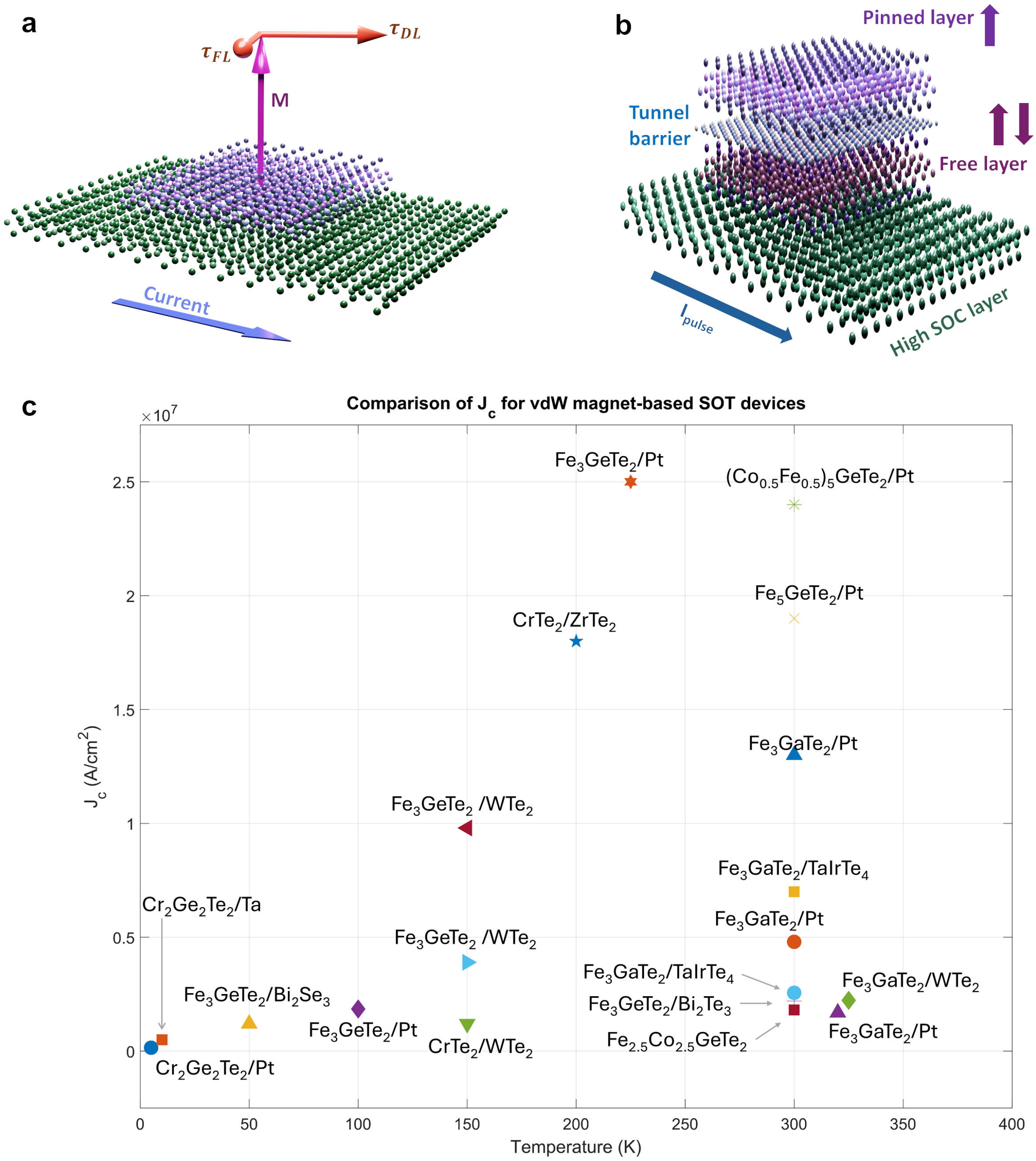

Figure 2.4: Van der Waals magnet-based spin obit torque devices a. A van der Waals heterostructure spin orbit torque device. The high spin orbit coupling material provides the spin orbit torque that acts to switch the magnetization M of the ferromagnet. **b**. A comparison of the critical switching current density in 2D magnet-based SOT devices. The operating temperature of the devices are shown in the x-axis. Data were obtained from [95–111]. **c**. An all van der Waals heterostructure of a memory component, integrating a magnetic tunnel junction for the read-out and an SOT device for magnetization switching. Higher operating temperature and lower switching currents are desired.

gies. For both SOT and STT, magnetization is switched using electrical current induced-torques, which is attractive for integration in electronic devices. STT has already been successfully utilized in magnetic random-access memory (STT-MRAM) [112]. However, several problems are limiting its performance and device integration: (1) high switching current, (2) slow switching time in few nanoseconds, and (3) device instability due to coupled read and write paths [113]. In contrast, SOT-based devices are implemented in a three terminal magnetic tunnel junction (MTJ) design, where a high in-plane pulse current is introduced to switch the magnetization and a low vertical current is used to detect the magnetization state, separating the read and write paths. The separation of read and write paths significantly improves device enudrance and reliability [11, 114].

For SOT, two layers are needed to build a device (as illustrated in Figure 2.4a). First is a high spin orbit coupling (SOC) material as a spin source layer, which converts charge current to spin current, via spin Hall effect (SHE) or Rashba-Edelstein effect (REE) [115]. Conventional spin sources include heavy metals (HM) such as Pt, Ta, W, and their alloys - materials exhibiting giant spin Hall effect. In addition to this, recent works have been directed towards exploring other van der Waals materials with high SOC and rich band structures; such as topological semimetals and insulators, and transition metal dichalcogenides (TMDs) where charge-to-spin conversion could originate from bulk, surface, or a combination of both [116]. The second layer is the magnetic layer, which provides the switchable magnetization states corresponding to the memory states.

In conventional magnet/HM heterostructures, a charge current is injected (along the y-axis) to the high SOC material resulting to a propagation of spin current in the out-of-plane direction (z-axis). Spin current from the spin source layer will propagate to at the interface to the magnetic layer and by the transfer of angular momentum, can switch the magnetization direction of the magnet. In high spin orbit coupling materials that are characterized by conventional charge-to-spin conversion, given the device geometry, the resulting spin polarization is along the x-axis leading to in-plane torques (field-like and damping-like) and hence can only deterministically switch an in-plane magnet. Ideally, magnets with perpendicular magnetic anisotropy (PMA) are desired to achieve fast (sub-nanosecond) switching and high-density devices. So, to utilize the in-plane damping torque in switching a PMA magnet, a small in-plane magnetic field is used to break the symmetry of the device. Field-assisted switching has been successfully demonstrated in $Cr_2Ge_2Te_6$/Ta [96], $Cr_2Ge_2Te_6$/Pt [95], Fe_3GeTe_2/Pt [99], Fe_3GeTe_2/Bi_2Te_3[117], Fe_3GaTe_2/Pt [110], and in all-vdW heterostructures of Fe_3GeTe_2/WTe_2 [100].

As field-assisted switching add further complications to device design, efforts have been directed towards circumventing this limitation. Among the solutions, is the utilization of low symmetry materials with unconventional charge-to-spin conversion such as WTe_2 and $TaIrTe_4$ to obtain out-of-plane torques [118–120]. Successful field-free switching have been demonstrated in Fe_3GeTe_2/WTe_2 [101],

Fe_3GaTe_2/WTe_2 [111], Fe_3GaTe_2/$TaIrTe_4$ [91]. Another way to realize deterministic switching is through exchange bias in antiferromagnet/ferromagnet heterostructures such as demosntrated in Co-doped Fe_5GeTe_2/Pt [106] and CrSBr/Fe_3GeTe_2/Pt [121] as well as employing intrinsically canted magnets like Fe_5GeTe_2 [104]. With exchange bias or a canted magnetism, the magnetic inversion symmetry is broken which normally requires the external magnetic field for deterministic magnetization switching.

Another exciting direction in the study of spin orbit torques in 2D magnets, are the emerging reports of self-induced spin orbit torques in 2D ferromagnets, eliminating the traditional requirement of a spin source layer. Recent experimental works have revealed SSOT in Fe_3GeTe_2 and Co-doped Fe_5GeTe_2 [92, 122] originating from crystal symmetry breaking. Materials sharing analogous structural motifs, layer stacking arrangements, or symmetry-reducing atomic environments could potentially demonstrate similar phenomena, providing a rational framework for expanding the library of intrinsic SSOT materials beyond the current examples.

3 Beyond room temperature itinerant van der Waals ferromagnets

This chapter focuses on the static and dynamic magnetic characterization of room temperature itinerant ferromagnets, Fe_5GeTe_2 (FGT), $(Co_{0.15}Fe_{0.85})_5GeTe_2$ (CFGT), and $(Ni_{0.40}Fe_{0.60})_5GeTe_2$ (NFGT). First, their static magnetic properties are systematically investigated using superconducting quantum interference device (SQUID) magnetometry. Measurements of magnetization as a function of temperature and applied magnetic field provide insight into their magnetic phase transitions, anisotropy, Curie temperatures, and coercive fields. In the second section, the magnetization dynamics of FGT, CFGT, and NFGT is explored through broadband ferromagnetic resonance (FMR) spectroscopy over the frequency range of 5-30 GHz at room temperature (*Paper IV*). From these measurements, key dynamic magnetic parameters such as the g-factor, effective magnetization, magnetic anisotropy field, and Gilbert damping constant are extracted, offering a foundational understanding of their suitability for spintronic applications.

3.1 Fe_5GeTe_2 and its doped variants

The family of iron germanium tellurides, Fe_nGeTe_2, $n = 3, 4, 5$, has attracted attention owing to its relatively high T_C, perpendicular magnetic anisotropy (PMA), and metallic conductivity [22, 51, 54, 123]. While Fe_3GeTe_2 was the first itinerant vdW ferromagnet to demonstrate robust magnetism down to the monolayer limit, and Fe_4GeTe_2 further extended the T_C closer to room temperature, Fe_5GeTe_2 composition pushes these boundaries even further.A defining characteristic of Fe_5GeTe_2 is its room-temperature ferromagnetism, with T_C reaching up to 310 K depending on synthesis method, thermal history, and Fe vacancy ordering [51, 124–126]. This tunability arises from its complex crystal structure, which includes multiple inequivalent Fe sublattices, and potential Fe site deficiencies ($Fe_{5-x}GeTe_2$), leading to metastable magnetic phases [127, 128].

As illustrated in Figure 3.1a, Fe_5GeTe_2 crystallizes in layered structure, where five inequivalent Fe sites form buckled honeycomb sublayers separated by Ge-Te bilayers, in a rhombohedral symmetry with space group R3m. Fe1 split sites (1U and 1D) and Ge split sites are shown with half-filled spheres. This complex stacking not only yields enhanced exchange interactions, responsible for its itinerant ferromagnetism at elevated temperatures, but also gives rise to rich spin textures, including Néel type domain walls and chiral spin structures mediated by Dzyaloshinskii-Moriya interactions [129, 130]. Moreover, the interplay between itinerant electrons and localized moments in Fe_5GeTe_2 leads to pronounced magnetotransport effects, such as large anomalous Hall conductivity and gate-tunable coercivity [131, 132].

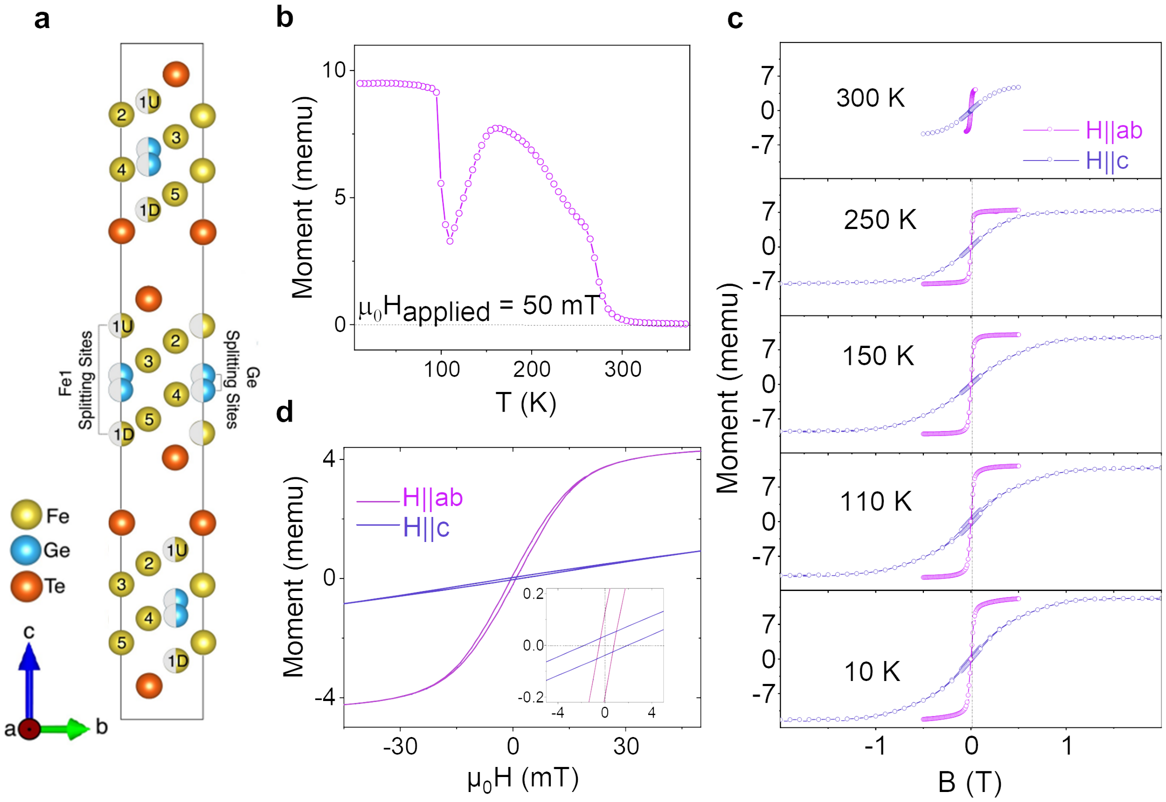

Figure 3.1: SQUID measurements of Fe_5GeTe_2. a. Fe_5GeTe_2 unit cell, showing a layered structure where Fe and Ge atoms are sandwiched between Te planes. The interlayer gap between the Te planes defines the van der Waals gap. Fe and Ge split sites are illustrated in half-filled spheres. **b.** The magnetic moment (M) of bulk Fe_5GeTe_2 as a function of temperature under an applied in-plane magnetic field of 50 mT. **c.** Temperature-dependent magnetic hysteresis loops of the Fe_5GeTe_2 from 10 K to 300 K. **d.** Enlarged magnetic hysteresis loops measured at 300 K reveal finite remanence and coercive fields for both out-of-plane and in-plane response indicating weak anisotropy at room temperature.

3.1.1 The room temperature itinerant ferromagnet Fe_5GeTe_2

Superconducting quantum interference device (SQUID) magnetometry was used to study the static magnetic properties of Fe_5GeTe_2 as shown in Figure 3.1b-

d. SQUID measurements were performed on bulk crystals, which have a planar geometry which allows the orientation of magnetic field along the ab-plane and perepndicular to the plane. Magnetization as a function of temperature (M(T)) under an applied in-plane field of 50 mT is shown in Figure 3.1b. From the M(T) data, we observe a complex temperature dependence with multiple magnetic transitions occurring above 300 K, at 130 K, and at 100 K. The magnetic transition at above 300 K corresponds to the transition from paramagnetic to ferromagnetic state. Further cooling to 130 K reveals a dip in magnetization which corresponds to a spin glassy phase [133], similar to previous reports for quenched FGT crystals [128]. After which, an increase in magnetization is observed at around 100 K, which has been determined to be a magnetostructural transition from a metastable phase before cooling [51, 126, 129]. In reports with further thermal cycling, the magneto-structural transition vanishes and the T_C is enhanced up to 310 K [128, 129]. This complicated behavior is linked to magnetostructural transitions related to the reorientation of the Fe1 moments [51, 134].

The isothermal magnetic hysteresis loops M(H), measured at various temperatures with both in-plane (H||ab) and out-of-plane magnetic fields (H||c), are presented in Figure 3.1c. In contrast to earlier reports [51], our results reveal an easy-plane magnetic anisotropy in FGT. This behavior has also been observed in MBE-grown FGT films [135] and Fe-deficient crystals [124]. The hysteresis loops persist up to room temperature, although the magnetic moment decreases with increasing temperature. Enlarged M(H) loops at 300 K are shown in Figure 3.1d. Both in-plane and out-of-plane measurements exhibit finite remanence and coercivity, suggesting possible canted magnetization at room temperature. This observation is consistent with earlier findings by May et al., who reported very weak anisotropy at elevated temperatures [51, 124].

3.1.2 Co-doped Fe_5GeTe_2

In Co-doped Fe_5GeTe_2, the magnetocrystalline anisotropy and Curie temperature (T_C) are strongly dependent on Co doping [53, 136, 137]. As schematically illustrated in Figure 3.2a, up to doping concentrations of 20%, Co atoms prefer to substitute to the outermost Fe sublattices (Fe1 split sites), which are labeled FeU and FeD species (dark blue color) *(Paper II)*. This agrees with other studies showing that Fe split sites are most prone to defects [51, 138].

Co concentration and magnetic anisotropy energy (MAE) are found to have a direct correlation, where doping alters the magnetocrystalline anisotropy from a weak out-of-plane or canted magnetization to a stronger easy-plane magnetization. In the pristine FGT, the outermost Fe has the largest contribution to the out-of-plane MAE. The Fe atoms towards the center of the monolayer have a decreased out-of-plane magnetic anisotropy (Fe5, Fe2), while Fe4, and Fe3 exhibit large in-plane MAE. Hence, the change in the magnetic anisotropy with Co doping

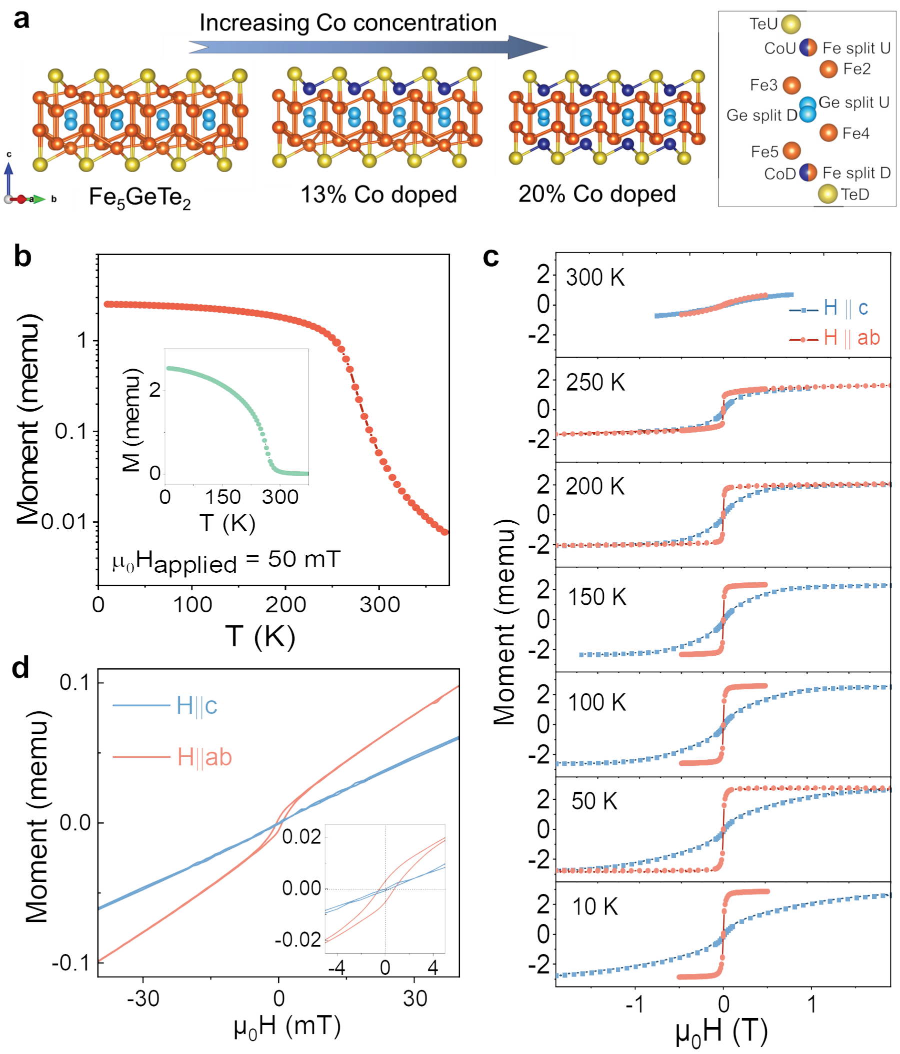

Figure 3.2: SQUID measurements of Co$_{0.15}$Fe$_{0.85}$)$_5$GeTe$_2$. a. Schematic illustration of Co-doped Fe$_5$GeTe$_2$ crystal structure with increasing Co concentration. Co, Fe, Te, and Ge atoms are represented by dark blue, orange, yellow, and light blue spheres, respectively. The right panel provides a detailed view of the atomic labels and their spatial arrangement along the crystallographic c-axis, highlighting the substitutional of Co into the Fe sublattice, with Fe(1) site as the most preferential doping site. **b.** The magnetic moment (M) of bulk CFGT as a function of temperature in logarithmic scale under an applied in-plane magnetic field of 50 mT. The inset displays the corresponding M(T) dependence on a linear scale. **c.** Temperature-dependent magnetic hysteresis loops of the CFGT crystal from 10 K to 300 K further demonstrate the persistence of strong in-plane ferromagnetic ordering throughout the measured range. **d.** Enlarged magnetic hysteresis loops measured at 300 K reveal a clear distinction between in-plane (orange) and out-of-plane (light blue) magnetic responses, indicating anisotropic magnetic behavior sustained up to room temperature.

can be understood from the substitution of the large out-of-plane magnetization in FeU and FeD with in-plane magnetization in CoU and CoD, and consequently the reduced MAE in Fe5 and Fe2, establishing a strong easy-plane anisotropy in Co-doped FGT for Co concentration up to 20% [83]. This easy-plane anisotropy together with enhanced T_C and magnetic anisotropy have been reported for Co-doping below 30% . Higher doping concentrations (>30%) lead to a change in lattice structure from rhombohedral to primitive cell as well as a change in magnetic ground state from ferromagnetic easy-plane anisotropy to antiferromagnetic perpendicular magnetic anisotropy [53, 136, 137].

To probe the magnetic properties of Co-doped FGT, we focus on $(Co_{0.15}Fe_{0.85})_5$ $GeTe_2$, which is still ferromagnetic but with higher T_C. The temperature-dependent magnetic moment of a bulk $Co_{0.15}Fe_{0.85})_5GeTe_2$ crystal was measured with a SQUID magnetometer. The M(T) curve in Figure 3.2b shows that a higher T_C has been achieved evidenced by a finite magnetic moment above 300 K. In contrast to FGT, the M(T) curve only show one transition-the paramagnetic to ferromagnetic transition at 310 K. The spin glassy phase transition and magnetostructural transition at lower temperatures are not observed in CFGT. This is a consequence of the preferential occupancy of Co-dopants to the defect-prone outermost Fe sites, which contributes to the low-temperature transitions.

Isothermal magnetic hysteresis loops M(H) measured from 10 K to 300 K for both in-plane (H||ab) and out-of-plane (H||c) orientations of the magnetic field (Figure 3.2c) show that strong easy-plane anisotropy is maintained up to room temperature. The magnified hysteresis loop at 300 K (Figure 3.2d) shows a clear remanence in the in-plane direction (H||ab), while the magnetic hysteresis almost vanishes for the out-of-plane orientation (H||c).

3.1.3 Ni-doped Fe_5GeTe_2

Similarly, for Ni-doped Fe_5GeTe_2, T_C and magnetic anisotropy are greatly affected by Ni dopants which preferentially substitute to the outermost Fe split site (FeU and FeD). However, in contrast to CFGT, the ferromagnetic ground with easy plane magnetic anisotropy is maintained with an increase in T_C and saturation magnetization peaking at 40% of Ni doping (with a record T_C close to 500 K) [52, 117]. After which, further increase of Ni concentration results to the dilution of magnetic moments leading to the decrease in T_C and magnetization saturation until the onset of paramagnetic state with doping concentrations beyond 86% [52]. Structural transformations have been observed in Ni-doped Fe_5GeTe_2, marked by a transition from ABC rhombohedral stacking to AA trigonal stacking. At higher doping levels, phase segregation emerges, giving rise to distinct Fe-rich and Ni-rich regions. Additionaly, itinerant ferromagnetism in the system is enhanced due to electron doping, as Ni atoms donate additional carriers to the system [52]. These findings underscore the strong interplay between magnetic behavior, electronic structure, and lattice configuration [139].

SQUID measurements for $(Ni_{0.40}Fe_{0.60})_5GeTe_2$ are shown in Figure 3.3. Due to the high T_C, the paramagnetic to ferromagnetic transition was not observed on the range of measurements performed. By fitting the M(T) data to $M(T) \approx (T_C - T)^\beta$, we obtain a T_C of 482 ± 2 K using a critical exponent of $\beta = 0.33$, which has been reported for AA stacked Fe_5GeTe_2 [140]. Similar to CFGT, the transitions at lower temperatures are also not observed for NFGT. M(H) curves in Figure 3.3b at different temperatures show strong easy-plane anisotropy persisting even beyond room temperature.

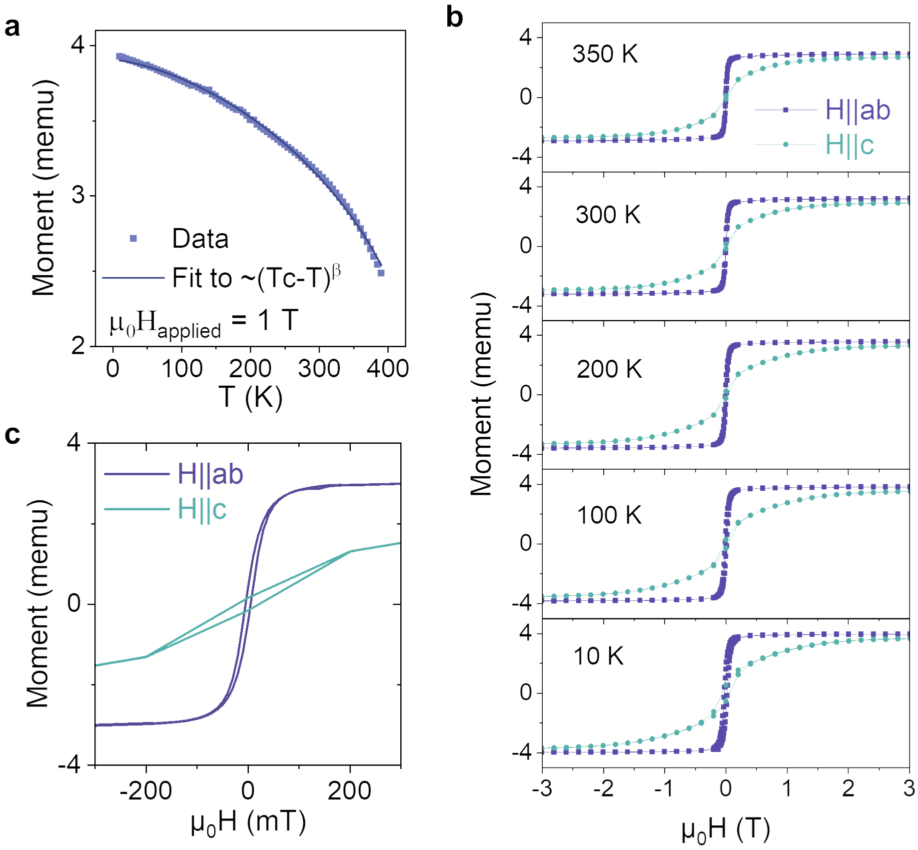

Figure 3.3: SQUID measurements of $(Ni_{0.40}Fe_{0.60})_5GeTe_2$ a. The magnetic moment (M) of bulk NFGT as a function of temperature under an applied magnetic field of 1 T from 2 K to 400 K. **b.** Isothermal magnetic hysteresis loops of the NFGT crystal from 10 K to 350 K showing beyond room temperature ferromagnetism with strong in-plane anisotropy. **c.** Magnified magnetic hysteresis loops measured at 300 K reveal a clear distinction between in-plane (purple) and out-of-plane (cyan) magnetic responses.

3.2 Ferromagnetic resonance in $\mathrm{Fe_5GeTe_2}$ and its doped variants

Broadband ferromagnetic resonance experiments over a wide range of frequencies were performed on bulk crystals of FGT, CFGT, and NFGT at room temperature using a Phase FMR system with a coplanar waveguide (CPW) for microwave field excitation (*Paper IV*). Microwave excitation fields h_{rf} with frequencies in the range of $5-30$ GHz were applied along the ab-plane of the crystals, while the DC magnetic field was applied along the ab-plane and c-plane of the crystals to investigate both their in-plane and out-of-plane response. The bulk vdW ferromagnetic crystals have a planar geometry, with the exception of NFGT (with a more granular structure), which allows us to orient the magnetic field parallel and perpendicular to the plane.

3.2.1 Probing magnetic resonance under an in-plane magnetic field

The sample position on the coplanar waveguide (CPW), applied in-plane magnetic field H, microwave excitation field h_{rf}, and the effective magnetic field H_{eff}, are shown in the schematic illustration in Figure 3.4a. When the frequency of precession matches the frequency of the applied microwave excitation field, the ferromagnet absorbs maximal microwave power. The power derivative of the FMR absorption spectra for FGT, CFGT, and NFGT is shown in Figure 3.4b-d, together with the fits to the sum of the symmetric and antisymmetric Lorentzian derivatives as described below[141]:

$$\frac{dP}{dH}(H) = \frac{-8C_1\Delta H(H-H_R)}{[\Delta H^2+4(H-H_R)^2]^2} + \frac{2C_2[\Delta H^2-4(H-H_R)^2]}{[\Delta H^2+4(H-H_R)^2]^2} \tag{3.1}$$

where H, ΔH, H_R, C_1, and C_2 correspond to the applied magnetic field, the full width at half maximum (FWHM) of FMR absorption, resonance field, and the symmetric and anti-symmetric fitting parameters of the Lorentzian derivatives, respectively.

Achieving resonance for FGT, CFGT, and NFGT confirms their ferromagnetic behavior at room temperature. From the FMR absorption spectra, it is observed that resonance conditions are obtained for FGT and CFGT for a broader range of frequencies up to 30 GHz within the applied field range of 1 T. NFGT, on the other hand, shows resonance conditions for the measured frequency range of $5-18$ GHz.

By fitting the FMR absorption spectra at each frequency to Equation 3.1, we obtain the frequency (f) dependence of the resonant field (H_R), as shown in Figure 3.4a, together with fits to Kittel's equation [142]:

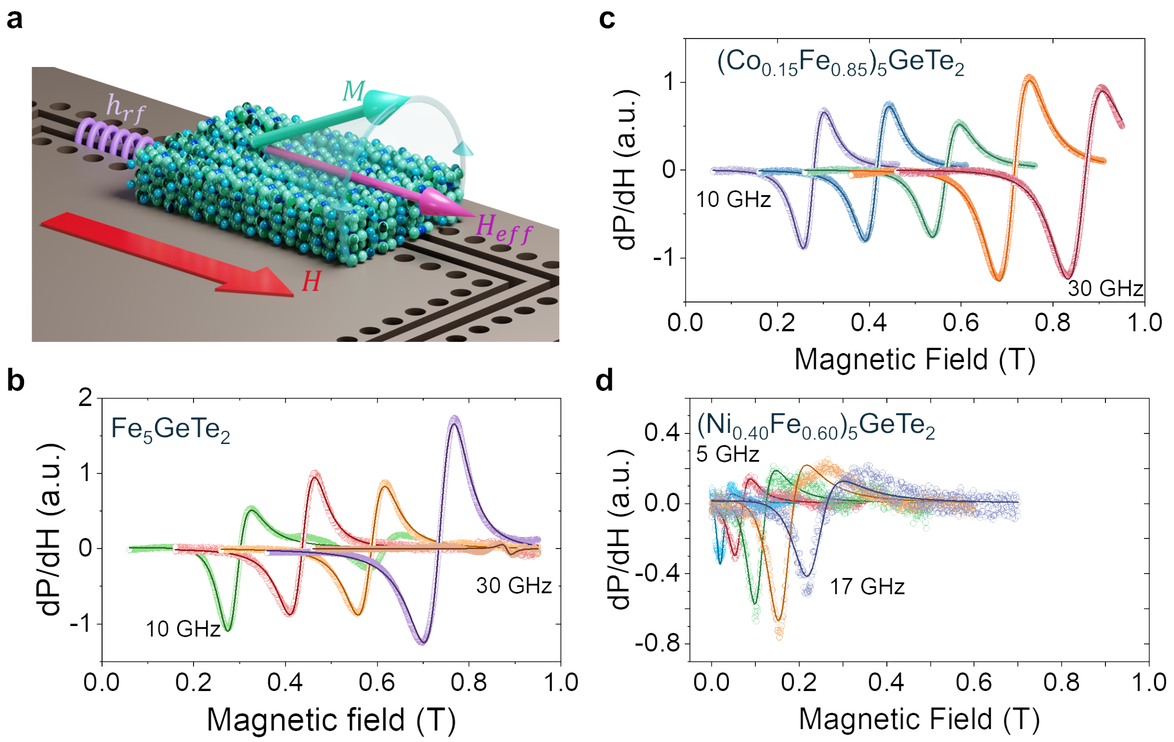

Figure 3.4: In-plane ferromagnetic resonance (IPFMR) spectra for FGT, CFGT, and NFGT a. Schematic diagram of ferromagnetic resonance (FMR) measurements on a vdW bulk ferromagnet on a coplanar waveguide (CPW) where a microwave field (h_{rf}) in the range of 5-30 GHz and an in-plane magnetic field up (H) to 1 T is applied. Representative data of ferromagnetic resonance response of **b.** FGT, **c.** CFGT, and **d.** NFGT corresponding to the power derivative of the FMR absorption spectra with an in-plane field at room temperature. The hollow symbols are the raw data, and the solid lines are the fits to Eq. 3.1

$$f_{(H||ab)} = \frac{\gamma\mu_0}{2\pi}\sqrt{(H_R - H_k)(H_R - H_k + M_{\text{eff}})} \tag{3.2}$$

where $\gamma = \frac{g\mu_B}{\hbar}$ is the gyromagnetic ratio with g as the Landé g-factor and μ_B is the Bohr magneton, H_k is the in-plane magnetic anisotropy field, M_{eff} is the effective magnetization of the sample, and μ_0 is the permeability of vacuum. γ, H_k, and M_{eff} are allowed to be free fitting parameters. The extracted values of g, $\mu_0 H_k$, and $\mu_0 M_{eff}$ for FGT, CFGT, and NFGT are summarized in Table 3.1.

Generally, the total magnetic moment M of a material is determined from the contribution of both spin (S) and orbital angular momentum (L) which can then be represented by an effective spin (S') and where the g-tensor takes into account the different g-values in each crystallographic direction [143]:

$$M = -\mu_B(L + 2S) \rightarrow g\mu_B S' \tag{3.3}$$

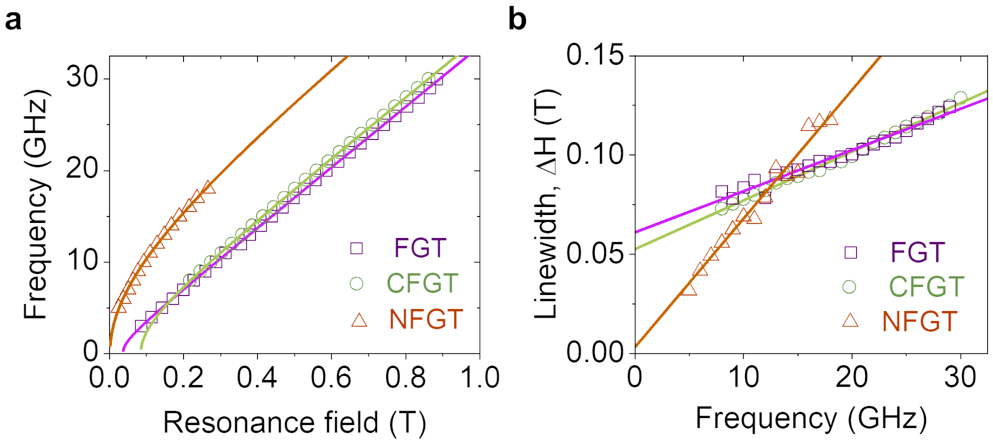

Figure 3.5: Resonance and linewidth analysis for FGT, CFGT, and NFGT under an in-plane magnetic field at room temperature. a. Frequency dependence of the resonant field for FGT (purple), CFGT (green), and NFGT (orange). The hollow symbols correspond to the experimental data, and the line is the fit to Kittel's equation (Eq. 2.), where anisotropy field ($\mu_0 H_k$), gyromagnetic ratio ($\gamma/2\pi$), and effective magnetization ($\mu_0 M_{eff}$) were extracted. **b.** Linewidth analysis for FGT (purple), CFGT (green), and NFGT (orange). Hollow symbols correspond to the experimental data while the solid line is the fit to Eq. 3, where the linewidth broadening (ΔH_0) and damping constant (α) were extracted.

For which, $g = 2.0023$ corresponds to a pure electron spin contribution to the magnetic moment. For H||ab, FGT, CFGT and NFGT have Landé g-factors that are greater than 2, indicating possible orbital contribution or spin-orbit interaction. Large Berry curvature has already been reported for Fe_3GeTe_2[144] and Fe_3GaTe_2 [145], while self-induced spin-orbit torque was observed in Co-doped Fe_5GeTe_2 [92]. To evaluate the orbital contribution to the g-factor we calculate for the ratio of orbital (μ_L) to spin (μ_S) contribution [146] $\mu_L/\mu_S = (g-2)/2$, which comes out to be 0.18 for FGT, 0.165 for CFGT, and 0.15 for NFGT.

Interestingly, by doping FGT with Co and Ni, the effective magnetization is increased significantly, especially for NFGT with $\mu_o M_{eff,NFGT} = 0.960$T. Among the three, NFGT has the highest effective magnetization and T_C. These enhancements were attributed to a more pronounced lattice reorientation with Ni-doping compared to Co-doping [52].

In addition, by analyzing the frequency dependence of the linewidth, ΔH, we can extract the effective Gilbert damping constant α, and the inhomogeneous broadening, ΔH_0, of the FMR spectra by fitting the ΔH versus f shown in Figure 3.5b to [147–149]:

$$\Delta H = \Delta H_0 + \frac{4\pi\alpha f}{\gamma\mu_0} \tag{3.4}$$

Equation 3.4 is used to fit the experimental values by having both ΔH_0 and α

Material	***g*-factor**	**$\mu_0 M_{\text{eff}}$ (T)**	**$\mu_0 H_k$ (T)**	**α**	**ΔH_0 (T)**
Fe_5GeTe_2 (FGT)	2.36±0.01	0.11±0.02	0.08±0.01	0.041±0.002	0.061±0.002
$(Co_{0.15}Fe_{0.85})_5GeTe_2$ (CFGT)	2.33±0.01	0.31±0.02	0.23±0.01	0.040±0.001	0.053±0.001
$(Ni_{0.40}Fe_{0.60})_5GeTe_2$ (NFGT)	2.30±0.04	0.96±0.03	0.95±0.06	0.104±0.005	0.003±0.002

Table 3.1: Dynamic magnetic parameters extracted from broadband IPFMR measurements.

as adjustable fitting parameters, achieving a good fit to the experimental data. The extracted values of ΔH_0 and α are summarized in Table 3.1. Resonance peak linewidths in FMR give us information on the relaxation times and magnetic uniformity of the sample. A broader linewidth indicates the presence of inhomogeneities in the sample. On the other hand, a narrow linewidth is expected from a highly uniform sample. FGT and CFGT have a Gilbert damping constant in the range of 0.04, comparable to earlier reports on FGT [150], while NFGT has a higher damping constant of 0.104. This makes FGT and CFGT attractive for high-frequency magnetization dynamics applications, while NFGT is more suitable for highly stable magnetic applications.

Another important parameter is the inhomogeneous linewidth broadening, ΔH_0, which behaves independent of the frequency. ΔH_0 may be caused by defects in the material, grain boundaries, domain structures, and other scattering processes [33]. NFGT shows minimal linewidth broadening of 0.003 T, a magnitude lower than FGT and CFGT with 0.061 T and 0.053 T, respectively. This indicates better magnetic uniformity in NFGT compared to FGT and CFGT. Two-magnon scattering (TMS) is another factor that can lead to linewidth broadening and may influence the effective damping constant obtained from our measurements [151]. Although TMS is known to exhibit a nonlinear dependence on frequency, our data show a linear relationship between linewidth and frequency across a broad frequency range. This suggests that the contribution of TMS, if present, is likely small but cannot be completely ruled out.

3.2.2 Probing magnetic resonance under an out-of-plane magnetic field

Next, we measured FMR with an applied out-of-plane magnetic field as schematically shown in Figure 3.6a. Figure 3.6b and c show the representative resonance spectra for FGT and CFGT, respectively. For FGT, the resonance spectra show sharp resonance signatures almost like the in-plane spectra. As earlier studies reported canted magnetism for FGT [81, 104], this could explain the distinct resonance curves obtained for both in-plane and out-of-plane applied magnetic fields. On the other hand, CFGT shows broader and a more dilute resonance spectra

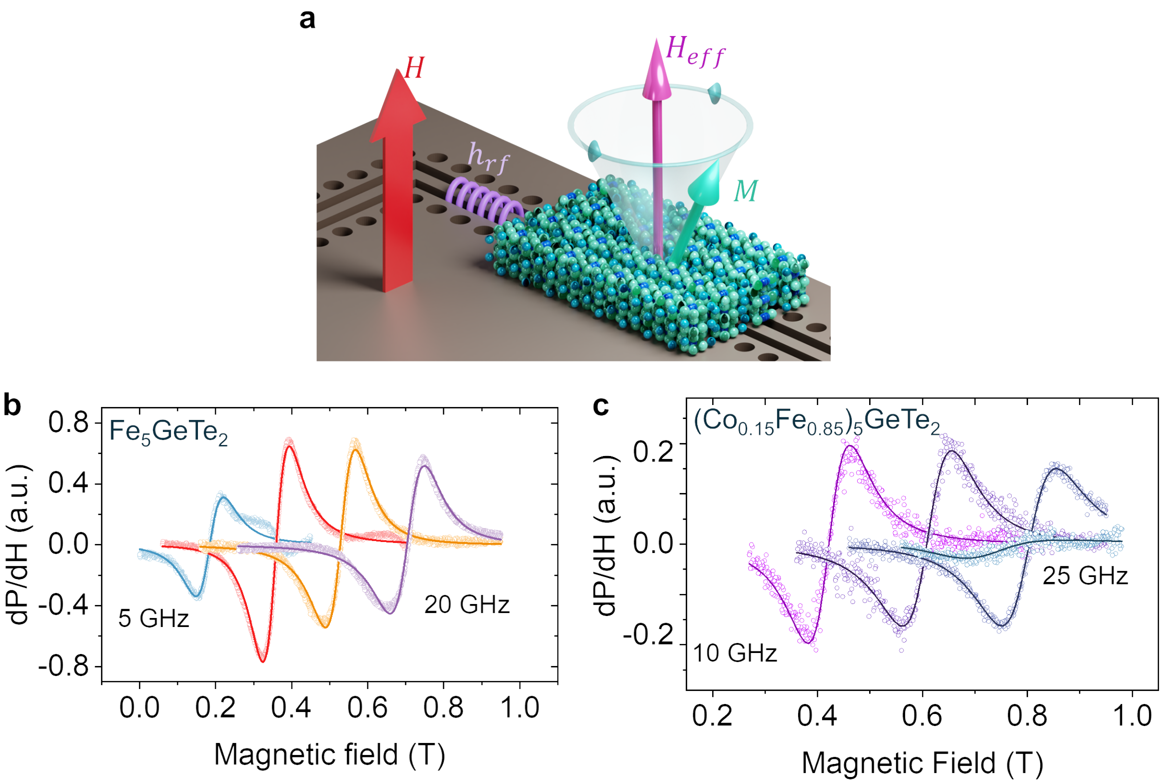

Figure 3.6: Out-of-plane ferromagnetic resonance (OPFMR) of FGT and CFGT a. Schematic diagram of ferromagnetic resonance (FMR) measurements on a vdW bulk ferromagnet on a coplanar waveguide (CPW) where a microwave field (h_{RF}) in the range of $5 - 30$ GHz and an out-of-plane magnetic field up (H) to 1 T is applied. **b.** Representative data for the ferromagnetic resonance response of FGT under an out-of-plane magnetic field showing resonance condition from $5 - 20$ GHz. **c.** Representative data for the ferromagnetic resonance response of CFGT with an out-of-plane field at a frequency range of $10 - 20$ GHz. The hollow symbols are the raw data, and the solid lines are the fits to Eq.3.1

under an out-of-plane field compared to the in-plane configuration. As CFGT has an easy-plane magnetic anisotropy, the weaker signals are expected in FMR signals with a small out-of-plane magnetic field of 1 T. For NFGT, with a strong easy-plane anisotropy, evident from the anisotropy field and effective magnetization we extracted, resonance conditions under an out-of-plane magnetic field cannot be obtained within a 1 T field range.

Similarly, the ferromagnetic resonance spectra at each frequency are fitted to Equation 3.1, and the obtained H_R versus f is shown in Figure 3.7a together with fits to the out-of-plane Kittel's equation [142]:

$$f_{H||c} = \frac{\gamma\mu_0}{2\pi}(H_R - M_{\text{eff}}) \tag{3.5}$$

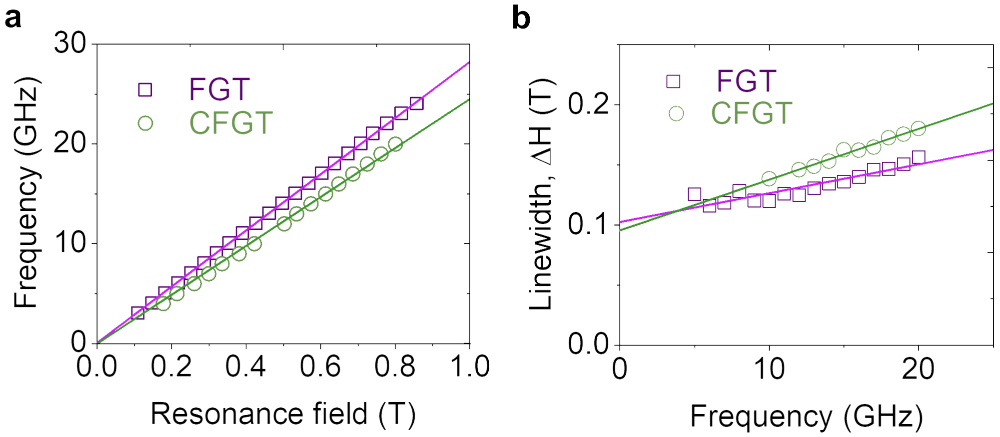

Figure 3.7: Resonance and linewidth analysis for FGT and CFGT under an out-of-plane magnetic field at room temperature. a. Frequency dependence of the resonant field for FGT (purple) and CFGT (green). The hollow symbols are the experimental data and the solid line is the fit to Kittel's equation (Eq. 4). **b.** Linewidth analysis for FGT (purple) and CFGT (green), where the linewidth broadening (ΔH_0) and damping constant (α) were extracted from the fitting to Eq. (3). The hollow symbols are the experimental data points.

Since the M_{eff} is sample dependent, we use the M_{eff} extracted in the in-plane FMR in Equation 3.2. The g values for FGT and CFGT under an out-of-plane field are summarized in Table 3.2. The frequency dependence of the linewidth was analyzed using Equation 3.4 with the extracted γ from the out-of-plane Kittel fitting, as shown in Figure 3.7b. The extracted values of ΔH_0 and α are also listed in Table 3.2.

Material	***g*-factor**	$\mu_0 M^*_{\text{eff}}$ **(T)**	α	ΔH_0 **(T)**
Fe_5GeTe_2 (FGT)	2.012 ±0.003	0.11	0.034 ±0.004	0.102 ±0.004
$(Co_{0.15}Fe_{0.85})_5GeTe_2$ (CFGT)	1.752 ±0.009	0.31	0.051 ±0.002	0.095 ±0.003

Table 3.2: Magnetic dynamic parameters extracted from broadband OPFMR measurements.

From the out-of-plane Kittel fitting we obtained a corresponding g-factor of 2.012 for FGT, and 1.752 for CFGT. Inhomogeneous linewidth broadening has increased for both FGT and CFGT at 0.1024 T and 0.0953 T, respectively, compared to the in-plane configuration. When measuring using out-of-plane magnetic field, the spins are aligned against the preferred easy axis, leading to enhanced spin fluctuations and inhomogeneous broadening. Although TMS contribution is suppressed, other effects such as surface inhomogeneities could also contribute to the linewidth broadening [43].

3.2.3 Anisotropic g-factor in Fe_5GeTe_2 and $(Co_{0.15}Fe_{0.85})_5GeTe_2$

Measurement of g-factor from FMR with the magnetic field applied in different directions could reveal orbital contributions to the total magnetic moment, which could be different for different crystallographic directions. Figure 3.8a and b show the frequency dependence of the resonance field for FGT and CFGT under an in-plane field (H||ab) and (H||c) out-of-plane field. We observe anisotropic g-factor for both FGT and CFGT as evident from the different slopes in the f versus H_R plots.

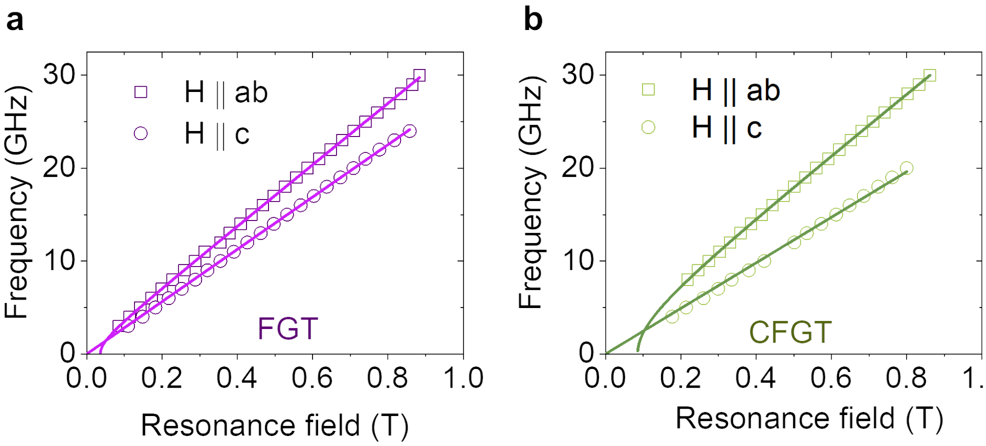

Figure 3.8: Anisotropic g-factor for FGT and CFGT. a. Comparison of the H_R vs f for FGT under an in-plane and out-of-plane field. **b.** H_R vs f for CFGT at different field orientations.

To maintain magnetism at reduced dimensions, like in vdW ferromagnets, uniaxial magnetic anisotropy is needed which could stem from crystal structure. This could reflect anisotropic behaviors. For FGT, the in-plane g-factor is 2.36 ($\mu_L/\mu_S = 0.18$) and the out-of-plane g-factor is 2.012 ($\mu_L/\mu_S = 0.006$) , while for CFGT it is 2.33 ($\mu_L/\mu_S = 0.165$) and 1.752 ($\mu_L/\mu_S = -0.124$), respectively. This drastic change in g-factor may be related to anisotropic spin-orbit coupling as orbital effect seems to be opposing spin in out-of-plane direction. The observed deviations of the g-factors from the free-electron value suggest a substantial orbital contribution to the total magnetic moment, with pronounced anisotropy in FGT and CFGT. These results highlight the role of spin–orbit coupling and crystal symmetry in governing the magnetization dynamics of vdW ferromagnets.

In summary, we have investigated the magnetization dynamics of van der Waals ferromagnets FGT, CFGT, and NFGT at room temperature using broadband ferromagnetic resonance (FMR) spectroscopy. From these measurements, we extracted key dynamic parameters including the g-factor, effective magnetization, in-plane magnetic anisotropy field, and Gilbert damping constant. A comparison of damping constants and other parameters for several vdW ferromagnets are presented in Table 3.3.

Material	α	$\mu_0 M_{\text{eff}}$ **(T)**	$\mu_0 H_k$ **(T)**	**Technique**	**Temp.**	**Ref.**
$(Ni_{0.40}Fe_{0.60})_5GeTe_2$ (NFGT)	0.104 (IP)	0.96	0.95	B-FMR	300 K	This work
$(Co_{0.15}Fe_{0.85})_5GeTe_2$ (CFGT)	0.040 (IP) 0.051 (OP)	0.31	0.23	B-FMR	300 K	This work
Fe_5GeTe_2	0.041 (IP) 0.034 (OP)	0.11	0.08	B-FMR	300 K	This work
Fe_5GeTe_2	0.035 (OP)	–	–	B-FMR	300 K	[150]
Fe_5GeTe_2	0.0513 (IP)	0.054	–	B-FMR	300 K	[152]
$Fe_{4.8}Co_{0.2}GeTe_2$	0.0526 (IP)	0.050	–	B-FMR	300 K	[152]
Fe_3GaTe_2	0.075 (OP)	0.083	4.00	TR-MOKE	300 K	[153]
Fe_3GeTe_2	0.058 (OP)	–	–	ESR	185–210 K	[154]
$CrBr_3$	0.009 (OP)	∼0.15	∼0.2	FMR	30 K	[155]
$Cr_2Ge_2Te_6$ (10.5 nm flake)	0.006(OP)	–	0.125	TRFR	10 K	[156]
Permalloy (3 nm thin film)	0.013 (IP)	–	–	FMR	300 K	[157]

Table 3.3: Summary of magnetic damping constant (α), effective magnetization ($\mu_0 M_{\text{eff}}$), anisotropy field ($\mu_0 H_k$) for different van der Waals magnets. Measurements were performed on bulk crystals unless otherwise specified. B-FMR: broadband ferromagnetic resonance spectroscopy; ESR: electron spin resonance; TR-MOKE: time-resolved magneto-optical Kerr effect; TRFR: time-resolved Faraday rotation.

4 Van der Waals ferromagnet/graphene spin valve heterostructures

In this chapter, we continue to probe the vdW ferromagnets Fe_5GeTe_2 (FGT) and $(Co_{0.15}Fe_{0.85})_5GeTe_2$ (CFGT) by integrating them into spintronic devices. We demonstrate the robust room temperature operation of lateral spin valve (SPV) devices using FGT (*Paper I*) and CFGT (*Paper II*) in heterostructures with graphene to evaluate their properties as spin sources, as illustrated in Figure 4.1. We performed room temperature spin transport measurements in nonlocal spin valve configuration and observed characteristic spin valve switching for both FGT/graphene and CFGT/graphene devices. The room temperature spintronic properties of FGT and CFGT are measured at the interface with graphene, characterized by a negative spin polarization. Hanle spin precession measurements provide additional insights by probing the spin dynamics at the vdW magnet/graphene interface, revealing canted magnetic moments in FGT and in-plane magnetic anisotropy in CFGT. These findings open opportunities for vdW interface design and applications of vdW-magnet-based spintronic devices at ambient temperatures.

4.1 Spin valve devices with Fe_5GeTe_2 and $(Co_{0.15}Fe_{0.85})_5GeTe_2$

In vdW ferromagnet/graphene spin valves, exfoliated FGT and CFGT flakes are used as spin injector or detector on a graphene spin transport channel (chemical vapor deposited CVD [158] or exfoliated graphene), with additional ferromagnetic cobalt (Co) contacts, and reference nonmagnetic gold (Au) contacts. An optical micrograph of a representative SPV device is shown in Figure 4.1b. The well-studied spin properties of Co contacts help to isolate and characterize the spin properties of the vdW ferromagnets. The nonlocal (NL) spin valve and Hanle spin precession measurements are sensitive to the vdW ferromagnet/graphene interface and should allow probing of the different spin polarization components (S_x, S_y, S_z). The spin valve measurements with the magnetic field (B_y) sweep along the y-axis can provide information about the in-plane spin polarization (S_y) along

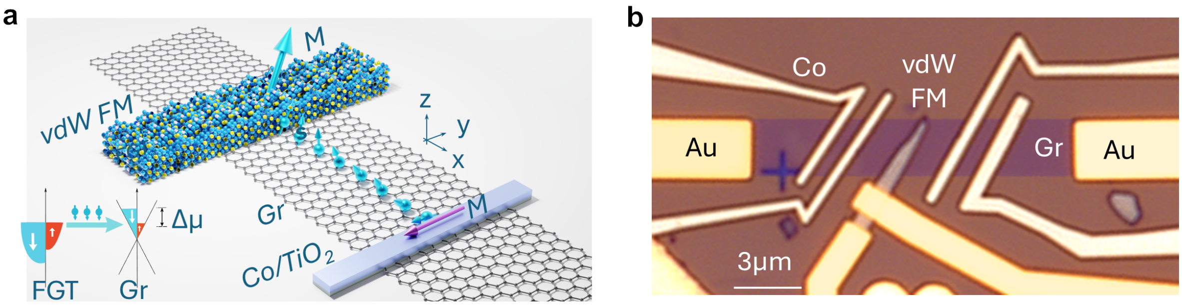

Figure 4.1: Room temperature graphene spin valves with vdW ferromagnets a. Schematic illustration of vdW ferromagnet/graphene spin valves (SPV) showing spin injection/detection in graphene with Co/TiO_2 as a reference ferromagnetic contact. **b.** Optical micrograph of a representative SPV device showing the vdW ferromagnet, Co electrode, graphene channel (recolored for visibility), and Au reference electrodes. The scale bar is 3 μm.

the y-axis, whereas the Hanle spin precession measurements with $B_{x(z)}$ along the x(z)-axis is a reliable approach to extract the (initial) spin polarization S_y and $S_{z(x)}$ and spin dynamic properties.

4.2 Graphene spin valves with Fe_5GeTe_2

4.2.1 Spin injection and detection in Fe_5GeTe_2

Figure 4.2a show the nonlocal SPV signal for FGT injection and detection, with the inset showing the corresponding nonlocal measurement set-up. In the FGT injection case, a current bias I_{dc} is applied between the FGT and Au contact. Spin accumulation occurs at the FGT/graphene interface, which then diffuses towards the Co detector. The nonlocal voltage is measured in the Co detector with respect to another Au contact, which relates to the magnitude of spin current detected by the Co contact. In the case of FGT detection, I_{dc} is applied between Co and Au and the nonlocal voltage is measured between FGT and another Au contact. The nonlocal geometry allows the segregation of the charge current pathway from that of the spin current. By sweeping a magnetic field along the long axis of both FGT and Co, in this case along the y-axis, the relative orientation of the magnetic moments of FGT and Co is tuned depending on their coercive fields (H_C), leading to a low resistance state (parallel) and to a high resistance state (antiparallel). By separately characterizing a reference Co (injector)-Co(detector) spin valve the switching fields (H_C) for the Fe_5GeTe_2 and Co contacts can be confirmed. In this case, the sharp switch at 5 mT corresponds to FGT and the switch at 27 mT corresponds to the Co contact. The observation of robust spin valve signals with sharp switching demonstrates the presence of an in-plane spin component S_y at the Fe$_5$GeTe$_2$/graphene interface at room temperature.

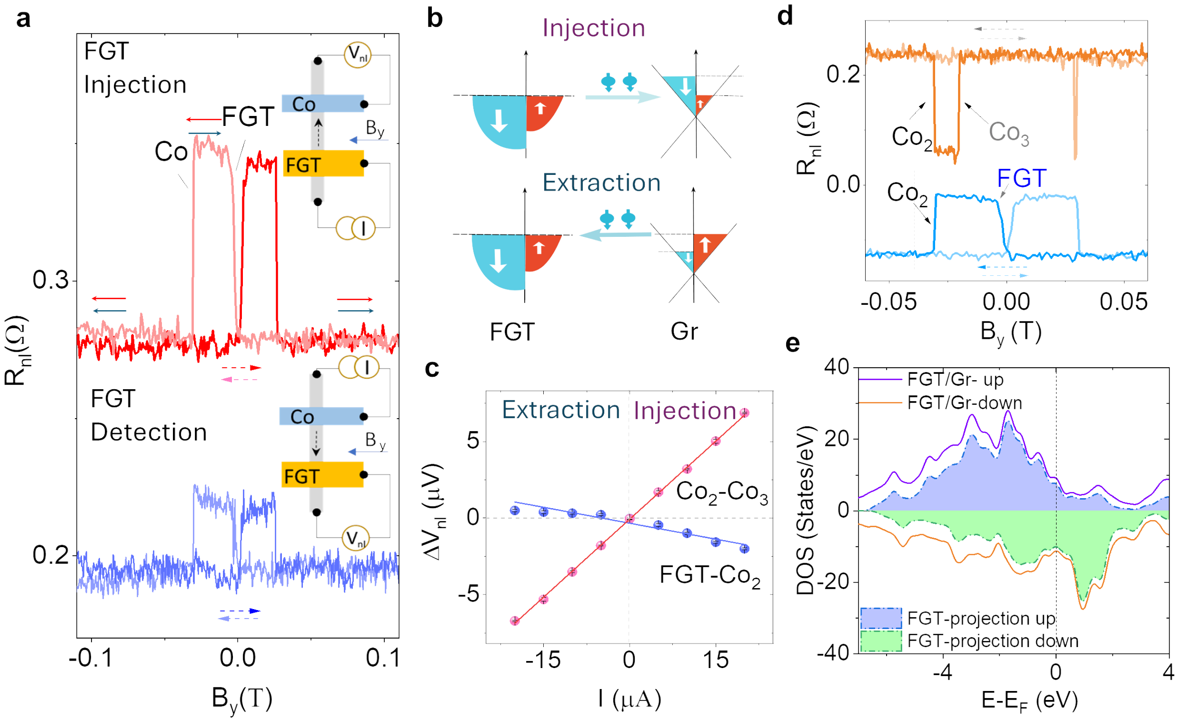

Figure 4.2: Spin injection and detection by Fe$_5$GeTe$_2$ a. The measured nonlocal (NL) spin valve signal $R_{nl} = V_{nl}/I_{dc}$ for spin injection from FGT with parallel (P) and antiparallel (AP) alignment of FGT and Co electrodes (red and blue arrows) on CVD graphene channel with an applied bias current I_{dc} across the FGT/Gr junction and NL voltage V$_{nl}$ measured by the Co detector, as shown in the measurement geometry in the inset. The reference Au/Ti contacts on FGT and graphene are represented by the black dots. The bottom panel shows the data for FGT as the detector and Co as an injector (schematic in the inset). The red (blue) dashed arrows show the magnetic field sweep directions. The switching fields for FGT and Co electrodes in the spin-valve measurement are indicated. The measurements were performed in Device 1 at room temperature. **b.** Schematics for the spin injection and extraction process at FGT/Gr interface, showing the accumulation of "down" and "up" spins in the graphene channel, respectively. **c.** Bias dependence of the FGT-Co$_2$ and Co$_2$-Co$_3$ spin-valve signal magnitude in the spin injection and extraction regime and the linear fittings, respectively. Co$_2$ and Co$_3$ are the reference Co electrodes. The error bars are calculated from the standard deviation of the measured data. d. Comparison of the measured spin valve signals of FGT-Co$_2$ and Co$_2$-Co$_3$ spin devices. The signals are shifted along the y-axis for clarity. **e.** Calculated spin-polarized total DOS for Fe$_5$GeTe$_2$/graphene heterostructure (solid lines) and projected onto Fe$_5$GeTe$_2$ (color-shaded area).

To examine the sign of the spin polarization of the Fe_5GeTe_2/graphene interface, results from current bias dependence measurements of FGT-Co spin valve were compared to results obtained for the standard Co-Co spin valve (Figure 4.2c). Reversing the bias current polarity ($+I_{dc}/-I_{dc}$) results in the spin accumulation with opposite spin polarization in graphene due to spin injection and extraction at the Fe_5GeTe_2/graphene interface, as illustrated in Figure 4.2b. In the spin injection case, the majority spin population in FGT will be accumulated in graphene while in the spin extraction case, the matching spin majority population in FGT will be extracted from the graphene channel leaving an accumulated opposite spin population in graphene. This explains the spin signal inversion with the sign inversion of the current bias. Moreover, the magnitude of the spin valve signal scales linearly with the applied bias current for Fe_5GeTe_2 and Co contacts. More importantly, we notice that the sign of the spin signal for the FGT-Co spin valve is opposite compared to that of the standard Co-Co spin valve, which implies negative or opposite spin polarization of the Fe_5GeTe_2/graphene interface compared to Co/TiO_2/graphene. Such a negative spin polarization is found to be robust and could be reproducibly observed in all devices. These observations agree with the density of states (DOS) obtained from DFT calculations (Figure 4.2e), where Fe_5GeTe_2 shows a negative spin polarization at the Fermi energy (E_F) with the DOS of the “spin-down” channel being larger than that of the “ spin-up” channel at the Fe_5GeTe_2/graphene interface.

To figure out the anisotropic characteristic of the Fe_5GeTe_2/graphene interface, an angle-dependent in-plane spin valve measurement was performed from $+90°$ to $-90°$ in the xy-plane as shown in Figure 4.3a-c. We observe that the switching field of the Co detector increases with the magnetic field rotation angle Φ, consistent with the strong uniaxial magnetic anisotropy of Co in a narrow stripe geometry. The measured spin valve signal is the result of the projection of the FGT spin polarization on the Co magnetic moment (M_{Co}). Note that, M_{Co} remains along the y-axis in the small B field range (±0.1 T). The saturation field of FGT is minimum at $\Phi = 0$, with a coercive field $H_C \approx 5$ mT, which is much smaller compared to that of Co. By extracting the antisymmetric precession and stage-like components from the in-plane results, we plot the angle dependence of the spin polarization S_z and S_y (Figure 4.3d and e). The measurements show that the in-plane magnetic moment of Fe_5GeTe_2 (and the corresponding spin polarization $S_{y(x)}$) can be easily rotated in the xy-plane by a small magnetic field; however, it has a robust out-of-plane spin polarization S_z. Similar results have been observed in the FGT detector configuration and in an additional device.

It should be noted that the spin valve data reflects the interfacial properties of the Fe_5GeTe_2/graphene and does not exactly match the bulk properties of Fe_5GeTe_2. This is due to the weak interlayer magnetic interaction in FGT [125, 132], resulting to only a few layers of Fe_5GeTe_2 at the interface with graphene which contribute to the spin valve signals. Moreover, the Fe_5GeTe_2/graphene interface area in different devices has a size of $\approx 1 - 3\mu\text{m}^2$, comparable to the expected Fe_5GeTe_2 magnetic domain size,[130, 131] which can explain the non-zero remanence at the injection/detection areas.

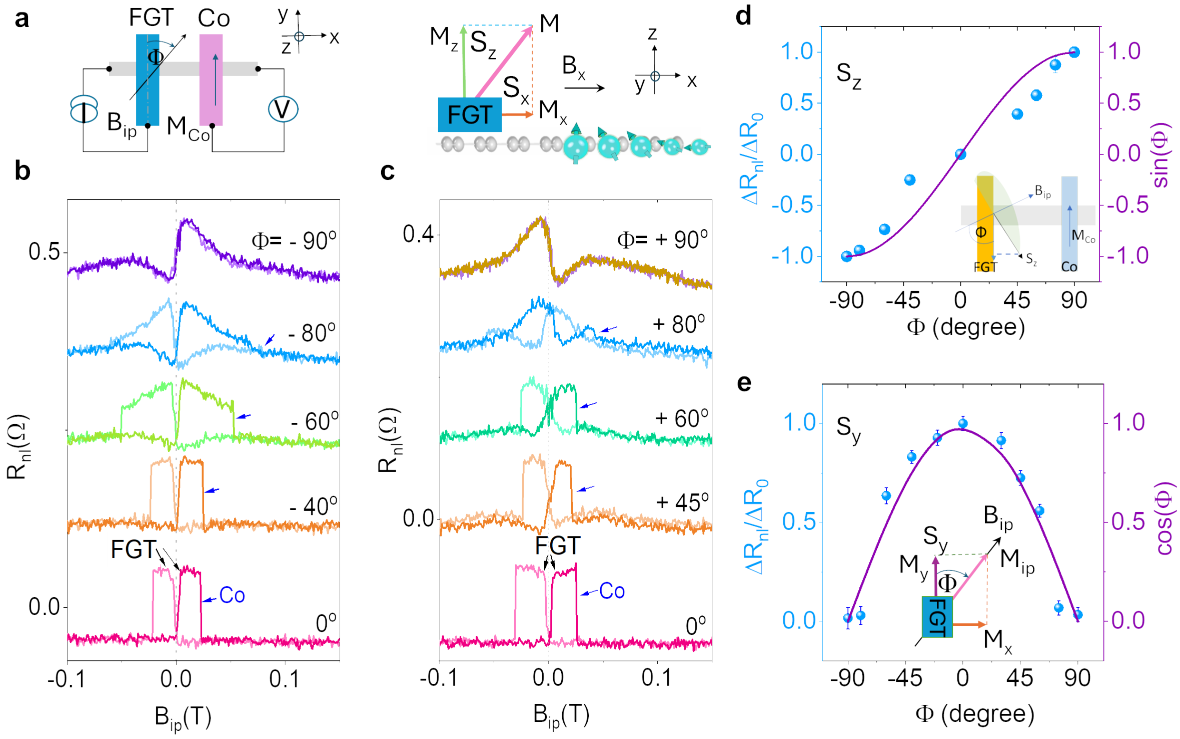

Figure 4.3: Angle dependence and spin precession in Fe_5GeTe_2/graphene heterostructure at room temperature. a. Left: Schematic top view of the spin valve device with in-plane B_{ip} magnetic field sweep in the xy-plane with an angle Φ relative to the y-axis. Right: Schematic side view of the device for magnetic moment configuration in FGT with an external B_x field. M is the magnetic moment with components M_x (M_z) along the x(z)-axis. S_x and S_z are the corresponding injected spin orientations. **b.** and **c.** In-plane angle dependence of the spin valve signal with angle $\Phi = 0$ to $-90°$ and 0 to $+90°$, respectively. The switching of injector FGT and detector Co electrodes in the spin valve signal are shown by the black and blue arrows, respectively. A linear y-axis shift is added to the signals for clarity, and a small hysteresis of ≈ 3.5 mT from the magnet is corrected using control experiments of reference Co-Co Hanle measurements. **d.** and **e.** Normalized spin valve signal components $S_{z(y)}$ and comparison with the sine (cosine) function with the in-plane B_{ip} rotation angle Φ. The error bars were calculated from the background noise of the signal. The insets are the top view of the schematic for the in-plane magnetic moment M_{ip} projection on the axes, where $S_{z(y)}$ are injected spins from magnetic moments $M_{z(y)}$ of FGT. The measurements were performed in Device 1 at room temperature.

4.2.2 Canted magnetism in Fe_5GeTe_2/graphene

To probe different spin polarization orientations at the Fe_5GeTe_2/graphene interface, we performed spin precession experiments in both the x-axis Hanle (xHanle) and the z-axis Hanle (zHanle) measurement geometries [159]. Figure 4.4a schematically shows the expected xHanle lineshape for different spin components (S_x, S_y, S_z) injected from Fe_5GeTe_2 with different magnetic moments (M_x, M_y, M_z). The injected out-of-plane spins S_z should result in an antisymmetric xHanle curve, whereas the spins along S_y should generate a symmetric xHanle signal. However, the spins along the S_x direction should not precess, resulting in the absence of a signal due to a collinear relationship with B_x. A sine-shaped xHanle signal is observed in the FGT-Co device (Figure 4.4b), indicating a possible out-of-plane spin S_z injection from the Fe_5GeTe_2/graphene interface due to the perpendicular magnetic anisotropy (PMA) of Fe_5GeTe_2 in remanence [160, 161]. The magnetic-moment-dependent xHanle signal shows a sign change with the parallel (P) and antiparallel (AP) states, also offering us a method to eliminate the non-spin precession related background.

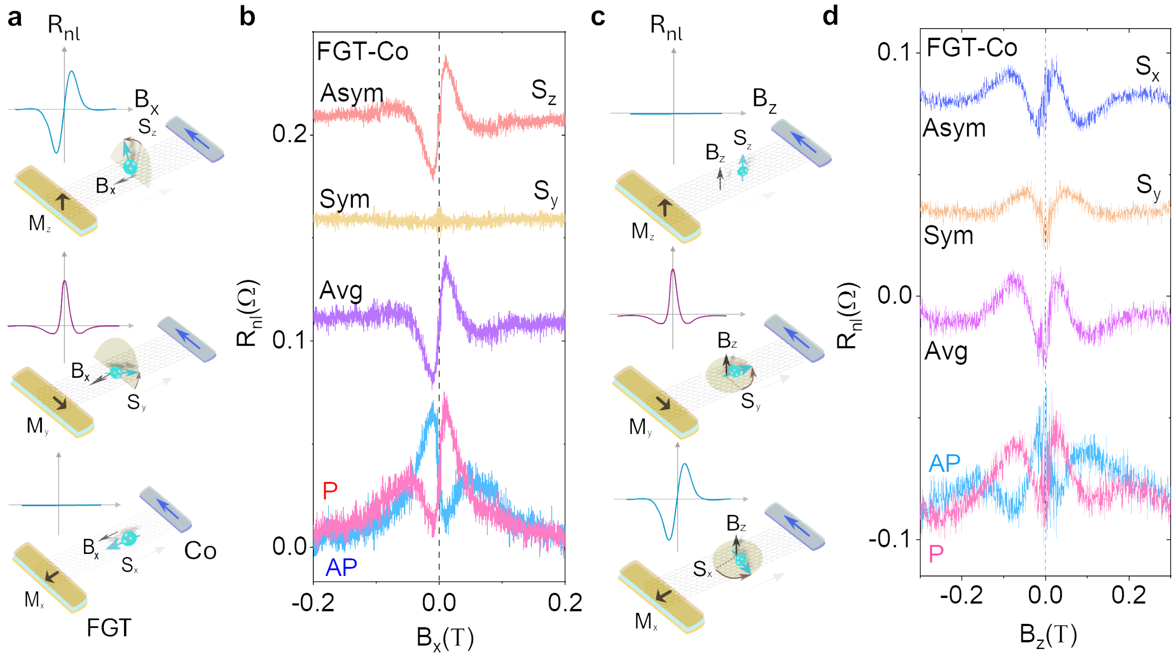

Figure 4.4: Hanle spin precession in Fe_5GeTe_2/graphene heterostructure at room temperature. a. and **c.** Schematics of xHanle and zHanle measurement geometries with B_x and B_z field sweeps respectively, and the expected lineshape of the spin precession signal for all the possible FGT magnetization scenarios (M_x, M_y, and M_z). **b.** and **d.** Measured xHanle and zHanle signals in the FGT-Co spin valve with different magnetic configurations (P/AP) of the electrodes. The averaged (Avg) Hanle signal and extracted symmetric (Sym) and antisymmetric (Asym) components are presented with a shift on the y-axis for clarity.

The difference in resistance between P and AP states $R_{avg} = [R_{nl(P)} - R_{nl(AP)}]/2$ was averaged (avg) and then decomposed into symmetric (sym) and antisymmetric (asym) components with $R_{asym} = [R_{avg}(B) + R_{avg}(-B)]/2$; $R_{sym} = [R_{avg}(B) - R_{avg}(-B)]/2$, corresponding to the spin components S_y and S_z, respectively. Notably, there is no symmetric Hanle component, suggesting no remanent S_y component when a B_x is applied, which is due to the soft magnetic property of the Fe_5GeTe_2 magnetization. This is consistent with a small H_C and a narrow minor loop observed for the Fe_5GeTe_2 in the spin-valve measurements. These xHanle measurements suggest an out-of-plane magnetic anisotropy at the Fe_5GeTe_2/graphene interface with spin polarization S_z in remanence.

Similarly, the in-plane spin polarizations $S_{y(x)}$ in the FGT-Co device were evaluated based on the symmetric and antisymmetric characteristics of the measured zHanle curves (Figure 4.4c). In contrast, the S_z spin polarization should not result in a signal, as it is collinear with B_z. The measured zHanle signal of the FGT-Co spin valve device (Figure 4.4d) suggests the injection of both spins, S_x and S_y, from the Fe_5GeTe_2/graphene interface. Measurements with the different magnetization directions of the magnetic moments (P/AP) result in the sign reversal of the Hanle curves, which are then averaged (R_{avg}) and decomposed into symmetric (Sym) and antisymmetric (Asym) components, corresponding to the spin components S_y and S_x, respectively. However, the magnitude of the S_x and S_y signals are much smaller than the measured S_z signal, confirming stronger out-of-plane magnetic moment in remanence at the Fe_5GeTe_2/graphene interface. The presence of canted magnetism can offer such multidirectional spin polarization in Fe_5GeTe_2.

4.2.3 Spin polarization at the Fe_5GeTe_2/graphene interface

Finally, the spin polarization of the Fe_5GeTe_2/graphene interface was calculated by considering both the spin valve and the Hanle signals. The magnitude of the spin-valve signal can be defined as:

$$R_{nl} = \frac{P_{ip,FGT} P_{Co} \lambda_{gr} R_{sq} exp(-L_{ch}/\lambda_{gr})}{2 w_{gr}} \tag{4.1}$$

where only the in-plane spin polarization of Fe_5GeTe_2, $P_{ip,FGT}$, is unknown; and the other parameters are extracted from the Co-Co reference zHanle measurements [159] (P_{Co} is the spin polarization of Co contacts, λ_{gr} is the spin diffusion length, R_{sq} is the square resistance of graphene, L_{ch} the channel length and w_{gr} the width of the graphene channel).

Device	**Type**	L_{ch} (μm)	w_{FGT} (μm)	w_{gr} (μm)	D_s (m^2/s)	τ_s (ps)	λ_{gr} (μm)	R_{hetero} (kΩ)		$\|P\|$ (%)	**Note**
Device 1	Co-Co	10.1	2.0	1.8	0.027	143	1.96	8		4.0±0.6 (Co)	zHanle
	FGT-Co	5.1							ip	2.6 (FGT)	SPV
									z	3.3 (FGT)	xHanle
Device 2	Co-Co	6.9	2.8	1.7	0.008	198	1.26	6		10.1±4.1 (Co)	zHanle
	FGT-Co	3.2							ip	44.9 (FGT)	SPV
									z	9.5 (FGT)	xHanle
Device 3	Co-Co	3.2	1.8	2.0	0.033	228	2.74	1.2		5.8±0.2 (Co)	zHanle
	FGT-Co	7.5							ip	2.8 (FGT)	SPV
									z	-	-
Device 4	Co-Co	7.0	1.8	1.2	0.02	162	1.80	0.33		6.0±0.9 (Co)	zHanle
	FGT-Co	3.7							ip	1.2 (FGT)	SPV
									z	-	-

Table 4.1: Summary of FGT-Co spin valve devices and extracted parameters. L_{ch}, w_{gr}, D_s, τ_s, λ_{gr}, $|P|$ are the graphene channel length, width, spin diffusion constant, spin lifetime, spin diffusion length, and FGT or Co spin polarization (in absolute value). w_{FGT} is the width of FGT. R_{hetero} is the interface resistance of FGT with graphene. CVD and Exf are the CVD and exfoliated graphene devices. zHanle, SPV (spin valve signal), and xHanle are the methods to extract the spin polarization. P_{ip} is the in-plane spin polarization with a saturated magnetization and P_z is the remanent spin polarization along the z-axis at the FGT/graphene interface.

The magnitude of the Hanle signal is defined as:

$$R_{\mathrm{nl}}(B_\perp) = \pm\frac{P_{z,FGT}P_{Co}R_{sq}}{w_{gr}}\int_0^\infty \sqrt{\frac{D_s}{4\pi t}}\exp\left[-\frac{L_{ch}^2}{4D_st}\right]\cos(\omega t)\exp\left[-\frac{t}{\tau_{\mathrm{s}}}\right]\mathrm{d}t \quad (4.2)$$

ω is the Larmor precession frequency, D_s is the spin diffusion constant, and τ_s is the spin lifetime. From the xHanle, the out-of-plane spin polarization of Fe_5GeTe_2 is calculated $P_{z,FGT}$.

The calculated in-plane spin polarizations for the different devices cover the range $|P_{ip,FGT}| = 1.2 - 44.9\%$, while the calculated out-of-plane spin polarization was extracted to be $|P_{z,FGT}| = 3 - 9.5\%$. It should be noted that the saturated in-plane spin polarization is different from the out-of-plane remanence spin polarization in Fe_5GeTe_2. Detailed spin parameters of the different measured devices are summarized in Table 4.1. The observed variation of the spin polarization in different devices can be due to compositional variations between different Fe_5GeTe_2 flakes [130] as well as different Fe_5GeTe_2/graphene interface conditions[162, 163].

4.3 Graphene spin valves with $(Co_{0.15}Fe_{0.85})_5GeTe_2$

To experimentally verify the in-plane magnetization and spin polarization in $(Co_{0.15}Fe_{0.85})_5GeTe_2$ (CFGT), we fabricated lateral graphene spin valve devices using exfoliated CFGT flakes similar to the FGT/graphene spin valves. In this case, spin current can be injected/detected by CFGT on a CVD graphene channel and detected/injected by a reference ferromagnetic Co contact. As the aspect ratio of CFGT is an important factor in determining the magnetic shape anisotropy and the easy axis of magnetization, a very narrow CFGT flake ($W_{CFGT} \sim 0.7\mu$m and thickness of ~ 30 nm) was used to achieve a stronger magnetic shape anisotropy and a nearly single magnetic domain state at the interface with graphene.

Similarly, the lateral CFGT/graphene heterostructure spin valve device can probe the interfacial spin polarization and, hence, the magnetic anisotropy of thin CFGT flakes. We performed nonlocal spin transport measurements on a graphene spin valve to quantify the injected (detected) spin current by a thin CFGT flake.

4.3.1 Spin injection and detection with $(Co_{0.15}Fe_{0.85})_5GeTe_2$

Figure 4.5a illustrates the nonlocal measurement configuration, where the current is passed through the Co-graphene interface (injector circuit), and voltage is measured at the CFGT-graphene interface (detector circuit). Figure 3b shows the nonlocal spin valve data for the detection of spin current by CFGT (Device 1) with the magnetic field sweep along the y-axis (B_y) at room temperature. This allows the control of the relative orientation of the magnetic moment of the injector (Co) and detector (CFGT) from parallel to antiparallel orientations resulting in the spin valve signal with two resistance states. Since the reference Co contacts have a magnetic easy axis along the y-direction, the observation of a spin valve signal confirms the detection of in-plane S_y spins by the detector CFGT contact. Noticeably, the CFGT shows sharp switching with a clear remanence and hysteresis in the spin valve signals, indicating the presence of dominant S_y spin polarization. This is also replicated in minor loop measurements with forward and backward field sweeps before reaching the Co coercive field (Figure 4.5c). The data measured in the two magnetization configurations show an apparent memory effect. Spin detection by CFGT using a different contact inDevice 1 is and spin injection by CFGT in another device (Device 2) was also measured.

We performed control measurements to probe the sign of spin polarization at the CFGT/graphene interface and compared it to the standard Co/graphene contacts by measuring a purely Co-Co (injector-detector) device. It is well-established that Co has a positive spin polarization, which means that the majority of spins at the Fermi level are parallel to its bulk magnetization [164]. However, we observed a reversal of the spin-valve signal when we compared Co-CFGT to Co-Co at the same bias condition (Figure 4.5d). We plot the detailed bias-dependent spin signal for Device 1 in Figure 4.5e, where the polarity of the spin-valve signal for the Co-CFGT and Co-Co devices changes according to the polarity of the bias current and follows a linear trend for the range of current considered. Note that the opposite polarity for the measured spin-valve signals for Co-CFGT and Co-Co remains consistent throughout the bias range considered. For different current bias polarities, the mechanism for spin accumulation at the interface of the injector magnet and the graphene transport channel changes between spin injection ($+I_{dc}$) or spin extraction ($-I_{dc}$). Considering the Co injector, for positive bias, spin-polarized electrons tunnel from Co into the graphene channel, accumulating a spin population at the interface with polarization in accordance with the spin polarization of Co. On the other hand, when we apply a negative bias, electrons from graphene tunnel into the injector. In this case, since there are more available states for majority spin electrons in Co, more majority spin electrons will be extracted from the graphene channel, creating a nonequilibrium spin population in graphene dominated by minority spin electrons, as illustrated in the inset of Figure 4.5d. This can further be analyzed by looking at the expression for the amplitude of the nonlocal spin-valve signal as described in Equation 4.1 [165].

The opposite nonlocal spin valve signals observed in these devices indicate opposite spin polarizations of the Co and CFGT contacts on graphene. This means that CFGT has a negative spin polarization and that the minority density of states is larger than the majority density of states at the Fermi level. In this case, when we apply a bias on the Co injector, and align the magnetic moments of Co and CFGT, the spin polarizations of the detector and injector have opposite directions, hence opposite signs are expected for the Co Co and Co-CFGT devices. This observation is further substantiated by calculations of the density of states

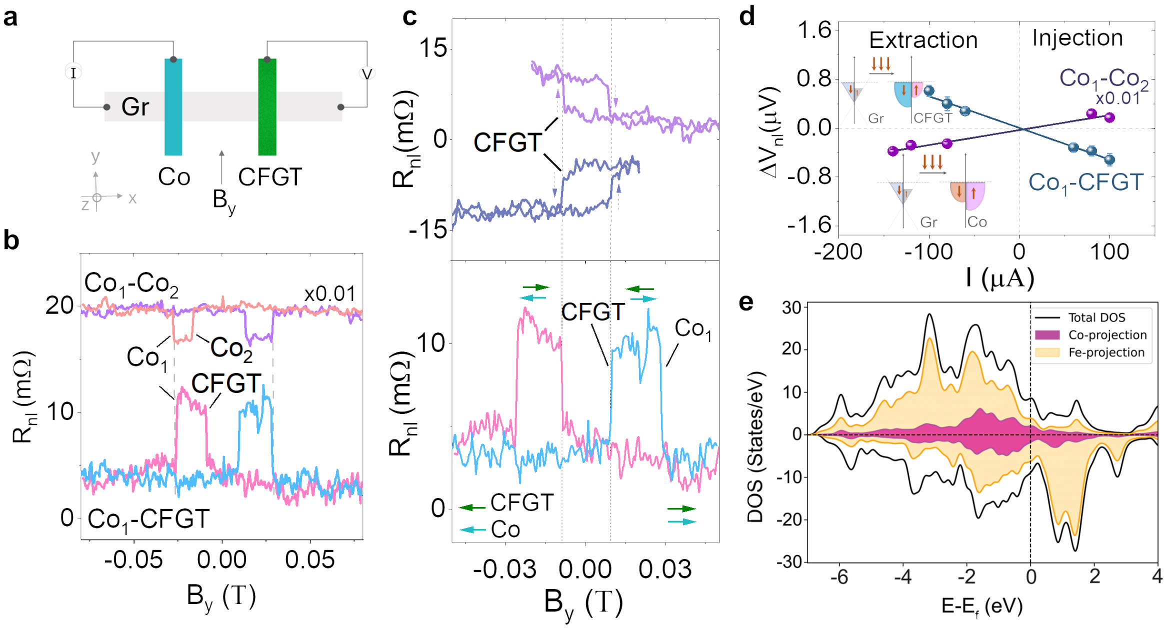

Figure 4.5: Lateral spin valve with CFGT/graphene heterostructure at room temperature. a. Schematic diagram for nonlocal spin valve for Co(injection)-CFGT (detection) configuration for Device 1. (b) Measured spin valve signal for Device 1, showing sharp switching for both CFGT and Co magnetic contacts. The arrows represent the direction of magnetization of CFGT and Co through a magnetic sweep. (c) Minor-loop measurements of CFGT. The arrows indicate the CFGT magnetic moment switching under the up- and down-sweep of the magnetic field. (d) Comparison of measured nonlocal spin valve signals of Co-CFGT and Co-Co devices, showing the opposite sign for the same polarity of applied bias current of 100 μA. The signals are shifted along the y-axis, and the signal for Co-Co was rescaled by ×0.01 for clarity. (e) Bias dependence of the spin signal for both Co-CFGT and Co-Co spin valve devices in the spin injection and extraction regimes, showing opposite spin polarization for Co and CFGT contacts. The error bars are estimated from the standard deviation of the measured data. The insets show the detection mechanism of the spin current for Co_1-CFGT and Co_1-Co_2 devices. (f) DOS (solid black line) and pDOS (colored shaded) for 20.1% doped CFGT, where orange represents the density of Fe states and magenta represents the density of Co states.

(DOS) and the projected density of states (pDOS) for CFGT Figure 4.5e. The spin polarization can be calculated by using the expression spin polarization = $\frac{N\uparrow - N\downarrow}{N\uparrow + N\downarrow}$ where N is the density of states at the Fermi level (solid vertical black line), and the arrows ↑ and ↓correspond to the majority and minority spin directions, respectively. Accordingly, a negative spin polarization of -2.1% and -7.9% was calculated for 20.1% and 13.4% Co doping, respectively. Right at the Fermi level, the Co atoms have a positive spin polarization (magenta-shaded curve), which competes with the overall negative polarization of the Fe atoms, decreasing the magnitude of the negative spin polarization. Consequently, the magnitude of spin polarization should decrease as the Co atom concentration increases, hence CFGT has a smaller spin polarization, compared to pure FGT.

4.3.2 In-plane anisotropy in $(\text{Co}_{0.15}\text{Fe}_{0.85})_5\text{GeTe}_2$

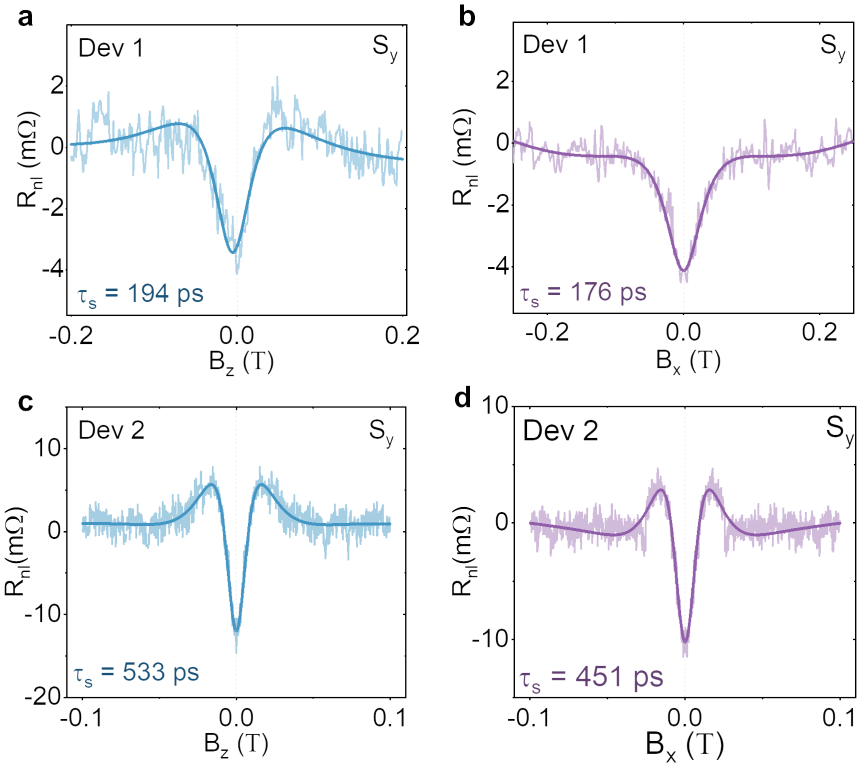

Figure 4.6: Hanle spin precession measurements in the CFGT-graphene heterostructure at room temperature. a. and **c.** Measured symmetric zHanle spin precession signal and the data fitting for Device 1 (CFGT as detector) and Device 2 (CFGT as injector), showing the dominant S_y spin polarization component of CFGT at room temperature. A linear background is subtracted from the measured data. **b.** and **d.** The measured symmetric xHanle spin precession signal and data fitting for Device 1 and Device 2 show the dominant S_y spin polarization component of CFGT at room temperature. A linear background is subtracted from the measured data.

To unambiguously prove the spin signal in our devices, we conducted Hanle spin precession experiments in both the z-axis (zHanle) and the x-axis (xHanle) geometries [159]. This helps to evaluate the spin lifetime and diffusion length in the graphene channel and to estimate the spin polarization of the CFGT/graphene interface in different orientations, which provides a direct probe to the direction of the magnetic moment of CFGT. In zHanle, the out-of-plane magnetic field B_z drives the injected spins to precess in the x-y plane. Spin precession results in a B_z-dependent evolution of the nonlocal spin signal. The measured nonlocal

Hanle signal is proportional to the spin polarization of injector and detector ($R_{nl} \propto P_{in}P_{de}$), with $P_{in(de)}$ being the spin polarization of the injector (detector), and a symmetric (antisymmetric) signal corresponds to an initial $S_{y(x)}$ spin state.

As presented in Figure 4.6a, for Device 1, the data for the nonlocal zHanle signal constitutes a symmetric curve suggesting a parallel state of the injected spins S_y with the magnetic moments of the CFGT detector. For Device 2 (Figure 4.6c), the signal is obtained by presetting the injector (CFGT) and detector (Co) to parallel and antiparallel states. The decomposed average zHanle signal shows only symmetric components, which means that, like Device 1, the injected spins by CFGT have only components along the y-axis, S_y. Similarly, the xHanle measurement is performed with the external B_x field applied along the x-axis, inducing a spin precession in the yz-plane. The observation of a symmetric xHanle curve in Figure 4.6b and d, for Device 1 and Device 2, demonstrates the dominant in-plane spin component S_y at the CFGT/graphene interface. From these precession measurements, we excluded any out-of-plane (S_z) contributions for both Device 1 and Device 2, proving the strong in-plane magnetization of CFGT. In addition, by choosing flakes with the long axis along the y-direction, we were able to obtain only S_y components, which translates to a magnetic moment in CFGT that is along the y-direction (M_y). This is different from earlier reported Hanle precession measurements in Fe_5GeTe_2/graphene spin valve, where contributions from S_x, S_y, and S_z were observed pointing to a canted magnetization of Fe_5GeTe_2.

By fitting the measured signal using the Hanle formula (Equation 4.2) [165], we evaluate the spin lifetime and the spin diffusion length in graphene channel from zHanle to be $\tau_s = 194 \pm 29$ ps and $\lambda_{gr} = 2.1 \pm 0.3$ μm for Device 1; and $\tau_s = 533 \pm 20$ ps and $\lambda_{gr} = 4.27 \pm 0.2$ μm for Device 2. From xHanle, we extract comparable spin transport parameters: $\tau_s = 176 \pm 14$ ps and $\lambda_{gr} = 2.5 \pm 0.2$ μm for Device 1; and $\tau_s = 451 \pm 18$ ps and $\lambda_{gr} = 3.42 \pm 0.1$ μm for Device 2.

4.3.3 Spin polarization at the $(Co_{0.15}Fe_{0.85})_5GeTe_2$/graphene interface

We can extract the spin polarization at the CFGT/Gr interface (for Device 2) to be 4.93% and 4.5%, using Equation 4.1 and Equation 4.2, respectively, considering a measured spin polarization of 4.8% in the reference Co/TiO_2/Gr contact. The spin injection efficiency can be influenced by the conductance mismatch and spin absorption effects between the ferromagnet and graphene. Since the resistance in graphene and ferromagnets differ by a few orders of magnitude, usually a tunnel barrier is introduced to improve conductance matching [166].

4.4 Interface assessment and conductance mismatch in FGT/graphene and CFGT/graphene

Conductance matching between the ferromagnetic contact and the channel material is a basic requirement for efficient spin injection and detection. The difference in the spin resistance of the ferromagnet $R_{s,Co}$ and the nonmagnetic channel materials $R_{s,gr}$ is the basic physical parameter, where $R_{s,FM} = \rho_{FM}\lambda_{FGT}/(t_{FGT}w_{FGT})$ and $R_{s,gr} = \rho_{gr}\lambda_{gr}/(t_{gr}w_{gr}) = R_{sq}\lambda_{gr}/w_{gr}$ [167, 168]. By adopting the analytical formulation based on the drift-diffusion model proposed by Takahashi and S. Maekawa [169], we can calculate the nonlocal spin valve signals for parameters obtained in FGT-Co spin valves on CVD and exfoliated graphene devices (Figure 4.7a) and in CFGT-Co devices on CVD graphene (Figure 4.7b). As the interface resistance of FGT/graphene is in the range of 6-8 kΩ, it is good enough to overcome the conductance mismatch issue, showing nearly optimal signals for both devices. However, for FGT/graphene devices with lower interface resistance the conductance mismatch issue can be more obvious. Similarly, for CFGT/graphene, Device 1 has a higher interface resistance of around 2 kΩ, which shows that the spin valve signal is not affected. Device 2, on the other hand, has a more transparent interface resistance of 200 Ω, resulting to a nonlocal signal that is lower than the nominal, reflecting a more pronounced effect of conductance mismatch. These analyses show the effect of interface resistance variations in the FGT/graphene and CFGT/graphene heterostructures on the nonlocal spin signal and spin injection efficiency.

To further elucidate the effect of FGT and CFGT on spin relaxation in graphene, we calculate the spin absorption rate Γ with a simplified model [170, 171]:

$$\Gamma = \frac{R_{\mathrm{sq}}D_s}{\rho_{\mathrm{FM}}\lambda_{\mathrm{FM}} + R_iA} \approx \frac{R_{\mathrm{sq}}D_s}{R_iA} \tag{4.3}$$

where R_{sq}, and D_s are the graphene channel square resistance and spin diffusion constant, respectively; ρ_{FM} and λ_{FM} are the resistivity and spin diffusion length of the ferromagnet, respectively; R_i is the interface resistance and A is the interface area of vdW ferromagnet/graphene heterostructure, where $\rho_{FM}\lambda_{FM}$ is negligible compared to R_iA. Based on the experimental parameters of the CVD and exfoliated graphene devices, we can further calculate the spin lifetime from the spin absorption rate. i.e. $\tau_{s,abs} = 1/\Gamma$ and the total spin relaxation time is given by $1/\tau_{s,tot} = 1/\tau_{s,SOC} + 1/\tau_{s,abs}$. One can see that the spin absorption contribution ($R_{abs/tot} = \tau_{tot}/\tau abs$) is less than 8% for FGT/grapheneDevice 1 or 5% for Device 2 (Figure 4.7b). On the other hand, spin absorption is more pronounced in the CFGT/graphene devices (Figure 4.7)b. We obtained a spin absorption contribution of 80% for Device 1 and 61% for Device 2. The higher spin absorption

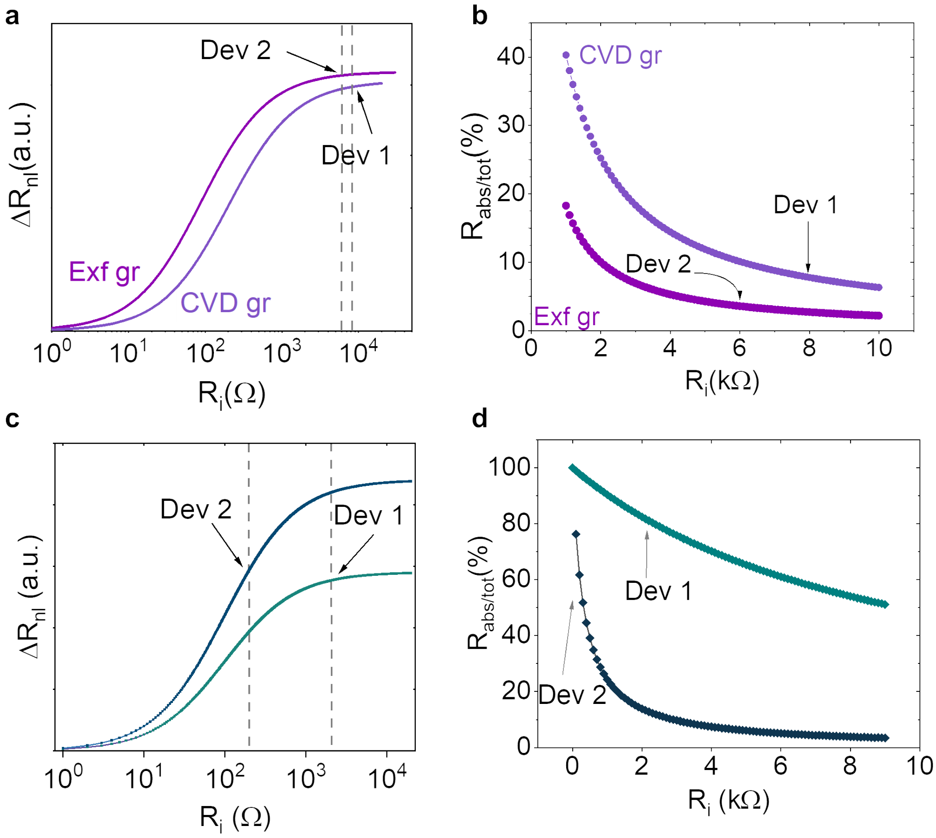

Figure 4.7: Conductance mismatch and spin absorption at the FGT/graphene and CFGT/graphene interfaces a. and **c.** Calculated nonlocal spin signal as a function for FGT/graphene and CFGT/graphene devices, respectively. R_i is the interface resistance in the vdW FM/graphene heterostrcuture. Dashed lines indicate the measured interface resistances in our devices. **b.** and **d.** Calculated spin absorption ratio as a function of the interface resistance R_i and square resistance R_{sq} of the graphene channel for FGT/graphene and CFGT/graphene devices, respectively.

for Device 1 is due, in part, to the high graphene channel resistance of $\approx 3.3k\Omega$, which is one order of magnitude higher, compared to the channel resistance in Device 2. Further optimization of the interface resistance by using appropriate 2D tunnel barriers can provide higher spin injection efficiency in graphene and minimize spin absorption.

5 Detection of spin texture in Fe_5GeTe_2 by graphene spin valve

In this chapter, we demonstrate room temperature electrical detection of magnetic spin textures in the van der Waals magnet Fe_5GeTe_2 (FGT), in a graphene-based spin valve device. Spin texture nucleation was enabled by Fe_5GeTe_2 nanolayer flakes with structural features such as constrictions or notches. These engineered geometries enable the injection of varied spin orientations into the graphene channel, leading to anomalous multilevel spin valve switching and the observation of Hanle spin precession. Our findings offer key insights into electrically probing magnetic spin textures in Fe_5GeTe_2 through graphene-based spintronic platforms.

5.1 Spin texture spin valves in graphene-based devices

The schematic diagram of the lateral spin valve device with an Fe_5GeTe_2 electrode with constriction is shown in Figure 5.1a, with the corresponding optical image and the nonlocal measurement geometry of Device 1 in Figure 5.1b. In this study, we employ a nonlocal spin valve device comprising of two electrodes: (1) ferromagnetic electrode featuring a spin texture (ST) in the vdW ferromagnet FGT, and (2) a conventional cobalt (Co) electrode exhibiting a quasi-single domain (SD) configuration. FGT is known for its non-centrosymmetric $\sqrt{3} \times \sqrt{3}$ surface superstructures [81, 130] and the presence of exotic chiral spin configurations, such as stripe domains and skyrmionic textures which arise from Dzyaloshinskii-Moriya interaction (DMI) [129, 172]. However, these spin textures often form spontaneously across the film. To achieve controlled nucleation of domains or skyrmions, structural patterning techniques such as introducing constrictions, notches, or engineered defects are commonly used [173].

In our device, we use an FGT nanolayer flake with a constriction to localize and stabilize the spin texture (Figure 5.1b). Spins originating from this textured FGT region are injected into the graphene channel, where they propagate and are ultimately detected by the Co electrode. The well-characterized magnetic switching behavior of the Co reference electrode in graphene spin-valve systems [174] serves as a reliable baseline for detecting and analyzing the spin textures introduced by the FGT electrode.

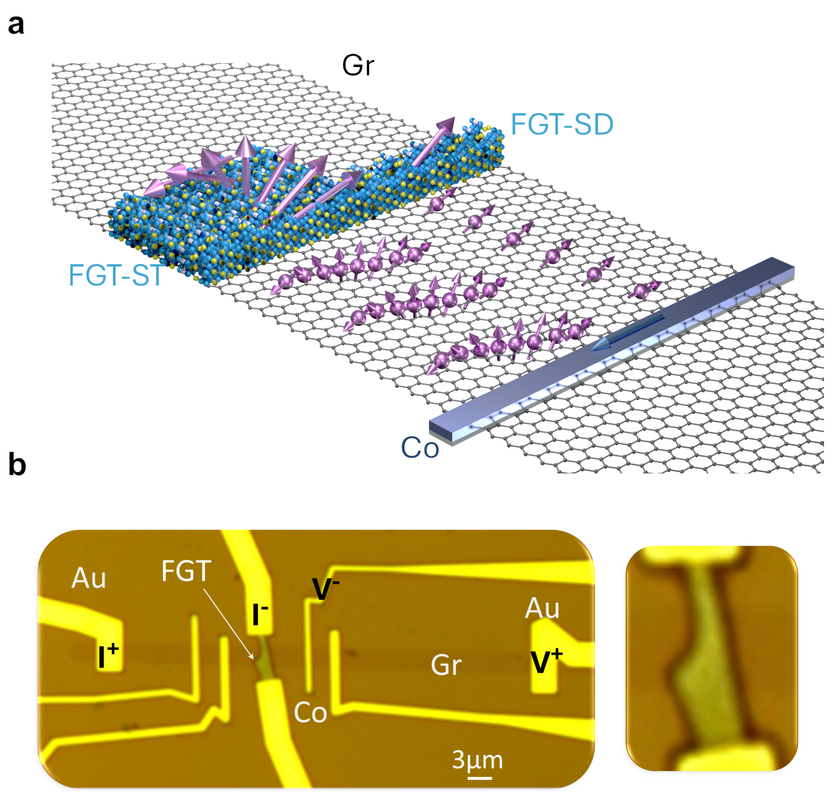

Figure 5.1: Spin texture spin valves in graphene-based devices. a. Schematic illustration of spin injection in graphene by Fe_5GeTe_2 with spin texture (ST) and single domain (SD) components. The arrows represent the spin textures and spins on the graphene channel. **b.** Optical image of Device 1 consisting of Fe_5GeTe_2 with a constriction to host magnetic spin textures, which is used for spin injection into CVD graphene channel with reference magnetic cobalt (Co) and nonmagnetic gold (Au) contacts. Current (I_-/I_+)and voltage (V_-/V_+) configurations for the nonlocal spin valve measurement geometry is indicated. The right panel of **b** shows a magnified microscope picture of the FGT flake with a constriction.

First, we schematically explain the expected differences between conventional and spin texture spin valve signals as a function of the external magnetic field (Figure 5.2a). The FGT with a constriction should have a region with spin textures as well as a region of aligned magnetic domains. Compared to the conventional single domain (SD-SPV) spin valve signal with one switching for FGT and the other for Co (Figure 5.2a, top panel), the spin-texture (ST-SPV) spin valve signal is expected to have multi-state switching (Figure 5.2a, bottom panel). In ST-SPV, a sharp switch from low resistance (stage I) to an intermediate resistance state (stage II) occurs at the $-B_y$ range due to spin textures of FGT. At the low positive field ($+B_y$), a gradual switch to the high resistance state due to spins aligning from the SD component in FGT (stage III) is followed by a sharp switch back to the intermediate state due to the Co electrode (stage IV), and upon further increase of the magnetic field, another switch from the intermediate state to the low resistance state occurs due to the realignment of the spin texture in FGT (stage V).

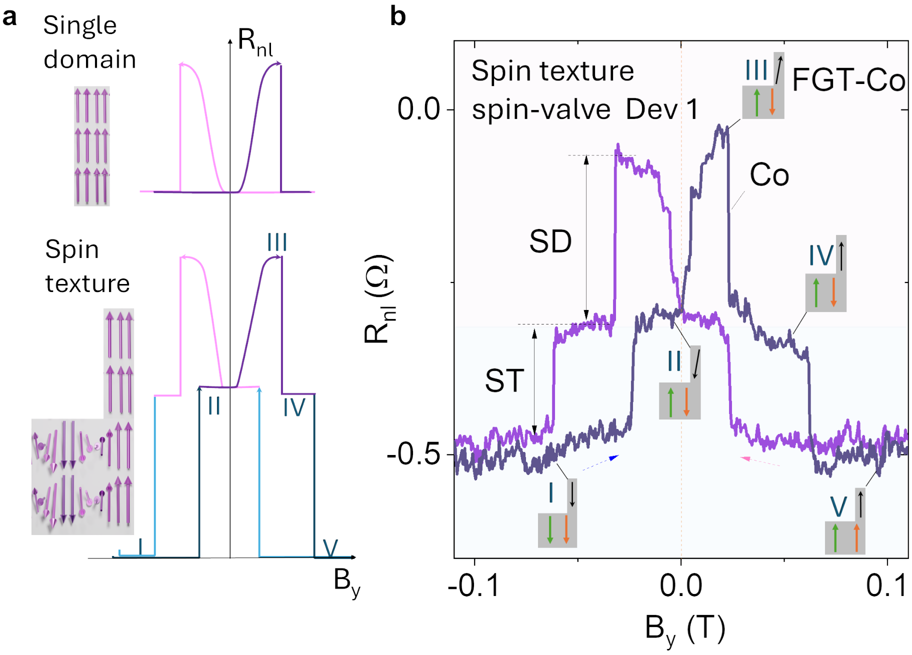

Figure 5.2: Electrical detection of spin textures in Fe_5GeTe_2. a. Illustration of the conventional single domain (SD) (top panel) and spin textures (ST) (bottom panel)with their corresponding spin valve signals. **b.** Measured spin-texture spin valve (ST-SV) signal using constricted FGT as the injector and Co as the detector at room temperature in Device 1. Stage I-V corresponds to different spin-texture statuses as a function of B_y. The black arrow indicates the SD component. The green and orange arrows represent the effective sub-domain structures of the ST component projection along the y-axis. Dashed arrows show the field sweep direction.

Specifically, the FGT spin texture spin valve (ST-SPV) data measured at room temperature as a function of B_y is presented in Figure 5.2b. Multi-state switching is observed for both forward and backward magnetic fields B_y sweep. First, we explain the forward magnetic field sweep curve (indigo color), where at both large negative and large positive field ranges (state I and V), all magnetic domains are reoriented to align with the field into a single magnetic moment in parallel with the Co detector, leading to low resistance states of the spin valve signal. However, at low fields (stage II), the spin texture state of FGT is maintained as it is more energetically favorable near zero fields, thereby resulting in a near zero net magnetization and, equivalently, an intermediate resistance state (stage II) in the spin valve signal. After crossing the zero field from $-B_y$ to $+B_y$, the transition from stage II to III is attributed to the conventional magnetic domain switching of FGT. It should be noted that the slow decrease in stage IV is due to the realignment of the canted domain with the y-axis. This is in agreement with our previous work on stripe-like FGT/graphene heterostructure[31]. These observationsbindicate the coexistence of spin textures and canted magnetic domains in the constricted FGT at room temperature. Therefore, strictly speaking, stages IV and II are not due to the same magnetic domain state, though they have almost the same signal magnitude. A further increase in the magnetic field (around 60 mT) breaks the spin texture and aligns all of them to form a single domain again (stage V). When the magnetic field sweeps back, a similar signal can still be observed, proving the robustness of the spin textures spin valve signals.

By comparing the conventional Co-Co and FGT_{stripe}-Co spin valves single domain spin valves, we can distinguish the contribution of the conventional SD and ST components in the spin valve signals more clearly. Figure 5.3a and b show the constricted FGT-Co_1 and Co-Co_1 spin valve configurations and signals, where both configurations share the same Co_1 contact as the detection electrode. The same coercive field of Co_1 contact suggests that the separation of stage III and stage IV is merely due to the Co magnetization reversal (Figure 5.3b). That is, stage III and stage IV comes from the same type of magnetic domain in FGT, due to a continuous realignment from its tilt easy axis to $+B_y$ [31]. A further repeating observation of the spin texture spin valve signal with different Co detector and measurement geometry confirms the robustness of the spin injection of ST and SD components in such constricted FGT. Moreover, a comparison of the constricted FGT and the stripe FGT_{stripe}-Co spin valve signal (Figure 5.3c and d) shows that the constriction in FGT does not affect the behavior of the SD component, specifically its magnetic anisotropy and coercive field. Instead, it helps to pin the spin textures leading to different magnetic domains.

Low temperature spin valve measurements were also performed for Device 1. In Figure 5.3e, the low temperature (60 K) spin valve measurement is compared with the room temperature (300 K) signal. The magnitude of the spin valve signal is significantly amplified at the lower temperature, and the coercive fields are shifted to higher fields. Finer switching features, both at low fields and high fields, become evident, which can be attributed to the multiple domains in FGT.

For the SD contribution, the coercive field (stage II to stage III) has increased as expected due to enhanced magnetic anisotropy at lower temperatures, similar to that of the Co contact. Noticeably, we also observe a non-uniform shift in the coercive fields of the ST component. As highlighted with the dashed lines and arrows in Figure 5.3e, the 'recover field' of the ST component, which refers to the transitions from stage I to stage II, does not change with temperature. However, the coercive field (stage IV to stage V) has increased. This observation is consistent during both the forward-sweep and backward-sweep of the magnetic fields. This behavior of the spin texture is quite different from that of conventional FM domains like Co and SD counterparts in FGT. This may be due to the pinning

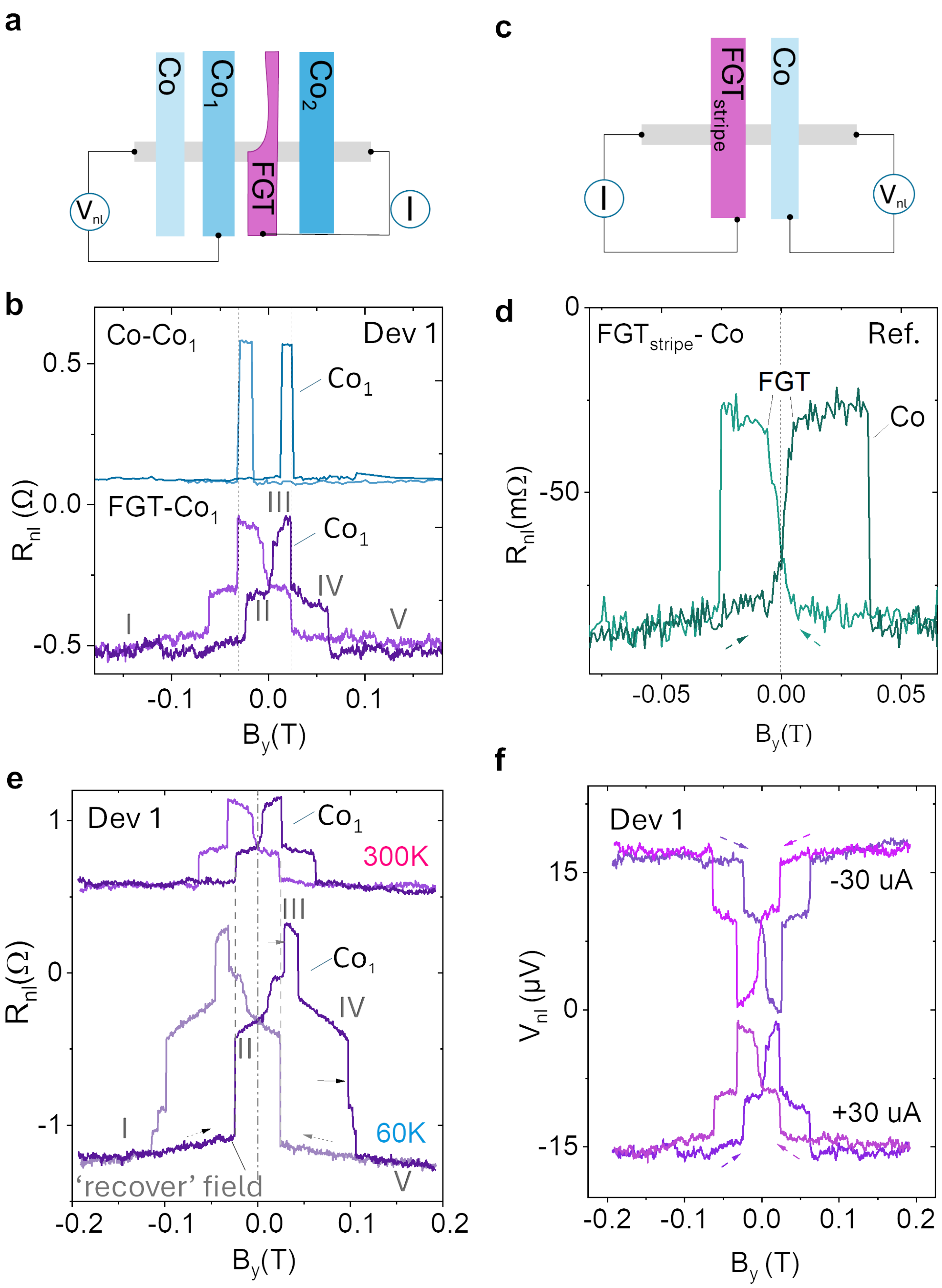

Figure 5.3: Comparison of spin texture spin valve (ST-SPV) with conventional quasi single domain spin valve (SD-SPV) signals. a., b. Spin valve measurements schematics and signals for constricted FGT-Co$_1$ and reference Co-Co$_1$ device in Device 1. **c.,d.** Representative spin valve measurement geometry and signal for stripe-like FGT$_{stripe}$-Co device with only SD component. **e.**Temperature dependent spin texture spin valve signals at 60 K and 300 K of Dev 1 at a bias current of +30 μA. **f.** ST spin-valve signal for opposite current polarity (± 30 μA) of Device 1, resulting in the reversal of the signal.

effect of the spin textures caused by the constriction. Figure 5.3f shows the effect of different bias polarities, where the sign of the nonlocal voltage signal reverses but the signal magnitude stays comparable.

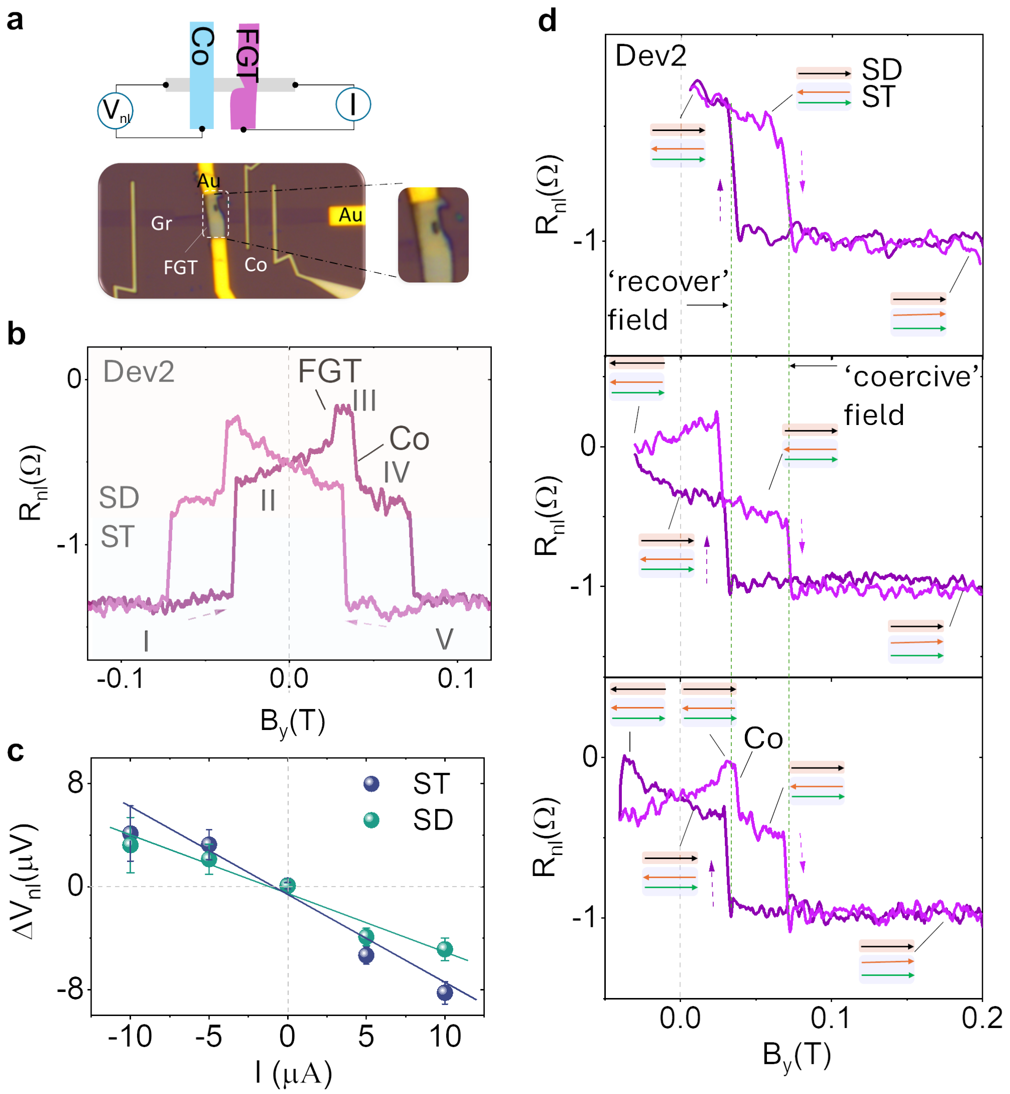

Figure 5.4: Spin-texture spin valve signal from Fe_5GeTe_2 with a notch. a. Schematics and optical image of Device 2 using an FGT with a nothc. **b.** Measured spin-texture spin-valve signals with a notched FGT. SD and ST components are marked with different background colors. **c.** Bias dependence of the SD and ST components. **d.** Minor loop measurements of the spin valve signal. Light (dark) magenta curves are the forward (backward) sweep, respectively. Insets show the corresponding domain structures at critical field range. The black arrow indicates the SD component. The green and orange arrows represent the effective domain structures of the ST component projection along the y-axis.

Next, we investigated a spin texture spin valve device with a notch in the FGT electrode (Device 2) (Figure 5.4a), which shows the same multi-state switches (stages I-V) with the coexistence of ST and SD states (Figure 5.4b). A further detailed bias dependence of the SD and ST components shows a linear trend as a function of the bias (Figure 5.4c), proving the linear regime spin injection of both SD and ST components at the small bias range. Detailed investigation of the minor loop measurement (Figure 5.4d) in Device 2 shows the hysteresis or memory effect of the ST and SD components [159]. The top panel shows that the ST component has a large hysteresis effect. Noticeably, it always displays the same 'alignment'-coercive field and 'recover'-coercive field no matter how the magnetic field is swept (dark magenta and light magenta). The middle panel of Figure 5.4c proves the hysteresis effect of the conventional ferromagnetism (SD component) of FGT; while the bottom one confirms the hysteresis effect for both SD and ST components. This hysteresis effect in both SD and ST components exhibits a similar magnetic nature in response to the external field.

5.2 Hanle spin precession measurements

Hanle precession measurements are conducted to analyze the spin components with an out-of-plane magnetic field (zHanle) to assess in-plane spin polarizations (S_x and S_y). While xHanle measurements were carried out with a magnetic field applied along the graphene channel (x-axis), resulting in the precession of spins in the yz-plane and providing information on the injection of S_y and S_z polarizations. Figure 5.5a and b illustrate the zHanle signal in reference to the By spin valve signal, displaying the spin states from the components of the constricted FGT near zero field. Interestingly, by comparing it with the spin valve signal (B_y), the Hanle signal (B_z) indicates that the main contribution arises from spin injection from the SD part of the FGT. Furthermore, both symmetric and antisymmetric Hanle components extracted from the Hanle signal suggest the presence of S_y and S_x spin polarizations, aligning with the canted magnetization of FGT[104]. Since the spin texture at low fields have almost zero net magnetization, the contribution of the ST component to the Hanle signal at low fields is negligible.

More carefully controlled z(x)-Hanle experiments were performed with the pre-initiation of the parallel (P) and antiparallel (AP) magnetic alignments of the Co and the SD component of FGT (Figure 5.5c and d). In the zHanle signals of Device 2, it is confirmed that the SD contribution dominates for both P and AP configurations. Furthermore, the ST contribution to the zHanle signal can be ruled out by comparing the Hanle signals (P and AP) with the reference (B_y) spin valve signal magnitude (Figure 5.5d). The extracted symmetric and antisymmetric signals from the averaged signal $R_{nl} = [R_{nl(AP)} - R_{nl(P)}]/2$ indicate that both S_y and S_x spin polarization exist simultaneously in the SD component of the notched FGT as well (Figure 5.5h).

Furthermore, by comparing the xHanle signals (AP and P) with the reference

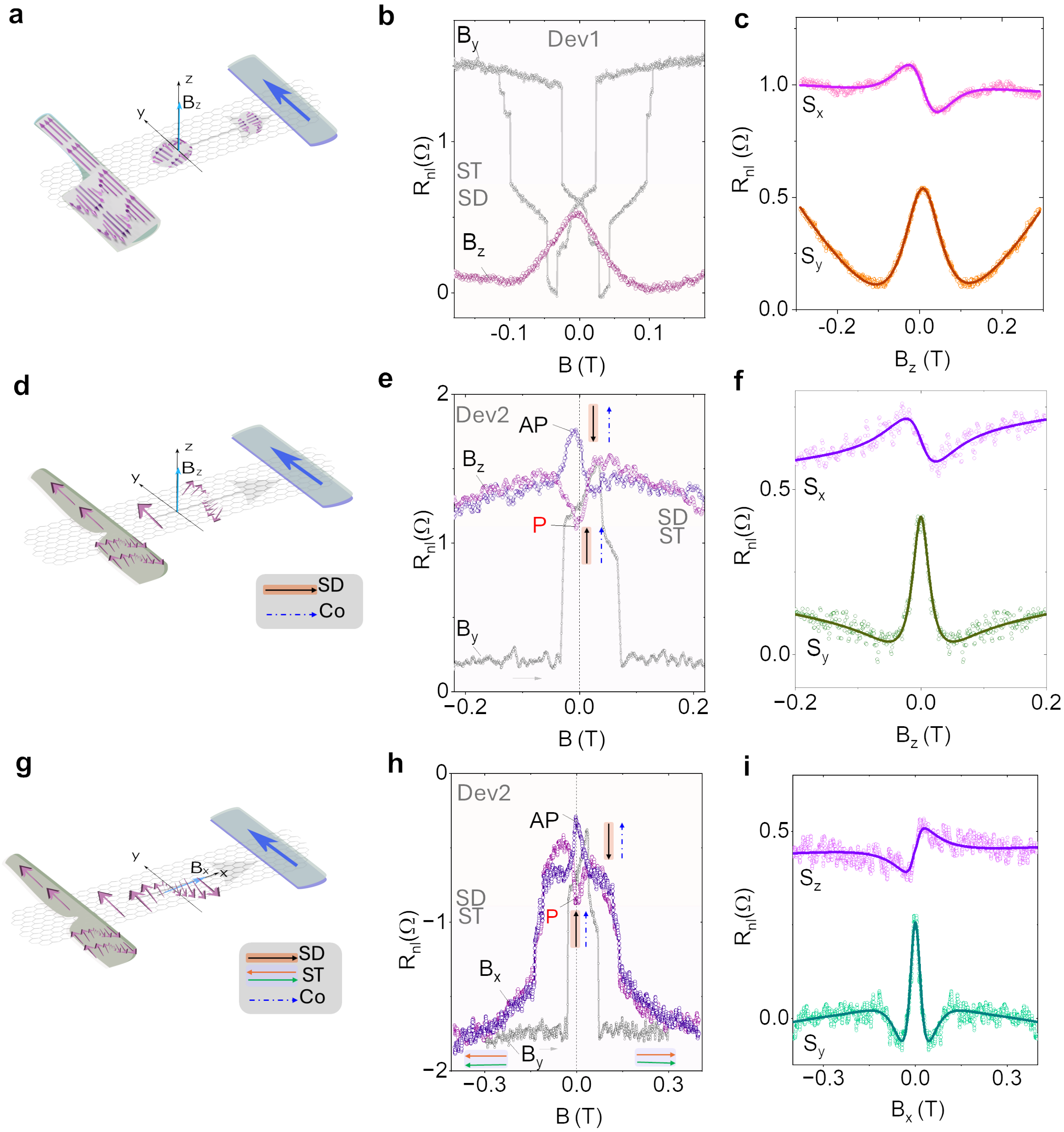

Figure 5.5: Hanle spin precession measurements of spin-texture spin valve devices. a., **b.** Measurement geometry and comparison between the nonlocal zHanle signal and the B_y spin valve signal of Device 1. **c.** Extracted symmetric and antisymmetric components from the zHanle in **b.**, **d.** Schematics and **e.** zHanle measurements in the notched FGT-Co spin valve with parallel (P) and anti-parallel (AP) magnetic moment of Co and SD of FGT. **f.** Extracted symmetric and antisymmetric components from the zHanle in **e.**. **g.** Schematics and **h.** xHanle signals with parallel (P) and anti-parallel (AP) configurations in Device 2. **i.** Symmetric and antisymmetric components from xHanle in Device 2. Reference spin valve signals with the magnetic field B_y are overlaid for comparison. For precision, no shift along the y-axis was made.

spin valve signal (B_y) in Figure 5.5f, we can confirm that the contribution is mainly from the SD component at a lower field as well. However, at the high field range of the xHanle signals, the switching behavior for both P and AP configurations behaves similarly to the reference (B_y) spin valve signal with a larger coercive field, which suggests the realignment for both SD and ST components. By averaging the xHanle P and AP signals, we can remove the non-spin-precession-related contributions [31]. The extracted symmetric and anti-symmetric components of the averaged signal are trivial at a large field range. In agreement with the zHanle signal, the xHanle spin precession is dominated by the mainly symmetric component, showing that the majority of the spins injected are oriented along y, and with a finite S_z spin population (Figure 5.5i). In summary, the detailed x(z)-Hanle signals with multiple spin polarizations confirm the tilted magnetization of the SD component in the constricted FGT [81] . While the ST component is more clearly observed in the B_y spin valve and magnetization rotation-induced Hanle signals. Furthermore, the observation of anomalous multi-level spin-valve switching and Hanle spin precession signals suggests that such a constriction/notch in FGT disrupts magnetic domains, enabling spin textures to persist alongside the conventional single magnetic domains.

5.3 Spin parameters and spin injection efficiency of Fe_5GeTe_2

To quantitatively describe the spin injection efficiency of Fe_5GeTe_2 in the graphene channel, we computed the spin polarization of FGT in the devices, with the results summarized in Table 5.1. Since we consider two active components for spin injection, the corresponding spin polarization, $P_{FGT,SD}$ and $P_{FGT,ST}$, are extracted exclusively for each ST and SD component. The corresponding measurement of $\Delta R_{NL,ST}$ and $\Delta R_{NL,SD}$ are marked in Figure 5.2 of the main text. The spin polarization of Co electrodes (P_{Co}), spin diffusion length λ_{gr} and spin lifetime τ_s are extracted from the reference Co-Co z(x)Hanle measurements. Using the Equation 4.1, we can extract spin parameters like spin polarization for the ST and SD components of the constricted/notched FGT, respectively [175].

Compared with conventional stripe-like FGTstripe-graphene and Co-Co nonlocal spin valve, the constricted/notched FGT-Co spin valve shows a clear ST spin injection, besides the normal SD counterpart. Furthermore, the spin injection efficiency of SD and ST was also evaluated from the spin valve signal (Table 5.1), it shows that both SD and ST have comparable spin injection efficiency PSD up to -20%, suggesting the ST component injection process behaves very similarly to conventional SD ones.

Parameter	**Device 1**	**Device 2**
R_{sq} (Ω)	950	818
L_{ch} (μm)	3.4	4.4
w_{gr} (μm)	1.9	2.0
λ_{gr} (μm)	2.0	1.9
τ_s (ps)	123	266
$R_{\mathrm{hetero.}}$ (kΩ)	4.0	2.7
$\Delta R_{\mathrm{nl,tot}}$ (Ω)	0.59	1.4
$\Delta R_{\mathrm{nl,SD}}$ (Ω)	0.31	0.59
$\Delta R_{\mathrm{nl,ST}}$ (Ω)	0.28	0.84
P_{Co} (%)	8.1	10.0
$P_{\mathrm{FGT,SD}}$ (%)	-6.1	-14.3
$P_{\mathrm{FGT,ST}}$ (%)	-5.6	-20.4

Table 5.1: Spin parameters extracted from the injection of FGT on the graphene channel at room temperature. R_{sq}, L_{ch}, w_{gr}, λ_{gr}, and τ_s are the graphene square resistance, channel length, channel width, spin diffusion length, and spin lifetime, respectively. R_{hetero} is the interface resistance of FGT/graphene, and $P_{FGT,ST(SD)}$ is the spin polarization of the ST and SD components of FGT

6 Self-induced spin orbit torque in Fe_3GaTe_2

In this chapter, the strong nonlinear Hall effect and self induced spin orbit torque (SSOT) in the above-room-temperature ferromagnet Fe_3GaTe_2 with strong perpendicular magnetic anisotropy (PMA) are investigated. The nonlinear Hall effect in Fe_3GaTe_2 is examined through temperature dependent measurements. Scaling analysis reveals large anomalous Hall angle while second harmonic Hall measurements indicate a damping-like self-induced spin orbit torque (SSOT) in Fe_3GaTe_2. Furthermore, partial magnetization switching, assisted by an in-plane magnetic field, is demonstrated, consistent with the SSOT geometry.

6.1 Large anomalous Hall effect in Fe_3GaTe_2

A van der Waals (vdW) ferromagnet with large perpendicular magnetic anisotropy (PMA) and above room-temperature Curie temperature (T_C) has been greatly anticipated to bridge the fundamental challenges in successfully realizing vdW based room temperature spintronic devices. Since the first report on Fe_3GaTe_2, a strong PMA ferromagnet with a record T_C of ~350-380 K and high saturation magnetization [47], several spintronic devices and proof-of-concept studies have already been reported taking advantage of these properties [108, 111, 176, 177].

Fe_3GaTe_2 belongs to the space group P63/mmc with a hexagonal structure, similar to Fe_3GeTe_2. Fe and Ga atoms are sandwiched between Te slabs while adjacent Te layers are separated by the vdW gap as shown in Figure 6.1a.

To perform electrical transport measurements, Hall bar devices were fabricated on exfoliated flakes. Hall measurements were performed at different temperatures using Quantum Design Dynacool physical property measurement system (PPMS) with an SR830 lock-in amplifier at a frequency of 213 Hz to probe the magnetic properties of Fe_3GaTe_2. The first harmonic response was measured to extract the anomalous Hall resistance, which depends on the equilibrium magnetization along the out-of-plane direction.

Figure 6.1b shows the anomalous Hall effect in Device 1, which is obtained from the first harmonic response after the subtraction of the linear ordinary Hall background. We calculate the magnitude of the anomalous Hall signal by taking the difference in the resistances at the positive and negative field saturation as expressed by the following: $R_{AHE} = (R_{(xy,+M)} - R_{(xy,-M)})/2$, obtaining $R_{AHE} =$

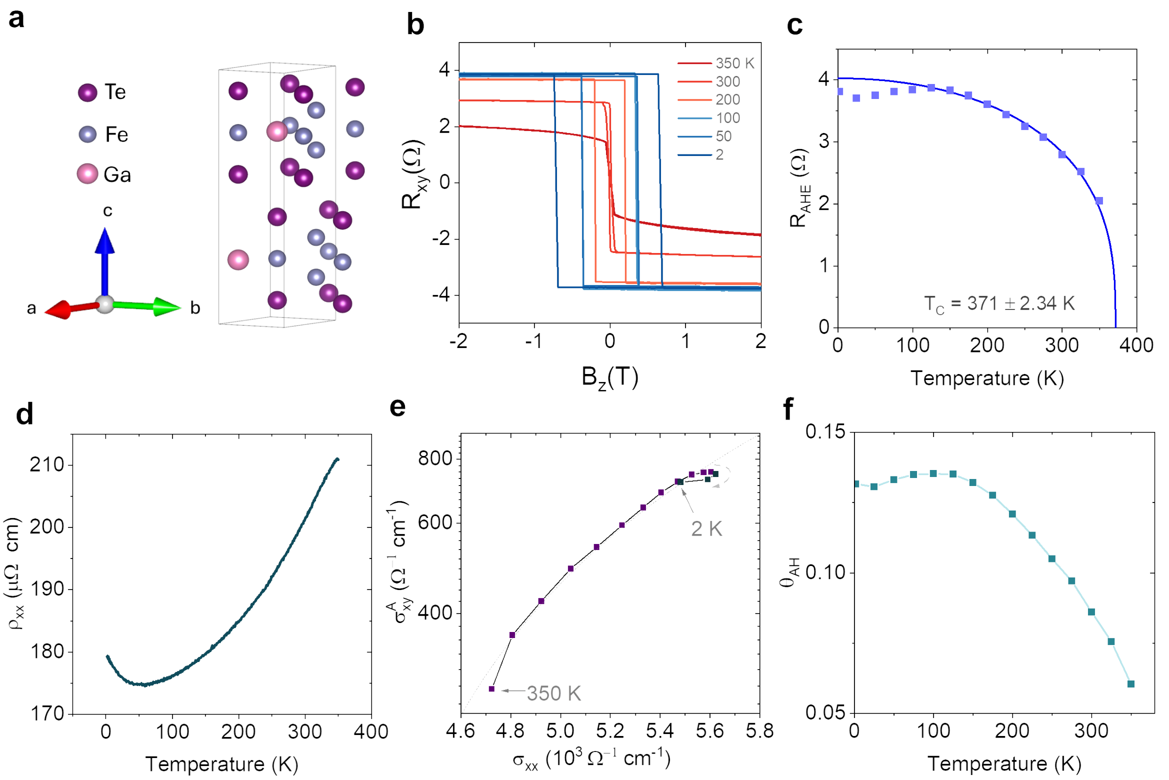

Figure 6.1: Large anomalous Hall effect in Fe$_3$GaTe$_2$. a. Layered crystal structure of Fe$_3$GaTe$_2$. **b.** Anomalous Hall effect in 62 nm thick Fe$_3$GaTe$_2$ flake (Device 1) at different temperatures after subtracting the linear ordinary Hall effect background. **c.** Solid symbols show the magnitude of the anomalous Hall extracted from **b** at different temperatures while the solid line is the fit to $R_{AHE}(T) = R_{AHE}(0)(1-(T/T_c)^a)^\beta$. **d.** Longitudinal resistance of Device 1 as a function of temperature. **e.** Scaling analysis of the anomalous Hall conductivity with the longitudinal conductivity showing two distinct behaviors: (I) Bad metal regime and (II) flat regime. **f.** Anomalous Hall of Fe$_3$GaTe$_2$ angle at different temperatures.

2.79Ω. Since the anomalous Hall component directly relates to the magnetization of Fe$_3$GaTe$_2$, we can analyze its temperature dependence to estimate the T_C. The solid symbols in Figure 6.1c show the temperature dependence of R_{AHE} while the line is the fit to $R_{AHE}(T) = R_{AHE}(0)(1-(T/T_C)^a)^\beta$ from which we extract the T_C =371.35±2.34 K, a=2.08, and β=0.34 which is consistent with earlier report [178].

Figure 6.1d displays the longitudinal resistivity of Fe$_3$GaTe$_2$ from 2 K to 360 K, which exhibits metallic behavior down to 60 K, below which an upturn n resistivity is observed. From the scaling analysis of the anomalous Hall component in Figure 6.1e, we observe a large anomalous Hall conductivity increasing from σ^A_{xy}=363 $\Omega^{-1}cm^{-1}$ at room temperature to σ^A_{xy}=730 $\Omega^{-1}cm^{-1}$ at 2 K - 50 K. Additionally, we observe two distinct regimes of anomalous Hall transport: (I) monotonic increase with increasing longitudinal conductivity, σ_{xx} and (II) a nearly saturating behavior for larger σ_{xx}. The first regime observed at high temperatures (50 K - 300 K) corresponds to the bad metal hopping regime, where the scaling relation follows σ_{xy}^{A}~$\sigma_{xx}^{1.66}$ [179, 180] (grey dotted lines in Figure 6.1e). In this regime, the transport is due to inelastic scattering of conduction electrons in the channel. In the second regime, the transport is characterized by the intrinsic anomalous Hall effect which originates from the Berry curvature. Additionally, we also extracted the anomalous Hall angle ($\theta_{AHE} = \sigma_{xy}^{A}/\sigma_{xx}$), as shown in Figure 6.1f, which quantifies the efficiency of the anomalous Hall effect in Fe_3GaTe_2. Compared to previous report on Fe_3GaTe_2 [144], we observe an anomalous Hall angle almost two times larger in Fe_3GaTe_2.

6.2 Field assisted current-induced magnetization switching of Fe_3GaTe_2

Switching experiments were performed to find out how the SSOT in Fe_3GaTe_2 could contribute in current-induced switching for SOT applications. Figure 6.2a shows the AHE loop for Device 2 shows sharp switching with a small component characterized with a broader tail before saturation. The magnitude of the signal is R_{AHE}=1.28 Ω with a coercive field of H_C=0.11 T. The switching experiments were performed by presetting the magnetization at $-M$ at sufficient negative magnetic field to obtain initiation points at $-M$ saturation before applying the assisting field and pulse current with a pulse width of 50 ms. A current of 200 μA was then used to read out the the magnetization state.

Figure 6.2b shows the current induced switching loops at different in-plane assisting fields. Switching was achieved at a critical current density of ~7x10^{10} A/m^2. For all the loops, the initiation points match the R_{AHE} at $-M$ saturation. We do not observe a loop zero assisting field, but a stronger loop is observed with applied in-plane fields. Moreover, the polarity of the switching loop (or the switching direction) reverses for positive and negative assisting fields. For positive assisting fields, the switching loop is in the clockwise direction and reverses to counterclockwise for negative fields. This behavior is opposite of what has been reported for Fe_3GaTe_2/Pt [110]. The switching percentage is summarized in Figure 6.2c. The field-assisted current-induced switching behavior observed agrees with the geometry of SSOT measured using second harmonic technique discussed in the next section. The decrease in switching percentage after ± 60 mT may be attributed to domain formation in Fe_3GaTe_2, at higher in-plane fields. Time-dependent switching experiments were also performed on Device 3 as shown in Figure 6.2d, with a more uniform response in the $+M$ compared to $-M$, which could be caused by pinned domains.

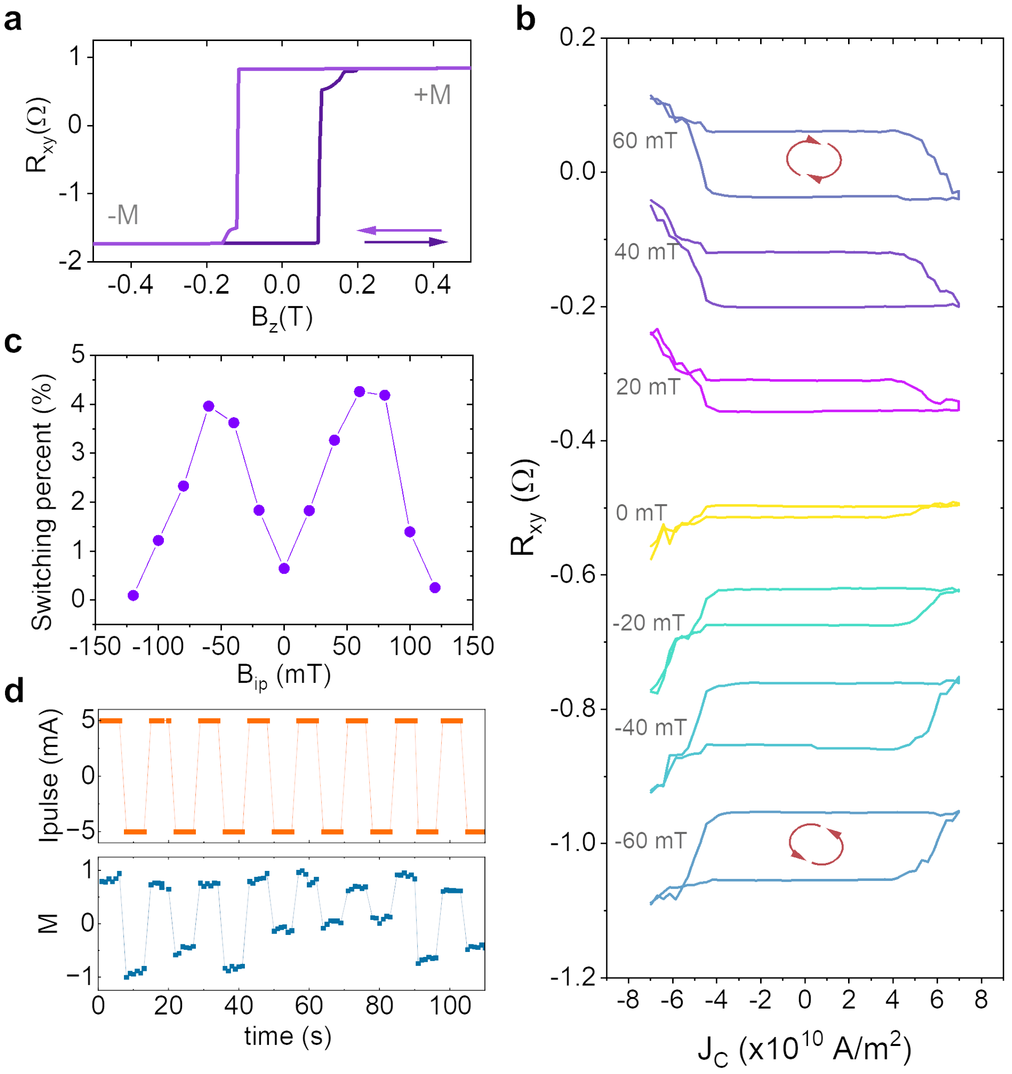

Figure 6.2: Field-assisted deterministic current-induced switching in Fe_3GaTe_2. **a.** Anomalous Hall effect in Device 2 without any background subtraction. **b.** Switching curves at different applied fields showing opposite switching directions for positive and negative assisting in-plane field. **c.** Magnetization switching percentage achieved for Device 2 at different assisting fields. **d.** Time dependence of I_{pulse} (upper panel) and the corresponding transverse resistance normalized to the R_{AHE}. Measurements were performed on Device 3.

6.3 Spin orbit fields in Fe_3GaTe_2 probed by second harmonic technique

Similar to Fe_3GeTe_2, Fe_3GaTe_2 has a hexagonal crystal structure of space group $P63/mmc$. Hence, we expect the effective spin orbit field in Fe_3GaTe_2 to follow the same form as that of Fe_3GeTe_2 [122]:

$$H_{\text{SOT}} = \Gamma_0 \left[(m_x J_x - m_y J_y)\hat{x} - (m_y J_x + m_x J_y)\hat{y} \right] \tag{6.1}$$

where Γ_0 relates to the strength of the SOT, J_x (J_y) is the current density along $x-$ ($y-$) directions, and m_x (m_y) are the magnetization components along the $x-$ ($y-$) directions. The self-generated SOT can then be written as:

$$\tau = -|\gamma| m \times \Gamma_0 \left[(m_x J_x - m_y J_y)\hat{x} - (m_y J_x + m_x J_y)\hat{y} \right] \tag{6.2}$$

where γ is the gyromagnetic ratio. This is quite different from the conventional damping-like ($\tau_{DL} \approx m \times (s \times m)$) and field-like torque ($\tau_{FL} \approx s \times m$) generated in ferromagnet/spin orbit material heterostructures. s is the spin polarization and m is the magnetization vector.

To evaluate the current-induced self-torques in Fe_3GaTe_2 we performed harmonic Hall measurements on Fe_3GaTe_2 Hall bars (Device 1) [181]. The second harmonic Hall component detects the oscillation of the magnetization around its equilibrium position generated by the periodically changing spin-orbit fields due to the applied sinusoidal current. More specifically, we can determine the strength of the self-generated torque by performing angle-dependent and field-dependent measurements.

From field-dependent measurements, we can extract the effective damping-like (H_{DL}) and field-like (H_{FL}) fields using the following expression, valid for $H_x > H_k$ [182]:

$$R_{xy}^{2\omega} = R_{DL} + R_{FL} + R_{thermal} \tag{6.3}$$

with

$$R_{DL} = \frac{R_{\text{AHE}}}{2} \frac{H_{\text{DL}}}{|H_x| - H_k} \tag{6.4}$$

$$R_{FL} = R_{\text{PHE}} \frac{H_{\text{FL}} + H_{\text{Oe}}}{|H_x|} \tag{6.5}$$

$$R_{thermal} = \alpha_{\text{ONE}} |H_x| + R_{\text{ANE+SSE}} \tag{6.6}$$

where H_k is the anisotropy field, H_x is the externally applied magnetic field, H_{oe} is the Oersted field contribution, R_{PHE} is the planar Hall resistance, α_{ONE} is related to the ordinary Nernst effect, and $R_{(ANE+SSE)}$ refers to the anomalous Nernst and spin Seebeck contributions. The two latter components arises from the thermal gradients in the sample.

The inset in Figure 6.3a shows a schematic diagram for the measurement set-up where the applied field is aligned with the current direction along the x-axis. By applying a magnetic field higher than H_k, the magnetization of Fe_3GaTe_2 aligns along the plane. This magnetization oscillates because of the spin orbit torques

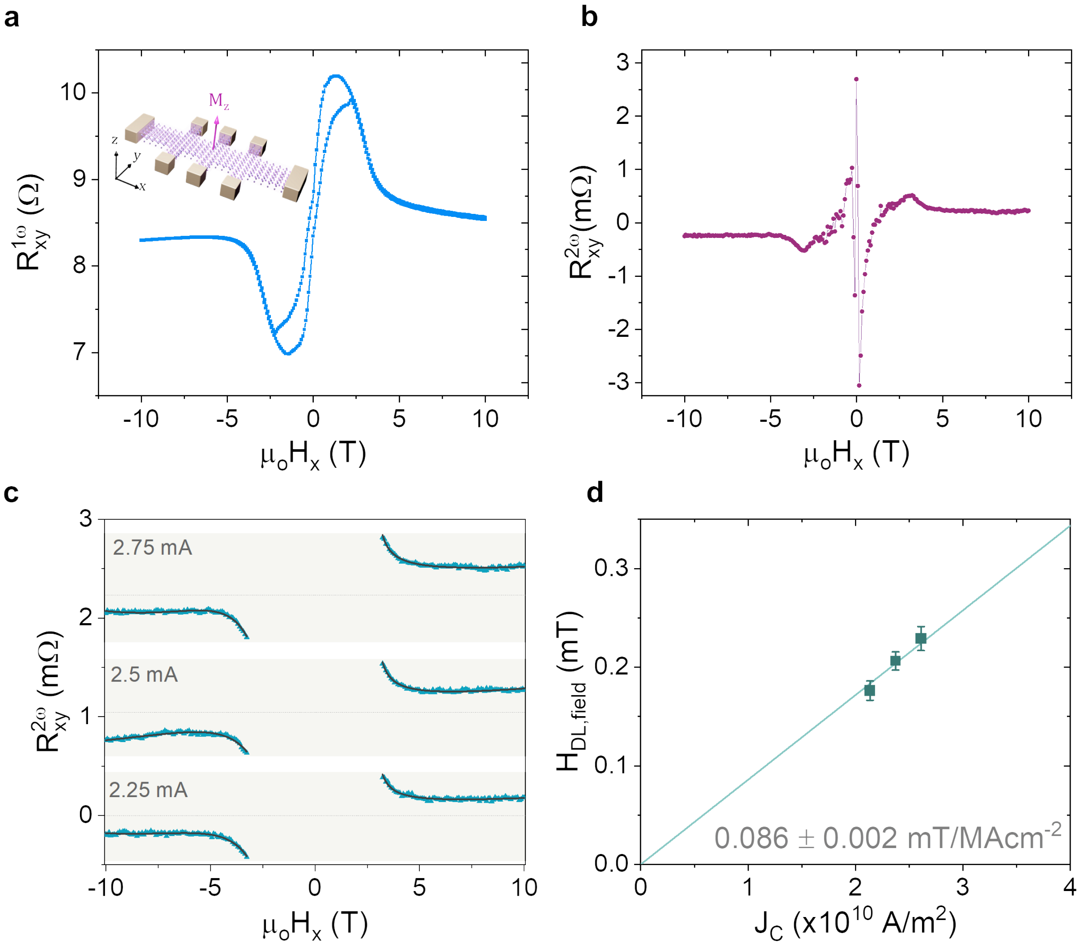

Figure 6.3: Field-dependent harmonic Hall measurements in Device 1. a. In-plane anomalous Hall effect for Fe_3GaTe_2 at room temperature. The inset shows the schematic diagram the Hall bar device. The current direction is along the *x-axis*. **b**. Second harmonic transverse resistance ($R_{xy}^{2\omega}$) as a function of external magnetic field H_x at room temperature, with ac current bias of I_{ac} =2.75 mA. **c**. In-plane magnetic field dependence of $R_{xy}^{2\omega}$ with different applied currents. Solid symbols represent the raw data while the solid lines are the fits to Equation 6.1. **d**. Corresponding effective damping-like field extracted from the field dependence of $R_{xy}^{2\omega}$ shown in **c**.

resulting in the modulation of the second harmonic signal, which eventually saturates at higher in-plane fields.

The first and second harmonic field dependences are shown in Figure 6.3a and b, respectively. From the first harmonic measurements, we extract the anisotropy field of 2.75 T and the in-plane anomalous Hall resistance of 1.55 Ω, which were used to fit the second harmonic signal using Equation 6.3.

Figure 6.3c presents the $R_{xy}^{2\omega}$ vs H_x curves at different currents with the fits to Equation 6.3 showing an increasing magnitude of signal with increasing current. From the raw data, we note that the ONE contribution is negligible. However, a significant ANE contribution can be extracted from the $R_{xy}^{2\omega}$ vs H_x curves where $R_{ANE} = [R^{2\omega}_{xy,sat(+Hx)} - R^{2\omega}_{xy,sat(-Hx)}]/2$ [105]. The R_{ANE} contribution at room temperature increases with the current and ranges from 0.17 to 0.22 mΩ. By extracting the damping-like R_{DL} and field-like R_{FL}components for different currents, allowing us to determine the corresponding effective fields. The damping-like component is two orders of magnitude larger than the extracted field-like component. From the slope of H_{DL} vs.J_c in Figure 6.3d, we extracted the effective damping-like field to be 0.086 mT/(MAcm^{-2}).

Another technique to evaluate the spin orbit torques is by performing angular sweep in the plane of the sample at $H > H_k$ as shown in Figure 6.4a. The first harmonic signal provides information on the planar Hall effect of Fe_3GaTe_2, as shown in Figure 6.4b. The planar Hall effect (PHE) describes the modulation of Hall signal by varying the azimuthal angle between the magnetic field and current. In our case, we determine R_{PHE} to be 11 mΩ, which is two orders of magnitude smaller than the R_{AHE}. This agrees well with the earlier report of PHE in Fe_3GaTe_2 [92].

Moreover, the angular dependence of the second harmonic Hall measurement reveals the damping-like and field-like components since both exhibit different angular symmetries. For $H > H_k$, the second harmonic Hall voltage varies with the angle φ between the current and the in-plane magnetic field direction as follows [183, 184]:

$$V_{xy}^{2\omega} = (V_{DL} + V_{thermal}) \cos\varphi + V_{FL} \cos 2\varphi \cos\varphi \tag{6.7}$$

with $V_{DL} = I_{ac}R_{DL}$, $V_{FL} = I_{ac}R_{FL}$, and $V_{thermal} = I_{ac}R_{thermal}$. The damping-like and thermal components follow a $cos\varphi$, while the field-like component follows $cos2\varphi cos\varphi$ dependence.

Figure 6.4c shows the $V_{xy}^{2\omega}$ vs. φ under different magnetic fields exceeding H_k. Clearly, we observe a dominant damping-like torque contribution given by the cosine dependence of $V_{xy}^{2\omega}$. Moreover, as the external magnetic field increases the second harmonic signal decreases, and gradually saturates at higher fields. This behavior is consistent with the field-dependence data. By fitting the data to Equation 6.7, we find that the field-like component is negligible and not required to describe the data. To extract the effective damping-like field we plot $V^{2\omega}_{xy,DL+thermal}$ as a function of $1/(H_x - H_k)$ for different current densities, as shown in Figure 6.4d. The slope of the linear fit gives effective damping-like field of 0.108 mT/MAcm^{-2} which agrees with the value obtained from the field-dependence data.

The SOT efficiency, ξ_{DL}, at room temperature can then be evaluated using the following equation [181]:

$$\xi_{\mathrm{DL}} = \frac{2e}{\hbar} M_s t_{\mathrm{FM}} \frac{\mu_0 H_{\mathrm{DL}}}{J_c} \tag{6.8}$$

where e is the elementary charge, $\hbar$ is the reduced Planck's constant, M_s =2.2x10^5 A/m[108] is the saturation magnetization of bulk Fe_3GaTe_2, and t_{FM}=62 nm is

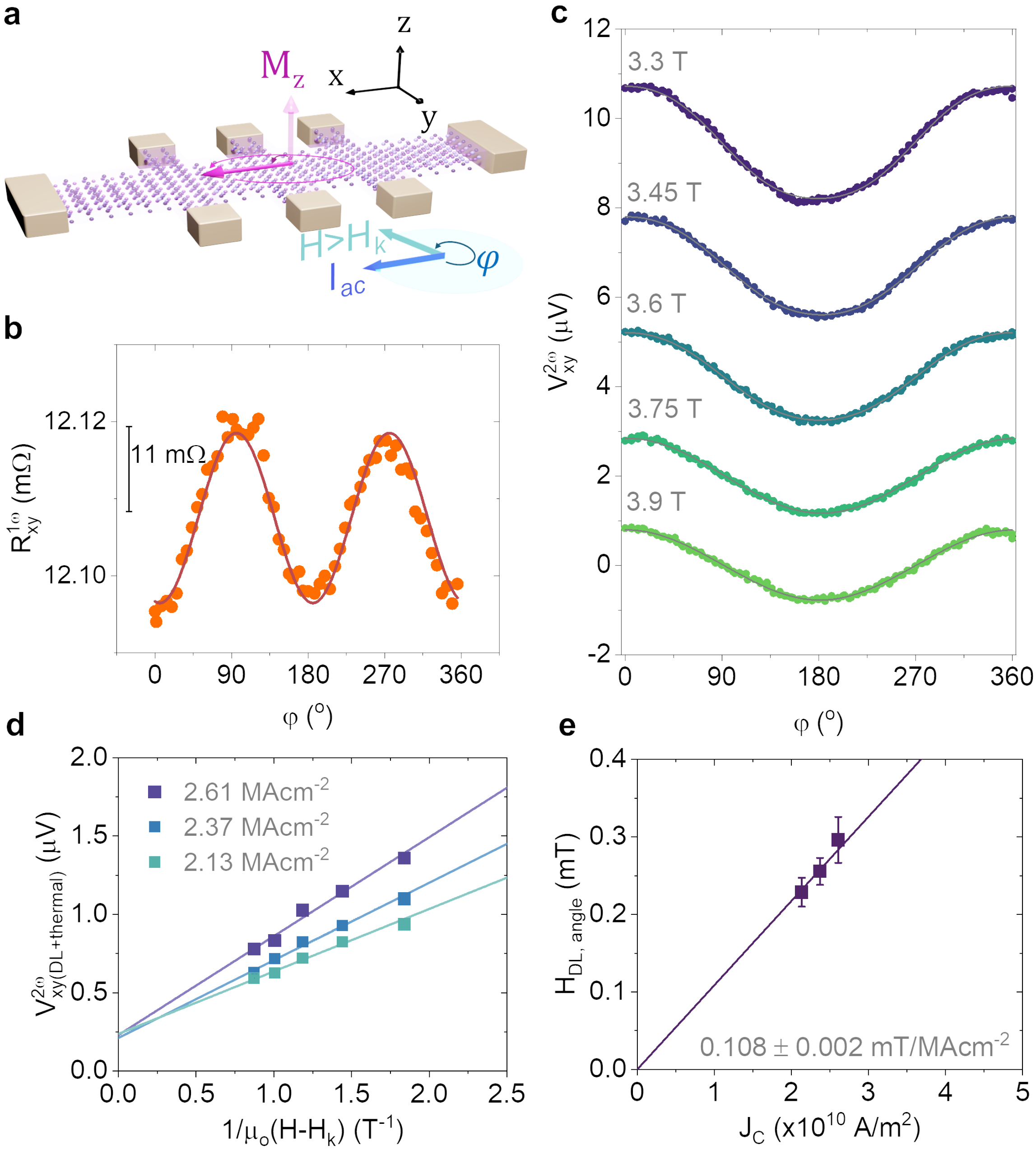

Figure 6.4: Angle-dependent first and second harmonic Hall measurements in Device 1. a. Schematic diagram of angle-dependent harmonic Hall measurements under an external magnetic field. The azimuthal angle φ is measured between the direction of current I_{ac} and applied field H. **b.** Planar Hall resistance ($R^{1\omega}_{xy}$) as a function of φ, with I_{ac} =2.75 mA and H =3.7 T. **c.** Angular dependence of second harmonic Hall voltage $V^{2\omega}_{xy}$ at different magnetic fields with I_{ac}=2.75 mA. The curves are vertically offset for clarity. **d.** Damping-like component $V^{2\omega}_{xy,DL+thermal}$ plotted against $1/\mu_0(H-H_k)$ for different current densities corresponding to I_{ac} =2.25, 2.5, 2.75 mA. **e.** Damping-like field (H_{DL}) as a function of current density, extracted from the linear fits **d**.

the thickness of the ferromagnet. From the field-dependence data, we calculate the SOT efficiency to be 0.356 while the angle-dependence data gives a value of 0.448. These values are comparable to reported values for Fe_3GaTe_2/Pt [110]. We can further calculate the spin Hall conductivity $\sigma_{SHC} = \sigma_C \xi_{DL}$, where σ_C is the charge conductivity. Using σ_C=6.14×10^5 $\Omega^{-1}m^{-1}$ we obtain the σ_{SHC} values of 2.19×10^5 $\hbar/2e$ $\Omega^{-1}m^{-1}$ and 2.75×10^5 $\hbar$/2e $\Omega^{-1}m^{-1}$, from the field- and angle-dependence, respectively.

7 Summary and outlook

Summary

Van der Waals (vdW) magnetic materials have emerged as compelling candidates for investigating spin transport, magnetization dynamics, and proximity effects in two-dimensional (2D) heterostructures. In this thesis, extensive focus was given to Fe_5GeTe_2 (FGT) and its doped variants, $(Co_{0.15}Fe_{0.85})_5GeTe_2$ (CFGT) and $(Ni_{0.4}Fe_{0.6})_5GeTe_2$ (NFGT) due to their high Curie temperatures and tunable magnetic characteristics compatible with graphene-based spintronic architectures.

Broadband ferromagnetic resonance (FMR) measurements conducted at room temperature on FGT, CFGT, and NFGT yielded critical dynamic parameters such as the g-factor, in-plane magnetic anisotropy, effective magnetization, and Gilbert damping constant. Among these, FGT and CFGT exhibited low damping values ($\sim$0.04), favorable for energy efficient and high speed device integration. In contrast, NFGT demonstrated higher effective magnetization and thermal stability, although with slightly increased damping. Deviations in g-factors from the free-electron value across all materials indicated substantial orbital contributions, revealing a pivotal role of spin orbit coupling and crystal symmetry in modulating their dynamic magnetic responses.

The practical implications of these dynamic properties were realized through spin-valve devices constructed from FGT/graphene and CFGT/graphene heterostructures. In FGT-based devices, room-temperature spin injection, transport, and detection were successfully demonstrated, with negative spin polarization (up to P_{ip} =44.9% and P_z =9.5%) observed at the FGT/graphene interface. The presence of multidirectional spin polarization suggested a canted magnetization at the interface, distinct from the bulk behavior of FGT. FGT exhibits strong remanent magnetization and magnetic softness at room temperature, which makes it desirable for field-free spin orbit torque (SOT) applications.

CFGT/graphene devices further confirmed the capability of Co doping to reorient magnetic anisotropy from out-of-plane to in-plane. Negative spin polarization ($\sim$5%) and symmetric Hanle curves validated robust in-plane magnetization and coherent spin transport at the CFGT/graphene interface. These results emphasized the tunability of magnetic anisotropy via site-specific doping, positioning CFGT as a prototype for in-plane vdW ferromagnetic integration in graphene spintronic devices.

Another notable advancement was the realization of spin-texture spin valves using FGT/graphene systems, wherein electrical signals directly reflected the creation and dynamics of non-collinear magnetic textures, such as spin domains and possible skyrmionic states. Devices with notches or constrictions in the FGT layer exhibited multiple switching signatures, which were linked spin texture formation. These spin textures were shown to survive and coexist with conventional single-domain configurations, and their interaction with injected spin currents was electrically detected through spin valve swithcing and Hanle precession in graphene. This strategy opens the door to electrical control and detection of spin textures, offering promising pathways for memory and logic circuits in spintronics.

Complementary to these studies, Fe_3GaTe_2, another Fe-based vdW magnet, with strong PMA and high T_C, displayed robust room temperature spin orbit torque behavior. A large anomalous Hall angle (up to 0.13 at 2 K) and a self-induced damping-like SOT efficiency (0.35-0.44) were observed through harmonic Hall resistance techniques. The spin Hall conductivity (σ_{SHC}) reached values as high as $\sim 2.75 \times 10^5\ \hbar/2e\ (\Omega m)^{-1}$ for 62 nm-thick Fe_3GaTe_2, illustrating its potential as a single layer spin orbit device. The observed partial switching of magnetization using self-torque in combination with in-plane assisting fields further confirmed the viability of this material for SOT-driven magnetization dynamics.

In summary, this dissertation demonstrates how Fe-based vdW magnets serve as robust platforms for studying and utilizing spin transport, spin–orbit interactions, and magnetization dynamics at room temperature. In future, their integration with scalable devices can establish a strong foundation for energy-efficient, ultrafast, and reconfigurable spintronic technologies.

Outlook

Looking ahead, several exciting directions remain open. First, the demonstration of room-temperature spin transport and magnetization dynamics in FGT and its Co/Ni-doped variants offers great relevance for practical applications in on-chip non-volatile memory, magnetic logic gates, and spin-based interconnects in low-power electronics. Future efforts could focus on improving interface quality and scaling down devices without sacrificing performance. Second, magnetic anisotropy and magnetodynamic parameter engineering through site-specific doping, as demonstrated in CFGT and NFGT, opens new opportunities for materials design. This enables the exploration of alternative dopants and compositional gradients that targets to achieve key figures of merit for specific device applications.

The all-electrical detection of nontrivial spin textures in FGT/graphene spin valves could be utilized for further development of topologically robust spin memories and logic circuits, or for multilevel spin memory and logic devices.

Further exploration of interfacial effects in hybrid vdW heterostructures and twist angle dependent phenomena could unlock even more complex spin configurations and exotic transport signatures. These effects can induce novel phenomena like reconfigurable magnetic states, moiré-induced exchange fields, valley-dependent spin transport or spin filtering, with implications for quantum spin logic and neuromorphic computing platforms.

In addition to the exciting physics, to transition from laboratory proof-of-concept to commercial relevance, vdW magnets must overcome challenges in ambient stability, wafer-scale synthesis, and contact resistance engineering. Improvements in CVD growth, and encapsulation techniques will be crucial for enabling industry-compatible devices.

References

[1] I. Žutić, J. Fabian, and S. Das Sarma, “Spintronics: Fundamentals and applications”, Reviews of Modern Physics **76**, 323–410 (2004).

[2] M. N. Baibich, J. M. Broto, A. Fert, F. N. Van Dau, F. Petroff, P. Etienne, G. Creuzet, A. Friederich, and J. Chazelas, “Giant Magnetoresistance of (001)Fe/(001)Cr Magnetic Superlattices”, en, Physical Review Letters **61**, 2472–2475 (1988).

[3] G. Binasch, P. Grünberg, F. Saurenbach, and W. Zinn, “Enhanced magnetoresistance in layered magnetic structures with antiferromagnetic interlayer exchange”, en, Physical Review B **39**, 4828–4830 (1989).

[4] M. Julliere, “Tunneling between ferromagnetic films”, en, Physics Letters A **54**, 225–226 (1975).

[5] J. S. Moodera, L. R. Kinder, T. M. Wong, and R. Meservey, “Large Magnetoresistance at Room Temperature in Ferromagnetic Thin Film Tunnel Junctions”, en, Physical Review Letters **74**, 3273–3276 (1995).

[6] J. Slonczewski, “Current-driven excitation of magnetic multilayers”, en, Journal of Magnetism and Magnetic Materials **159**, L1–L7 (1996).

[7] M. Tsoi, A. G. M. Jansen, J. Bass, W.-C. Chiang, M. Seck, V. Tsoi, and P. Wyder, “Excitation of a Magnetic Multilayer by an Electric Current”, en, Physical Review Letters **80**, 4281–4284 (1998).

[8] Y. Huai, F. Albert, P. Nguyen, M. Pakala, and T. Valet, “Observation of spin-transfer switching in deep submicron-sized and low-resistance magnetic tunnel junctions”, en, Applied Physics Letters **84**, 3118–3120 (2004).

[9] G. D. Fuchs, N. C. Emley, I. N. Krivorotov, P. M. Braganca, E. M. Ryan, S. I. Kiselev, J. C. Sankey, D. C. Ralph, R. A. Buhrman, and J. A. Katine, “Spin-transfer effects in nanoscale magnetic tunnel junctions”, en, Applied Physics Letters **85**, 1205–1207 (2004).

[10] L. Liu, C.-F. Pai, Y. Li, H. W. Tseng, D. C. Ralph, and R. A. Buhrman, “Spin-Torque Switching with the Giant Spin Hall Effect of Tantalum”, en, Science **336**, 555–558 (2012).

[11] I. M. Miron, K. Garello, G. Gaudin, P.-J. Zermatten, M. V. Costache, S. Auffret, S. Bandiera, B. Rodmacq, A. Schuhl, and P. Gambardella, “Perpendicular switching of a single ferromagnetic layer induced by in-plane current injection”, en, Nature **476**, 189–193 (2011).

[12] S. S. P. Parkin, M. Hayashi, and L. Thomas, “Magnetic Domain-Wall Racetrack Memory”, Science **320**, 190–194 (2008).

[13] B. Behin-Aein, D. Datta, S. Salahuddin, and S. Datta, “Proposal for an all-spin logic device with built-in memory”, en, Nature Nanotechnology **5**, 266–270 (2010).

[14] A. V. Chumak, V. I. Vasyuchka, A. A. Serga, and B. Hillebrands, “Magnon spintronics”, en, Nature Physics **11**, 453–461 (2015).

[15] K. S. Novoselov, A. K. Geim, S. V. Morozov, D. Jiang, Y. Zhang, S. V. Dubonos, I. V. Grigorieva, and A. A. Firsov, “Electric Field Effect in Atomically Thin Carbon Films”, en, Science **306**, 666–669 (2004).

[16] N. D. Mermin and H. Wagner, “Absence of Ferromagnetism or Antiferromagnetism in One- or Two-Dimensional Isotropic Heisenberg Models”, en, Physical Review Letters **17**, 1133–1136 (1966).

[17] B. Huang, G. Clark, E. Navarro-Moratalla, D. R. Klein, R. Cheng, K. L. Seyler, D. Zhong, E. Schmidgall, M. A. McGuire, D. H. Cobden, W. Yao, D. Xiao, P. Jarillo-Herrero, and X. Xu, “Layer-dependent ferromagnetism in a van der Waals crystal down to the monolayer limit”, en, Nature **546**, 270–273 (2017).

[18] C. Gong, L. Li, Z. Li, H. Ji, A. Stern, Y. Xia, T. Cao, W. Bao, C. Wang, Y. Wang, Z. Q. Qiu, R. J. Cava, S. G. Louie, J. Xia, and X. Zhang, “Discovery of intrinsic ferromagnetism in two-dimensional van der Waals crystals”, en, Nature **546**, 265–269 (2017).

[19] K. S. Burch, D. Mandrus, and J.-G. Park, “Magnetism in two-dimensional van der Waals materials”, en, Nature **563**, 47–52 (2018).

[20] C. Gong and X. Zhang, “Two-dimensional magnetic crystals and emergent heterostructure devices”, en, Science **363**, eaav4450 (2019).

[21] H. Li, S. Ruan, and Y.-J. Zeng, “Intrinsic Van Der Waals Magnetic Materials from Bulk to the 2D Limit: New Frontiers of Spintronics”, en, Advanced Materials **31**, 1900065 (2019).

[22] Z. Fei, B. Huang, P. Malinowski, W. Wang, T. Song, J. Sanchez, W. Yao, D. Xiao, X. Zhu, A. F. May, W. Wu, D. H. Cobden, J.-H. Chu, and X. Xu, “Two-dimensional itinerant ferromagnetism in atomically thin Fe3GeTe2”, en, Nature Materials **17**, 778–782 (2018).

[23] T. Kong, K. Stolze, E. I. Timmons, J. Tao, D. Ni, S. Guo, Z. Yang, R. Prozorov, and R. J. Cava, “VI_3 —a New Layered Ferromagnetic Semiconductor”, en, Advanced Materials **31**, 1808074 (2019).

[24] G. Long, H. Henck, M. Gibertini, D. Dumcenco, Z. Wang, T. Taniguchi, K. Watanabe, E. Giannini, and A. F. Morpurgo, “Persistence of Magnetism in Atomically Thin $MnPS_3$ Crystals”, en, Nano Letters **20**, 2452–2459 (2020).

[25] Y. Deng, Y. Yu, M. Z. Shi, Z. Guo, Z. Xu, J. Wang, X. H. Chen, and Y. Zhang, “Quantum anomalous Hall effect in intrinsic magnetic topological insulator $\mathrm{MnBi_2\ Te_4}$”, en, Science **367**, 895–900 (2020).

[26] T. Song, X. Cai, M. W.-Y. Tu, X. Zhang, B. Huang, N. P. Wilson, K. L. Seyler, L. Zhu, T. Taniguchi, K. Watanabe, M. A. McGuire, D. H. Cobden, D. Xiao, W. Yao, and X. Xu, “Giant tunneling magnetoresistance in spin-filter van der Waals heterostructures”, Science **360**, 1214–1218 (2018).

[27] T. Song, Z. Fei, M. Yankowitz, Z. Lin, Q. Jiang, K. Hwangbo, Q. Zhang, B. Sun, T. Taniguchi, K. Watanabe, M. A. McGuire, D. Graf, T. Cao, J.-H. Chu, D. H. Cobden, C. R. Dean, D. Xiao, and X. Xu, “Switching 2D magnetic states via pressure tuning of layer stacking”, en, Nature Materials **18**, 1298–1302 (2019).

[28] T. Li, S. Jiang, N. Sivadas, Z. Wang, Y. Xu, D. Weber, J. E. Goldberger, K. Watanabe, T. Taniguchi, C. J. Fennie, K. Fai Mak, and J. Shan, “Pressure-controlled interlayer magnetism in atomically thin CrI3”, en, Nature Materials **18**, 1303–1308 (2019).

[29] Y. Deng, Y. Yu, Y. Song, J. Zhang, N. Z. Wang, Z. Sun, Y. Yi, Y. Z. Wu, S. Wu, J. Zhu, J. Wang, X. H. Chen, and Y. Zhang, “Gate-tunable room-temperature ferromagnetism in two-dimensional Fe3GeTe2”, en, Nature **563**, 94–99 (2018).

[30] F. Wu, M. Gibertini, K. Watanabe, T. Taniguchi, I. Gutiérrez-Lezama, N. Ubrig, and A. F. Morpurgo, “Gate-Controlled Magnetotransport and Electrostatic Modulation of Magnetism in 2D Magnetic Semiconductor CrPS4”, en, Advanced Materials **35**, 2211653 (2023).

[31] S. Jiang, L. Li, Z. Wang, K. F. Mak, and J. Shan, “Controlling magnetism in 2D CrI3 by electrostatic doping”, en, Nature Nanotechnology **13**, 549–553 (2018).

[32] D. Zhong, K. L. Seyler, X. Linpeng, R. Cheng, N. Sivadas, B. Huang, E. Schmidgall, T. Taniguchi, K. Watanabe, M. A. McGuire, W. Yao, D. Xiao, K.-M. C. Fu, and X. Xu, “Van der Waals engineering of ferromagnetic semiconductor heterostructures for spin and valleytronics”, Science Advances **3**, e1603113 (2017).

[33] M. Kim, P. Kumaravadivel, J. Birkbeck, W. Kuang, S. G. Xu, D. G. Hopkinson, J. Knolle, P. A. McClarty, A. I. Berdyugin, M. Ben Shalom, R. V. Gorbachev, S. J. Haigh, S. Liu, J. H. Edgar, K. S. Novoselov, I. V. Grigorieva, and A. K. Geim, “Micromagnetometry of two-dimensional ferromagnets”, en, Nature Electronics **2**, 457–463 (2019).

[34] H. Wang, Y. Liu, P. Wu, W. Hou, Y. Jiang, X. Li, C. Pandey, D. Chen, Q. Yang, H. Wang, D. Wei, N. Lei, W. Kang, L. Wen, T. Nie, W. Zhao, and K. L. Wang, "Above Room-Temperature Ferromagnetism in Wafer-Scale Two-Dimensional van der Waals Fe3GeTe2 Tailored by a Topological Insulator", ACS Nano **14**, 10045–10053 (2020).

[35] Q. L. He et al., "Tailoring exchange couplings in magnetic topological-insulator/antiferromagnet heterostructures", en, Nature Materials **16**, 94–100 (2017).

[36] S. Kezilebieke, M. N. Huda, V. Vaňo, M. Aapro, S. C. Ganguli, O. J. Silveira, S. Głodzik, A. S. Foster, T. Ojanen, and P. Liljeroth, "Topological superconductivity in a van der Waals heterostructure", en, Nature **588**, 424–428 (2020).

[37] L. Ai, E. Zhang, J. Yang, X. Xie, Y. Yang, Z. Jia, Y. Zhang, S. Liu, Z. Li, P. Leng, X. Cao, X. Sun, T. Zhang, X. Kou, Z. Han, F. Xiu, and S. Dong, "Van der Waals ferromagnetic Josephson junctions", en, Nature Communications **12**, 6580 (2021).

[38] T. S. Ghiasi, D. Petrosyan, J. Ingla-Aynés, T. Bras, K. Watanabe, T. Taniguchi, S. Mañas-Valero, E. Coronado, K. Zollner, J. Fabian, P. Kim, and H. S. J. van der Zant, "Quantum spin Hall effect in magnetic graphene", en, Nature Communications **16**, 5336 (2025).

[39] A. J. Freeman and R. E. Watson, "Theory of Direct Exchange in Ferromagnetism", Physical Review **124**, 1439–1454 (1961).

[40] P. W. Anderson, "Antiferromagnetism. Theory of Superexchange Interaction", en, Physical Review **79**, 350–356 (1950).

[41] M. A. Ruderman and C. Kittel, "Indirect Exchange Coupling of Nuclear Magnetic Moments by Conduction Electrons", Physical Review **96**, 99–102 (1954).

[42] T. Kasuya, "A Theory of Metallic Ferro- and Antiferromagnetism on Zener's Model", Progress of Theoretical Physics **16**, 45–57 (1956).

[43] K. Yosida, "Magnetic Properties of Cu-Mn Alloys", Physical Review **106**, 893–898 (1957).

[44] B. Heinrich and J. Cochran, "Ultrathin metallic magnetic films: magnetic anisotropies and exchange interactions", en, Advances in Physics **42**, 523–639 (1993).

[45] H. J. Elmers, J. Hauschild, H. Fritzsche, G. Liu, U. Gradmann, and U. Köhler, "Magnetic Frustration in Ultrathin Fe Films", Physical Review Letters **75**, 2031–2034 (1995).

[46] C. A. F. Vaz, J. A. C. Bland, and G. Lauhoff, "Magnetism in ultrathin film structures", Reports on Progress in Physics **71** (2008).

[47] G. Zhang, F. Guo, H. Wu, X. Wen, L. Yang, W. Jin, W. Zhang, and H. Chang, “Above-room-temperature strong intrinsic ferromagnetism in 2D van der Waals Fe3GaTe2 with large perpendicular magnetic anisotropy”, en, Nature Communications **13**, 5067 (2022).

[48] J.-U. Lee, S. Lee, J. H. Ryoo, S. Kang, T. Y. Kim, P. Kim, C.-H. Park, J.-G. Park, and H. Cheong, “Ising-Type Magnetic Ordering in Atomically Thin FePS3”, Nano Letters **16**, 7433–7438 (2016).

[49] A. Wiedenmann, J. Rossat-Mignod, A. Louisy, R. Brec, and J. Rouxel, “Neutron diffraction study of the layered compounds MnPSe3 and FePSe3”, Solid State Communications **40**, 1067–1072 (1981).

[50] E. Morosan, H. W. Zandbergen, L. Li, M. Lee, J. G. Checkelsky, M. Heinrich, T. Siegrist, N. P. Ong, and R. J. Cava, “Sharp switching of the magnetization in Fe0.25TaS2”, Physical Review B **75**, 104401 (2007).

[51] A. F. May, D. Ovchinnikov, Q. Zheng, R. Hermann, S. Calder, B. Huang, Z. Fei, Y. Liu, X. Xu, and M. A. McGuire, “Ferromagnetism Near Room Temperature in the Cleavable van der Waals Crystal Fe5GeTe2”, ACS Nano **13**, 4436–4442 (2019).

[52] X. Chen, Y.-T. Shao, R. Chen, S. Susarla, T. Hogan, Y. He, H. Zhang, S. Wang, J. Yao, P. Ercius, D. A. Muller, R. Ramesh, and R. J. Birgeneau, “Pervasive beyond Room-Temperature Ferromagnetism in a Doped van der Waals Magnet”, Physical Review Letters **128**, 217203 (2022).

[53] A. F. May, M.-H. Du, V. R. Cooper, and M. A. McGuire, “Tuning magnetic order in the van der Waals metal Fe5GeTe2 by cobalt substitution”, Physical Review Materials **4**, 074008 (2020).

[54] J. Seo et al., “Nearly room temperature ferromagnetism in a magnetic metal-rich van der Waals metal”, Science Advances **6**, eaay8912 (2020).

[55] W. Chen, Z. Sun, Z. Wang, L. Gu, X. Xu, S. Wu, and C. Gao, “Direct observation of van der Waals stacking–dependent interlayer magnetism”, Science **366**, 983–987 (2019).

[56] Y. Zhong, C. Peng, H. Huang, D. Guan, J. Hwang, K. H. Hsu, Y. Hu, C. Jia, B. Moritz, D. Lu, J.-S. Lee, J.-F. Jia, T. P. Devereaux, S.-K. Mo, and Z.-X. Shen, “From Stoner to local moment magnetism in atomically thin Cr2Te3”, en, Nature Communications **14**, 5340 (2023).

[57] X. Sun et al., “Room temperature ferromagnetism in ultra-thin van der Waals crystals of 1T-CrTe2”, en, Nano Research **13**, 3358–3363 (2020).

[58] X. Cai, T. Song, N. P. Wilson, G. Clark, M. He, X. Zhang, T. Taniguchi, K. Watanabe, W. Yao, D. Xiao, M. A. McGuire, D. H. Cobden, and X. Xu, “Atomically Thin CrCl3: An In-Plane Layered Antiferromagnetic Insulator”, Nano Letters **19**, 3993–3998 (2019).

[59] M.-W. Lin, H. L. Zhuang, J. Yan, T. Z. Ward, A. A. Puretzky, C. M. Rouleau, Z. Gai, L. Liang, V. Meunier, B. G. Sumpter, P. Ganesh, P. R. C. Kent, D. B. Geohegan, D. G. Mandrus, and K. Xiao, “Ultrathin nanosheets of CrSiTe3: a semiconducting two-dimensional ferromagnetic material”, en, Journal of Materials Chemistry C **4**, 315–322 (2015).

[60] Y. Zhang, J. Chu, L. Yin, T. A. Shifa, Z. Cheng, R. Cheng, F. Wang, Y. Wen, X. Zhan, Z. Wang, and J. He, “Ultrathin Magnetic 2D Single-Crystal CrSe”, en, Advanced Materials **31**, 1900056 (2019).

[61] Y. Wang, S. Kajihara, H. Matsuoka, B. K. Saika, K. Yamagami, Y. Takeda, H. Wadati, K. Ishizaka, Y. Iwasa, and M. Nakano, “Layer-Number-Independent Two-Dimensional Ferromagnetism in Cr3Te4”, Nano Letters **22**, 9964–9971 (2022).

[62] L.-Z. Zhang, A.-L. Zhang, X.-D. He, X.-W. Ben, Q.-L. Xiao, W.-L. Lu, F. Chen, Z. Feng, S. Cao, J. Zhang, and J.-Y. Ge, “Critical behavior and magnetocaloric effect of the quasi-two-dimensional room-temperature ferromagnet $\mathrm{Cr}{}_{4}\mathrm{Te}{}_{5}$”, Physical Review B **101**, 214413 (2020).

[63] Y. Liu, M. Abeykoon, E. Stavitski, K. Attenkofer, and C. Petrovic, “Magnetic anisotropy and entropy change in trigonal Cr5Te8”, Physical Review B **100**, 245114 (2019).

[64] J. Son, S. Son, P. Park, M. Kim, Z. Tao, J. Oh, T. Lee, S. Lee, J. Kim, K. Zhang, K. Cho, T. Kamiyama, J. H. Lee, K. F. Mak, J. Shan, M. Kim, J.-G. Park, and J. Lee, “Air-Stable and Layer-Dependent Ferromagnetism in Atomically Thin van der Waals CrPS4”, ACS Nano **15**, 16904–16912 (2021).

[65] M. A. McGuire, V. O. Garlea, S. KC, V. R. Cooper, J. Yan, H. Cao, and B. C. Sales, “Antiferromagnetism in the van der Waals layered spin-lozenge semiconductor CrTe3”, Physical Review B **95**, 144421 (2017).

[66] T. Zhang, Y. Wang, H. Li, F. Zhong, J. Shi, M. Wu, Z. Sun, W. Shen, B. Wei, W. Hu, X. Liu, L. Huang, C. Hu, Z. Wang, C. Jiang, S. Yang, Q.-m. Zhang, and Z. Qu, “Magnetism and Optical Anisotropy in van der Waals Antiferromagnetic Insulator CrOCl”, ACS Nano **13**, 11353–11362 (2019).

[67] P. Liu, Z. Xu, H. Huang, J. Li, C. Feng, M. Huang, M. Zhu, Z. Wang, Z. Zhang, D. Hou, Y. Lu, and B. Xiang, “Exploring the magnetic ordering in atomically thin antiferromagnetic MnPSe3 by Raman spectroscopy”, Journal of Alloys and Compounds **828**, 154432 (2020).

[68] G. Long, T. Zhang, X. Cai, J. Hu, C.-w. Cho, S. Xu, J. Shen, Z. Wu, T. Han, J. Lin, J. Wang, Y. Cai, R. Lortz, Z. Mao, and N. Wang, “Isolation and Characterization of Few-Layer Manganese Thiophosphite”, ACS Nano **11**, 11330–11336 (2017).

[69] D. J. O'Hara, T. Zhu, A. H. Trout, A. S. Ahmed, Y. K. Luo, C. H. Lee, M. R. Brenner, S. Rajan, J. A. Gupta, D. W. McComb, and R. K. Kawakami, "Room Temperature Intrinsic Ferromagnetism in Epitaxial Manganese Selenide Films in the Monolayer Limit", Nano Letters **18**, 3125–3131 (2018).

[70] R. Basnet, K. M. Kotur, M. Rybak, C. Stephenson, S. Bishop, C. Autieri, M. Birowska, and J. Hu, "Controlling magnetic exchange and anisotropy by nonmagnetic ligand substitution in layered M P X 3 (M = Ni , Mn; X = S , Se)", en, Physical Review Research **4**, 023256 (2022).

[71] K. Kim, S. Y. Lim, J.-U. Lee, S. Lee, T. Y. Kim, K. Park, G. S. Jeon, C.-H. Park, J.-G. Park, and H. Cheong, "Suppression of magnetic ordering in XXZ-type antiferromagnetic monolayer NiPS3", en, Nature Communications **10**, 345 (2019).

[72] X. Wang, D. Li, Z. Li, C. Wu, C.-M. Che, G. Chen, and X. Cui, "Ferromagnetism in 2D Vanadium Diselenide", ACS Nano **15**, 16236–16241 (2021).

[73] S. Son, M. J. Coak, N. Lee, J. Kim, T. Y. Kim, H. Hamidov, H. Cho, C. Liu, D. M. Jarvis, P. A. C. Brown, J. H. Kim, C.-H. Park, D. I. Khomskii, S. S. Saxena, and J.-G. Park, "Bulk properties of the van der Waals hard ferromagnet VI3", Physical Review B **99**, 041402 (2019).

[74] M. Nakano, Y. Wang, S. Yoshida, H. Matsuoka, Y. Majima, K. Ikeda, Y. Hirata, Y. Takeda, H. Wadati, Y. Kohama, Y. Ohigashi, M. Sakano, K. Ishizaka, and Y. Iwasa, "Intrinsic 2D Ferromagnetism in V5Se8 Epitaxial Thin Films", Nano Letters **19**, Publisher: American Chemical Society, 8806–8810 (2019).

[75] S. Lei, J. Lin, Y. Jia, M. Gray, A. Topp, G. Farahi, S. Klemenz, T. Gao, F. Rodolakis, J. L. McChesney, C. R. Ast, A. Yazdani, K. S. Burch, S. Wu, N. P. Ong, and L. M. Schoop, "High mobility in a van der Waals layered antiferromagnetic metal", Science Advances **6**, eaay6407 (2020).

[76] J. L. Lado and J. Fernadez-Rossier, "On the origin of magnetic anisotropy in two dimensional CrI3", 2D Materials **4** (2017).

[77] B. Huang, G. Clark, D. R. Klein, D. MacNeill, E. Navarro-Moratalla, K. L. Seyler, N. Wilson, M. A. McGuire, D. H. Cobden, D. Xiao, W. Yao, P. Jarillo-Herrero, and X. Xu, "Electrical control of 2D magnetism in bilayer CrI3", en, Nature Nanotechnology **13**, 544–548 (2018).

[78] C. Lei, B. L. Chittari, K. Nomura, N. Banerjee, J. Jung, and A. H. MacDonald, "Magnetoelectric Response of Antiferromagnetic $\mathrm{CrI_3}$ Bilayers", en, Nano Letters **21**, 1948–1954 (2021).

[79] Z. Wang, D. Sapkota, T. Taniguchi, K. Watanabe, D. Mandrus, and A. F. Morpurgo, "Tunneling Spin Valves Based on Fe3GeTe2/hBN/Fe3GeTe2 van der Waals Heterostructures", Nano Letters **18**, 4303–4308 (2018).

[80] H. Pan, C. Zhang, J. Shi, X. Hu, N. Wang, L. An, R. Duan, P. Deb, Z. Liu, and W. Gao, “Room-Temperature Lateral Spin Valve in Graphene/Fe3GaTe2 van der Waals Heterostructures”, ACS Materials Letters **5**, 2226–2232 (2023).

[81] B. Zhao, R. Ngaloy, S. Ghosh, S. Ershadrad, R. Gupta, K. Ali, A. M. Hoque, B. Karpiak, D. Khokhriakov, C. Polley, B. Thiagarajan, A. Kalaboukhov, P. Svedlindh, B. Sanyal, and S. P. Dash, “A Room-Temperature Spin-Valve with van der Waals Ferromagnet Fe5GeTe2/Graphene Heterostructure”, en, Advanced Materials **35**, 2209113 (2023).

[82] X. He, C. Zhang, D. Zheng, P. Li, J. Q. Xiao, and X. Zhang, “Nonlocal Spin Valves Based on Graphene/Fe3GeTe2 van der Waals Heterostructures”, ACS Applied Materials & Interfaces **15**, 9649–9655 (2023).

[83] R. Ngaloy, B. Zhao, S. Ershadrad, R. Gupta, M. Davoudiniya, L. Bainsla, L. Sjöström, M. A. Hoque, A. Kalaboukhov, P. Svedlindh, B. Sanyal, and S. P. Dash, “Strong In-Plane Magnetization and Spin Polarization in ($Co_{0.15}$ $Fe_{0.85}$ $)_5$ $GeTe_2$ /Graphene van der Waals Heterostructure Spin-Valve at Room Temperature”, en, ACS Nano, acsnano.3c07462 (2024).

[84] X. Zeng, L. Zhang, Y. Zhang, F. Yang, L. Zhou, Y. Wang, C. Fang, X. Li, S. Zheng, Y. Liu, Y. Liu, X. Wang, Y. Hao, and G. Han, “Spin valve effect in the van der Waals heterojunction of Fe3GeTe2/tellurene/Fe3GeTe2”, en, Applied Physics Letters **125**, `10.1063/5.0215304` (2024).

[85] K.-H. Min, D. H. Lee, S.-J. Choi, I.-H. Lee, J. Seo, D. W. Kim, K.-T. Ko, K. Watanabe, T. Taniguchi, D. H. Ha, C. Kim, J. H. Shim, J. Eom, J. S. Kim, and S. Jung, “Tunable spin injection and detection across a van der Waals interface”, en, Nature Materials **21**, 1144–1149 (2022).

[86] W. Zhu, Y. Zhu, T. Zhou, X. Zhang, H. Lin, Q. Cui, F. Yan, Z. Wang, Y. Deng, H. Yang, L. Zhao, I. Žutić, K. D. Belashchenko, and K. Wang, “Large and tunable magnetoresistance in van der Waals ferromagnet/semiconductor junctions”, en, Nature Communications **14**, 5371 (2023).

[87] H. Lin, F. Yan, C. Hu, Q. Lv, W. Zhu, Z. Wang, Z. Wei, K. Chang, and K. Wang, “Spin-Valve Effect in Fe3GeTe2/MoS2/Fe3GeTe2 van der Waals Heterostructures”, ACS Applied Materials & Interfaces **12**, 43921–43926 (2020).

[88] W. Zhu, H. Lin, F. Yan, C. Hu, Z. Wang, L. Zhao, Y. Deng, Z. R. Kudrynskyi, T. Zhou, Z. D. Kovalyuk, Y. Zheng, A. Patanè, I. Žutić, S. Li, H. Zheng, and K. Wang, “Large Tunneling Magnetoresistance in van der Waals Ferromagnet/Semiconductor Heterojunctions”, en, Advanced Materials **33**, 2104658 (2021).

[89] Y. Zheng, X. Ma, F. Yan, H. Lin, W. Zhu, Y. Ji, R. Wang, and K. Wang, “Spin filtering effect in all-van der Waals heterostructures with WSe2 barriers”, en, npj 2D Materials and Applications **6**, 62 (2022).

[90] W. Zhu, S. Xie, H. Lin, G. Zhang, H. Wu, T. Hu, Z. Wang, X. Zhang, J. Xu, and Y. Wang, “Zhu, (2022)Large Room-Temperature Magnetoresistance in van der Waals Ferromagnet/Semiconductor Junctions”, Chinese Physics Letters **39** (2022).

[91] L. Pandey, B. Zhao, K. Tenzin, R. Ngaloy, V. Lamparská, H. Bangar, A. Ali, M. Abdel-Hafiez, G. Zhang, H. Wu, H. Chang, L. Sjöström, P. Rout, J. Sławińska, and S. P. Dash, *Energy-efficient field-free unconventional spin-orbit torque magnetization switching dynamics in van der Waals heterostructures*, Feb. 2025.

[92] H. Zhang, X. Chen, T. Wang, X. Huang, X. Chen, Y.-T. Shao, F. Meng, P. Meisenheimer, A. N’Diaye, C. Klewe, P. Shafer, H. Pan, Y. Jia, M. F. Crommie, L. W. Martin, J. Yao, Z. Qiu, D. A. Muller, R. J. Birgeneau, and R. Ramesh, “Room-Temperature, Current-Induced Magnetization Self-Switching in A Van Der Waals Ferromagnet”, en, Advanced Materials **36**, 2308555 (2024).

[93] S. Albarakati, C. Tan, Z.-J. Chen, J. G. Partridge, G. Zheng, L. Farrar, E. L. H. Mayes, M. R. Field, C. Lee, Y. Wang, Y. Xiong, M. Tian, F. Xiang, A. R. Hamilton, O. A. Tretiakov, D. Culcer, Y.-J. Zhao, and L. Wang, “Antisymmetric magnetoresistance in van der Waals Fe3GeTe2/graphite/Fe3GeTe2 trilayer heterostructures”, Science Advances **5**, eaaw0409 (2019).

[94] D. R. Klein, D. MacNeill, J. L. Lado, D. Soriano, E. Navarro-Moratalla, K. Watanabe, T. Taniguchi, S. Manni, P. Canfield, J. Fernández-Rossier, and P. Jarillo-Herrero, “Probing magnetism in 2D van der Waals crystalline insulators via electron tunneling”, Science **360**, 1218–1222 (2018).

[95] V. Gupta, T. M. Cham, G. M. Stiehl, A. Bose, J. A. Mittelstaedt, K. Kang, S. Jiang, K. F. Mak, J. Shan, R. A. Buhrman, and D. C. Ralph, “Manipulation of the van der Waals Magnet Cr2Ge2Te6 by Spin–Orbit Torques”, Nano Letters **20**, 7482–7488 (2020).

[96] V. Ostwal, T. Shen, and J. Appenzeller, “Efficient Spin-Orbit Torque Switching of the Semiconducting Van Der Waals Ferromagnet Cr2Ge2Te6”, en, Advanced Materials **32**, 1906021 (2020).

[97] M. Lohmann, D. Wickramaratne, J. Moon, M. Noyan, H.-J. Chuang, B. T. Jonker, and C. H. Li, “Highly Efficient Spin–Orbit Torque Switching in Bi_2 Se_3 /Fe_3 $GeTe_2$ van der Waals Heterostructures”, en, ACS Nano **18**, 680–690 (2024).

[98] G. Shi, F. Wang, Y. Liu, Z. Li, H. R. Tan, D. Yang, A. Soumyanarayanan, and H. Yang, “Field-Free Manipulation of Two-Dimensional Ferromagnet CrTe2 by Spin–Orbit Torques”, Nano Letters **24**, 7302–7310 (2024).

[99] X. Wang et al., “Current-driven magnetization switching in a van der Waals ferromagnet Fe3GeTe2”, en, Science Advances **5** (2019).

[100] I. Shin, W. J. Cho, E.-S. An, S. Park, H.-W. Jeong, S. Jang, W. J. Baek, S. Y. Park, D.-H. Yang, J. H. Seo, G.-Y. Kim, M. N. Ali, S.-Y. Choi, H.-W. Lee, J. S. Kim, S. D. Kim, and G.-H. Lee, “Spin–Orbit Torque Switching in an All-Van der Waals Heterostructure”, en, Advanced Materials **34**, 2101730 (2022).

[101] I.-H. Kao, R. Muzzio, H. Zhang, M. Zhu, J. Gobbo, S. Yuan, D. Weber, R. Rao, J. Li, J. H. Edgar, J. E. Goldberger, J. Yan, D. G. Mandrus, J. Hwang, R. Cheng, J. Katoch, and S. Singh, “Deterministic switching of a perpendicularly polarized magnet using unconventional spin–orbit torques in WTe2”, en, Nature Materials **21**, 1029–1034 (2022).

[102] Y. Ou, W. Yanez, R. Xiao, M. Stanley, S. Ghosh, B. Zheng, W. Jiang, Y.-S. Huang, T. Pillsbury, A. Richardella, C. Liu, T. Low, V. H. Crespi, K. A. Mkhoyan, and N. Samarth, “ZrTe2/CrTe2: an epitaxial van der Waals platform for spintronics”, en, Nature Communications **13**, 2972 (2022).

[103] M. Alghamdi, M. Lohmann, J. Li, P. R. Jothi, Q. Shao, M. Aldosary, T. Su, B. P. T. Fokwa, and J. Shi, “Highly Efficient Spin–Orbit Torque and Switching of Layered Ferromagnet Fe_3 $GeTe_2$”, en, Nano Letters **19**, 4400–4405 (2019).

[104] B. Zhao, L. Pandey, K. Ali, E. Wang, C. M. Polley, B. Thiagarajan, P. Makk, M. H. D. Guimarães, and S. P. Dash, “Field-Free Spin–Orbit Torque Switching of Canted van der Waals Magnets”, ACS Nano **19**, 13817–13824 (2025).

[105] H. Wang, H. Wu, J. Zhang, Y. Liu, D. Chen, C. Pandey, J. Yin, D. Wei, N. Lei, S. Shi, H. Lu, P. Li, A. Fert, K. L. Wang, T. Nie, and W. Zhao, “Room temperature energy-efficient spin-orbit torque switching in two-dimensional van der Waals Fe3GeTe2 induced by topological insulators”, en, Nature Communications **14**, 5173 (2023).

[106] B. Zhao, L. Bainsla, S. Ershadrad, L. Zeng, R. Ngaloy, P. Svedlindh, E. Olsson, B. Sanyal, and S. P. Dash, “Coexisting Non-Trivial Van der Waals Magnetic Orders Enable Field-Free Spin-Orbit Torque Magnetization Dynamics”, en, Advanced Materials **n/a**, 2502822.

[107] Y. Zhang, X. Ren, R. Liu, Z. Chen, X. Wu, J. Pang, W. Wang, G. Lan, K. Watanabe, T. Taniguchi, Y. Shi, G. Yu, and Q. Shao, “Robust Field-Free Switching Using Large Unconventional Spin-Orbit Torque in an All-Van der Waals Heterostructure”, en, Advanced Materials **36**, 2406464 (2024).

[108] W. Li, W. Zhu, G. Zhang, H. Wu, S. Zhu, R. Li, E. Zhang, X. Zhang, Y. Deng, J. Zhang, L. Zhao, H. Chang, and K. Wang, “Room-Temperature van der Waals Ferromagnet Switching by Spin-Orbit Torques”, en, Advanced Materials **35**, 2303688 (2023).

[109] C. Yun, H. Guo, Z. Lin, L. Peng, Z. Liang, M. Meng, B. Zhang, Z. Zhao, L. Wang, Y. Ma, Y. Liu, W. Li, S. Ning, Y. Hou, J. Yang, and Z. Luo, “Efficient current-induced spin torques and field-free magnetization switching in a room-temperature van der Waals magnet”, Science Advances **9**, eadj3955 (2023).

[110] S. N. Kajale, T. Nguyen, C. A. Chao, D. C. Bono, A. Boonkird, M. Li, and D. Sarkar, “Current-induced switching of a van der Waals ferromagnet at room temperature”, en, Nature Communications **15**, 1485 (2024).

[111] S. N. Kajale, T. Nguyen, N. T. Hung, M. Li, and D. Sarkar, “Field-free deterministic switching of all–van der Waals spin-orbit torque system above room temperature”, Science Advances **10**, eadk8669 (2024).

[112] J. M. Slaughter, N. D. Rizzo, J. Janesky, R. Whig, F. B. Mancoff, D. Houssameddine, J. J. Sun, S. Aggarwal, K. Nagel, S. Deshpande, S. M. Alam, T. Andre, and P. LoPresti, “High density ST-MRAM technology (Invited)”, in 2012 International Electron Devices Meeting (Dec. 2012), pp. 29.3.1–29.3.4.

[113] Y. Huai, “Spin-Transfer Torque MRAM (STT-MRAM): Challenges and Prospects”, en, AAPS Bulletin **18** (2008).

[114] M. Cubukcu, O. Boulle, M. Drouard, K. Garello, C. Onur Avci, I. Mihai Miron, J. Langer, B. Ocker, P. Gambardella, and G. Gaudin, “Spin-orbit torque magnetization switching of a three-terminal perpendicular magnetic tunnel junction”, Applied Physics Letters **104**, 042406 (2014).

[115] J. Kim, J. Sinha, M. Hayashi, M. Yamanouchi, S. Fukami, T. Suzuki, S. Mitani, and H. Ohno, “Layer thickness dependence of the current-induced effective field vector in Ta|CoFeB|MgO”, en, Nature Materials **12**, 240–245 (2013).

[116] W. Han, Y. Otani, and S. Maekawa, “Quantum materials for spin and charge conversion”, en, npj Quantum Materials **3**, 27 (2018).

[117] B. Wang, Y. Li, X. Li, C. Mu, J. Xiang, S. Yuan, A. Nie, K. Zhai, T. Xue, F. Wen, and Z. Liu, “Room temperature two-dimensional ferromagnetic Ni-doped Fe5GeTe2 with tunable Tc for enhanced oxygen evolution reaction”, Applied Physics Letters **123**, 071902 (2023).

[118] B. Zhao, B. Karpiak, D. Khokhriakov, A. Johansson, A. M. Hoque, X. Xu, Y. Jiang, I. Mertig, and S. P. Dash, “Unconventional Charge–Spin Conversion in Weyl-Semimetal WTe2”, en, Advanced Materials **32**, 2000818 (2020).

[119] L. Bainsla, B. Zhao, N. Behera, A. M. Hoque, L. Sjöström, A. Martinelli, M. Abdel-Hafiez, J. Åkerman, and S. P. Dash, “Large out-of-plane spin–orbit torque in topological Weyl semimetal TaIrTe4”, en, Nature Communications **15**, 4649 (2024).

[120] M. Vila, C.-H. Hsu, J. H. Garcia, L. A. Benítez, X. Waintal, S. O. Valenzuela, V. M. Pereira, and S. Roche, “Low-symmetry topological materials for large charge-to-spin interconversion: The case of transition metal dichalcogenide monolayers”, en, Physical Review Research **3**, 043230 (2021).

[121] T. M. J. Cham, R. J. Dorrian, X. S. Zhang, A. H. Dismukes, D. G. Chica, A. F. May, X. Roy, D. A. Muller, D. C. Ralph, and Y. K. Luo, “Exchange Bias Between van der Waals Materials: Tilted Magnetic States and Field-Free Spin–Orbit-Torque Switching”, en, Advanced Materials **36**, 2305739 (2024).

[122] F. Martin, K. Lee, M. Schmitt, A. Liedtke, A. Shahee, H. T. Simensen, T. Scholz, T. G. Saunderson, D. Go, M. Gradhand, Y. Mokrousov, T. Denneulin, A. Kovács, B. Lotsch, A. Brataas, and M. Kläui, “Strong bulk spin–orbit torques quantified in the van der Waals ferromagnet Fe3GeTe2”, Materials Research Letters **11**, 84–89 (2023).

[123] Q. Liu, J. Xing, Z. Jiang, Y. Guo, X. Jiang, Y. Qi, and J. Zhao, “Layer-dependent magnetic phase diagram in FenGeTe2 (3 n 7) ultrathin films”, en, Communications Physics **5**, 140 (2022).

[124] A. F. May, C. A. Bridges, and M. A. McGuire, “Physical properties and thermal stability ofFe5-xGeTe2 single crystals”, Physical Review Materials **3**, 104401 (2019).

[125] Z. Li, W. Xia, H. Su, Z. Yu, Y. Fu, L. Chen, X. Wang, N. Yu, Z. Zou, and Y. Guo, “Magnetic critical behavior of the van der Waals Fe5GeTe2 crystal with near room temperature ferromagnetism”, en, Scientific Reports **10**, 15345 (2020).

[126] J. Stahl, E. Shlaen, and D. Johrendt, “The van der Waals Ferromagnets Fe5–GeTe2 and Fe5—xNixGeTe2 – Crystal Structure, Stacking Faults, and Magnetic Properties”, Zeitschrift für anorganische und allgemeine Chemie **644**, 1923–1929 (2018).

[127] X. Lv, K. Pei, C. Yang, G. Qin, M. Liu, J. Zhang, and R. Che, “Controllable Topological Magnetic Transformations in the Thickness-Tunable van der Waals Ferromagnet Fe5GeTe2”, ACS Nano **16**, 19319–19327 (2022).

[128] M. T. Birch, F. S. Yasin, K. Litzius, L. Powalla, S. Wintz, F. Schulz, A. E. Kossak, M. Weigand, T. Scholz, B. V. Lotsch, G. Schütz, X. Z. Yu, and M. Burghard, “Influence of Magnetic Sublattice Ordering on Skyrmion Bubble Stability in 2D Magnet Fe5GeTe2”, ACS Nano **18**, 18246–18256 (2024).

[129] M. Schmitt, T. Denneulin, A. Kovács, T. G. Saunderson, P. Rüßmann, A. Shahee, T. Scholz, A. H. Tavabi, M. Gradhand, P. Mavropoulos, B. V. Lotsch, R. E. Dunin-Borkowski, Y. Mokrousov, S. Blügel, and M. Kläui, “Skyrmionic spin structures in layered Fe5GeTe2 up to room temperature”, en, Communications Physics **5**, 254 (2022).

[130] T. T. Ly, J. Park, K. Kim, H.-B. Ahn, N. J. Lee, K. Kim, T.-E. Park, G. Duvjir, N. H. Lam, K. Jang, C.-Y. You, Y. Jo, S. K. Kim, C. Lee, S. Kim, and J. Kim, “Direct Observation of Fe-Ge Ordering in Fe5xGeTe2 Crystals and Resultant Helimagnetism”, en, Advanced Functional Materials **31**, 2009758 (2021).

[131] H. Zhang, R. Chen, K. Zhai, X. Chen, L. Caretta, X. Huang, R. V. Chopdekar, J. Cao, J. Sun, J. Yao, R. Birgeneau, and R. Ramesh, “Itinerant ferromagnetism in van der Waals Fe5GeTe2 crystals above room temperature”, Physical Review B **102**, 064417 (2020).

[132] C. Tan, W.-Q. Xie, G. Zheng, N. Aloufi, S. Albarakati, M. Algarni, J. Li, J. Partridge, D. Culcer, X. Wang, J. B. Yi, M. Tian, Y. Xiong, Y.-J. Zhao, and L. Wang, “Gate-Controlled Magnetic Phase Transition in a van der Waals Magnet Fe5GeTe2”, Nano Letters **21**, 5599–5605 (2021).

[133] R. Mathieu, P. Jönsson, D. N. H. Nam, and P. Nordblad, “Memory and superposition in a spin glass”, Physical Review B **63**, 092401 (2001).

[134] T. Ohta, K. Sakai, H. Taniguchi, B. Driesen, Y. Okada, K. Kobayashi, and Y. Niimi, “Enhancement of coercive field in atomically-thin quenched Fe5GeTe2”, en, Applied Physics Express **13**, 043005 (2020).

[135] M. Ribeiro, G. Gentile, A. Marty, D. Dosenovic, H. Okuno, C. Vergnaud, J.-F. Jacquot, D. Jalabert, D. Longo, P. Ohresser, A. Hallal, M. Chshiev, O. Boulle, F. Bonell, and M. Jamet, “Large-scale epitaxy of two-dimensional van der Waals room-temperature ferromagnet Fe5GeTe2”, en, npj 2D Materials and Applications **6**, 10 (2022).

[136] C. Tian, F. Pan, S. Xu, K. Ai, T. Xia, and P. Cheng, “Tunable magnetic properties in van der Waals crystals (Fe1xCox)5GeTe2”, Applied Physics Letters **116**, 202402 (2020).

[137] J. Zhang, Z. Wang, Y. Xing, X. Luo, Z. Wang, G. Wang, A. Shen, H. Ye, S. Dong, and L. Li, “Enhanced magnetic and electrical properties of Co-doped Fe5GeTe2”, Applied Physics Letters **124**, 103103 (2024).

[138] S. Ershadrad, S. Ghosh, D. Wang, Y. Kvashnin, and B. Sanyal, “Unusual Magnetic Features in Two-Dimensional Fe5GeTe2 Induced by Structural Reconstructions”, The Journal of Physical Chemistry Letters **13**, 4877–4883 (2022).

[139] S. Ghosh, S. Ershadrad, and B. Sanyal, “Structural distortion and dynamical electron correlation driven enhanced ferromagnetism in Ni-doped two-dimensional Fe5GeTe2 beyond room temperature”, en, 2D Materials **11**, 035002 (2024).

[140] X. Chen, W. Tian, Y. He, H. Zhang, T. L. Werner, S. Lapidus, J. P. C. Ruff, R. Ramesh, and R. J. Birgeneau, "Thermal cycling induced alteration of the stacking order and spin-flip in the room temperature van der Waals magnet Fe5GeTe2", Physical Review Materials **7**, 044411 (2023).

[141] G. Woltersdorf, "SPIN-PUMPING AND TWO-MAGNON SCATTERING IN MAGNETIC MULTILAYERS", en, PhD thesis (Simon Fraser Univeristy, Aug. 2004).

[142] C. Kittel, "On the Theory of Ferromagnetic Resonance Absorption", Physical Review **73**, 155–161 (1948).

[143] M. Farle, "Ferromagnetic resonance of ultrathin metallic layers", en, Reports on Progress in Physics **61**, 755 (1998).

[144] K. Kim, J. Seo, E. Lee, K.-T. Ko, B. S. Kim, B. G. Jang, J. M. Ok, J. Lee, Y. J. Jo, W. Kang, J. H. Shim, C. Kim, H. W. Yeom, B. Il Min, B.-J. Yang, and J. S. Kim, "Large anomalous Hall current induced by topological nodal lines in a ferromagnetic van der Waals semimetal", en, Nature Materials **17**, 794–799 (2018).

[145] W. Cho, Y.-G. Kang, J. Cha, D. H. D. Lee, D. H. Kiem, J. Oh, Y. Joo, S. Yer, D. Kim, J. Park, C. Kim, Y. Yang, Y. Kim, M. J. Han, and H. Yang, "Singular Hall Response from a Correlated Ferromagnetic Flat Nodal-Line Semimetal", en, Advanced Materials **36**, 2402040 (2024).

[146] C. Kittel, "On the Gyromagnetic Ratio and Spectroscopic Splitting Factor of Ferromagnetic Substances", Physical Review **76**, 743–748 (1949).

[147] L. Bainsla, Y. Sakuraba, A. Kumar, A. K. Chaurasiya, K. Masuda, N. Suwannaharn, A. A. Awad, N. Behera, R. Khymyn, T. Sasaki, S. P. Dash, and J. Åkerman, "Energy-Efficient Single Layer Spin Hall Nano-Oscillators Driven by Berry Curvature", ACS Nano **19**, 18534–18544 (2025).

[148] L. Bainsla, R. Yilgin, M. Tsujikawa, K. Z. Suzuki, M. Shirai, and S. Mizukami, "Low magnetic damping for equiatomic CoFeMnSi Heusler alloy", en, Journal of Physics D: Applied Physics **51**, 495001 (2018).

[149] L. Bainsla, A. Kumar, A. A. Awad, C. Wang, M. Zahedinejad, N. Behera, H. Fulara, R. Khymyn, A. Houshang, J. Weissenrieder, and J. Åkerman, "Ultrathin Ferrimagnetic GdFeCo Films with Low Damping", en, Advanced Functional Materials **32**, 2111693 (2022).

[150] L. Alahmed, B. Nepal, J. Macy, W. Zheng, B. Casas, A. Sapkota, N. Jones, A. R. Mazza, M. Brahlek, W. Jin, M. Mahjouri-Samani, S. S.-L. Zhang, C. Mewes, L. Balicas, T. Mewes, and P. Li, "Magnetism and spin dynamics in room-temperature van der Waals magnet Fe5GeTe2", en, 2D Materials **8**, 045030 (2021).

[151] R. Arias and D. L. Mills, “Extrinsic contributions to the ferromagnetic resonance response of ultrathin films”, Physical Review B **60**, 7395–7409 (1999).

[152] P. Kumar, S. Patnaik, and B. K. Kuanr, “Spin dynamics of room temperature van der Waals (vdW) ferromagnets and their usage in microwave devices”, AIP Advances **14**, 025027 (2024).

[153] J. Zhang, Z. Wang, Z. Li, T. Li, S. Liu, J. Zhang, R.-J. Zhang, Q. Jin, Z. Shi, Y. Liu, Z. Sheng, and Z. Zhang, “Sub-THz High Spin Precession Frequency in van der Waals Ferromagnet Fe3GaTe2”, Nano Letters **24**, 12204–12210 (2024).

[154] L. Ni, Z. Chen, W. Li, X. Lu, Y. Yan, L. Zhang, C. Yan, Y. Chen, Y. Gu, Y. Li, R. Zhang, Y. Zhai, R. Liu, Y. Yang, and Y. Xu, “Magnetic dynamics of two-dimensional itinerant ferromagnet Fe3GeTe2*”, en, Chinese Physics B **30**, 097501 (2021).

[155] X. Shen, H. Chen, Y. Li, H. Xia, F. Zeng, J. Xu, H. Y. Kwon, Y. Ji, C. Won, W. Zhang, and Y. Wu, “Multi-domain ferromagnetic resonance in magnetic van der Waals crystals CrI3 and CrBr3”, Journal of Magnetism and Magnetic Materials **528**, 167772 (2021).

[156] T. Zhang, Y. Chen, Y. Li, Z. Guo, Z. Wang, Z. Han, W. He, and J. Zhang, “Laser-induced magnetization dynamics in a van der Waals ferromagnetic Cr2Ge2Te6 nanoflake”, Applied Physics Letters **116**, 223103 (2020).

[157] Y. Zhao, Q. Song, S.-H. Yang, T. Su, W. Yuan, S. S. P. Parkin, J. Shi, and W. Han, “Experimental Investigation of Temperature-Dependent Gilbert Damping in Permalloy Thin Films”, en, Scientific Reports **6**, 22890 (2016).

[158] S. Roche, J. Åkerman, B. Beschoten, J.-C. Charlier, M. Chshiev, S. Prasad Dash, B. Dlubak, J. Fabian, A. Fert, M. Guimarães, F. Guinea, I. Grigorieva, C. Schönenberger, P. Seneor, C. Stampfer, S. O. Valenzuela, X. Waintal, and B. van Wees, “Graphene spintronics: the European Flagship perspective”, en, 2D Materials **2**, 030202 (2015).

[159] N. Tombros, C. Jozsa, M. Popinciuc, H. T. Jonkman, and B. J. van Wees, “Electronic spin transport and spin precession in single graphene layers at room temperature”, en, Nature **448**, 571–574 (2007).

[160] C. K. Safeer, J. Ingla-Aynés, F. Herling, J. H. Garcia, M. Vila, N. Ontoso, M. R. Calvo, S. Roche, L. E. Hueso, and F. Casanova, “Room-Temperature Spin Hall Effect in Graphene/MoS2 van der Waals Heterostructures”, Nano Letters **19**, 1074–1082 (2019).

[161] L. A. Benítez, W. Savero Torres, J. F. Sierra, M. Timmermans, J. H. Garcia, S. Roche, M. V. Costache, and S. O. Valenzuela, “Tunable room-temperature spin galvanic and spin Hall effects in van der Waals heterostructures”, en, Nature Materials **19**, 170–175 (2020).

[162] M. Arai, R. Moriya, N. Yabuki, S. Masubuchi, K. Ueno, and T. Machida, “Construction of van der Waals magnetic tunnel junction using ferromagnetic layered dichalcogenide”, Applied Physics Letters **107**, 103107 (2015).

[163] J. F. Sierra, J. Fabian, R. K. Kawakami, S. Roche, and S. O. Valenzuela, “Van der Waals heterostructures for spintronics and opto-spintronics”, en, Nature Nanotechnology **16**, 856–868 (2021).

[164] M. Beth Stearns, “Simple explanation of tunneling spin-polarization of Fe, Co, Ni and its alloys”, Journal of Magnetism and Magnetic Materials **5**, 167–171 (1977).

[165] A. Dankert, M. V. Kamalakar, J. Bergsten, and S. P. Dash, “Spin transport and precession in graphene measured by nonlocal and three-terminal methods”, Applied Physics Letters **104**, 192403 (2014).

[166] E. I. Rashba, “Theory of electrical spin injection: Tunnel contacts as a solution of the conductivity mismatch problem”, Physical Review B **62**, R16267–R16270 (2000).

[167] W. Han, K. Pi, K. M. McCreary, Y. Li, J. J. I. Wong, A. G. Swartz, and R. K. Kawakami, “Tunneling Spin Injection into Single Layer Graphene”, Physical Review Letters **105**, 167202 (2010).

[168] A. Fert and H. Jaffrès, “Conditions for efficient spin injection from a ferromagnetic metal into a semiconductor”, Physical Review B **64**, 184420 (2001).

[169] S. Takahashi and S. Maekawa, “Spin injection and detection in magnetic nanostructures”, Physical Review B **67**, 052409 (2003).

[170] D. Khokhriakov, A. W. Cummings, K. Song, M. Vila, B. Karpiak, A. Dankert, S. Roche, and S. P. Dash, “Tailoring emergent spin phenomena in Dirac material heterostructures”, Science Advances **4**, eaat9349 (2018).

[171] W. Amamou, G. Stecklein, S. J. Koester, P. A. Crowell, and R. K. Kawakami, “Spin Absorption by In Situ Deposited Nanoscale Magnets on Graphene Spin Valves”, Physical Review Applied **10**, 044050 (2018).

[172] R. Fujita, P. Bassirian, Z. Li, Y. Guo, M. A. Mawass, F. Kronast, G. van der Laan, and T. Hesjedal, “Layer-Dependent Magnetic Domains in Atomically Thin Fe5GeTe2”, ACS Nano **16**, 10545–10553 (2022).

[173] F. Büttner, I. Lemesh, M. Schneider, B. Pfau, C. M. Günther, P. Hessing, J. Geilhufe, L. Caretta, D. Engel, B. Krüger, J. Viefhaus, S. Eisebitt, and G. S. D. Beach, “Field-free deterministic ultrafast creation of magnetic skyrmions by spin–orbit torques”, en, Nature Nanotechnology **12**, 1040–1044 (2017).

[174] B. Zhao, D. Khokhriakov, B. Karpiak, A. M. Hoque, L. Xu, L. Shen, Y. P. Feng, X. Xu, Y. Jiang, and S. P. Dash, “Electrically controlled spin-switch and evolution of Hanle spin precession in graphene”, en, 2D Materials **6**, 035042 (2019).

[175] S. Mühlbauer, B. Binz, F. Jonietz, C. Pfleiderer, A. Rosch, A. Neubauer, R. Georgii, and P. Böni, “Skyrmion Lattice in a Chiral Magnet”, Science **323**, 915–919 (2009).

[176] L. Jiang, Q. Li, J. Li, H. Guo, C. Wu, Z. Luo, R. Xiong, M. Zeng, Z. Luo, J. Zhao, Z. Chen, Z. Zhang, and H. Wu, “Room-Temperature Spin-Logic Operations in van der Waals Ferromagnet Fe3GaTe2”, Nano Letters **25**, 9712–9718 (2025).

[177] D. Zhang, H. Wei, J. Duan, J. Chen, J. Chen, D. Yue, W. Gong, P. Liu, Y. Yang, J. Gou, J. Yan, K. Zhai, P. Wang, S. Hu, Z. Jia, W. Jiang, L. Liu, W. Wang, Y. Li, and Y. Jiang, “Orbital torque switching of room temperature two-dimensional van der Waals ferromagnet Fe3GaTe2”, en, Nature Communications **16**, 7047 (2025).

[178] H. Algaidi, C. Zhang, Y. Ma, C. Liu, A. Chen, D. Zheng, and X. Zhang, “Magnetic critical behavior of van der Waals Fe3GaTe2 with above-room-temperature ferromagnetism”, APL Materials **12**, 011124 (2024).

[179] S. Onoda, N. Sugimoto, and N. Nagaosa, “Intrinsic Versus Extrinsic Anomalous Hall Effect in Ferromagnets”, Physical Review Letters **97**, 126602 (2006).

[180] N. Nagaosa, J. Sinova, S. Onoda, A. H. MacDonald, and N. P. Ong, “Anomalous Hall effect”, en, Reviews of Modern Physics **82**, 1539–1592 (2010).

[181] M. Hayashi, J. Kim, M. Yamanouchi, and H. Ohno, “Quantitative characterization of the spin-orbit torque using harmonic Hall voltage measurements”, Physical Review B **89**, 144425 (2014).

[182] H. Wu, P. Zhang, P. Deng, Q. Lan, Q. Pan, S. A. Razavi, X. Che, L. Huang, B. Dai, K. Wong, X. Han, and K. L. Wang, “Room-Temperature Spin-Orbit Torque from Topological Surface States”, Physical Review Letters **123**, 207205 (2019).

[183] C. O. Avci, K. Garello, M. Gabureac, A. Ghosh, A. Fuhrer, S. F. Alvarado, and P. Gambardella, “Interplay of spin-orbit torque and thermoelectric effects in ferromagnet/normal-metal bilayers”, Physical Review B **90**, 224427 (2014).

[184] Y.-C. Lau and M. Hayashi, “Spin torque efficiency of Ta, W, and Pt in metallic bilayers evaluated by harmonic Hall and spin Hall magnetoresistance measurements”, en, Japanese Journal of Applied Physics **56**, 0802B5 (2017).